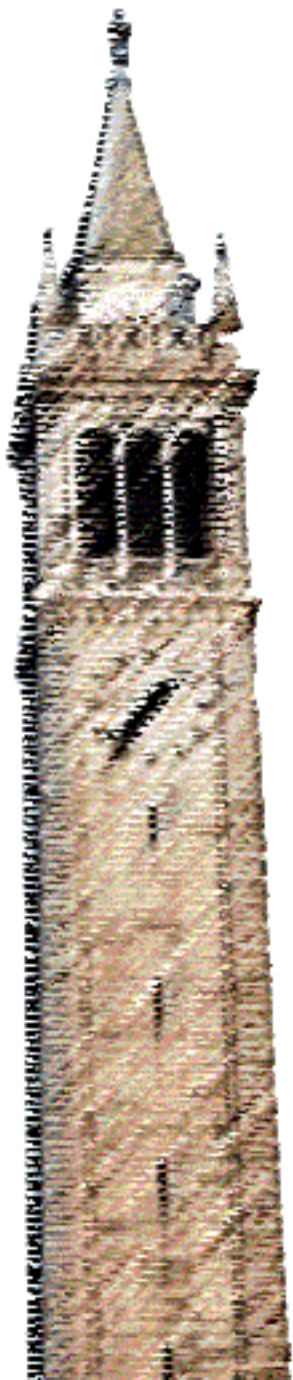


Printed and Flexible Systems for Solar Energy Harvesting

Aminy Ostfeld



Electrical Engineering and Computer Sciences
University of California at Berkeley

Technical Report No. UCB/EECS-2017-19

<http://www2.eecs.berkeley.edu/Pubs/TechRpts/2017/EECS-2017-19.html>

May 1, 2017

Copyright © 2017, by the author(s).
All rights reserved.

Permission to make digital or hard copies of all or part of this work for personal or classroom use is granted without fee provided that copies are not made or distributed for profit or commercial advantage and that copies bear this notice and the full citation on the first page. To copy otherwise, to republish, to post on servers or to redistribute to lists, requires prior specific permission.

Printed and Flexible Systems for Solar Energy Harvesting

by

Aminy Erin Ostfeld

A dissertation submitted in partial satisfaction of the
requirements for the degree of
Doctor of Philosophy

in

Engineering - Electrical Engineering and Computer Sciences

in the

Graduate Division

of the

University of California, Berkeley

Committee in charge:

Professor Ana Claudia Arias, Chair
Professor Kristofer S.J. Pister
Professor Liwei Lin

Summer 2016

Printed and Flexible Systems for Solar Energy Harvesting

Copyright 2016
by
Aminy Erin Ostfeld

Abstract

Printed and Flexible Systems for Solar Energy Harvesting

by

Aminy Erin Ostfeld

Doctor of Philosophy in Engineering - Electrical Engineering and Computer Sciences

University of California, Berkeley

Professor Ana Claudia Arias, Chair

Emerging wireless and flexible electronic systems such as wearable devices and sensor networks call for a power source that is sustainable, reliable, has high power density, and can be integrated into a flexible package at low cost. These demands can be met using photovoltaic systems, consisting of solar modules for energy harvesting, battery storage to overcome variations in solar module output or load, and often power electronics to regulate voltages and power flows. A great deal of research in recent years has focused on the development of high-performing materials and architectures for individual components such as solar cells and batteries. However, there remains a need for co-design and integration of these components in order to achieve complete power systems optimized for specific applications. To fabricate these systems, printing techniques are of great interest as they can be performed at low temperatures and high speeds and facilitate customization of the components.

This thesis discusses the development of printed and flexible photovoltaic power systems, spanning both device-level and system-level design. Photovoltaic cells and multi-cell modules are designed and manufactured using solution-processed organic materials. The use of carbon nanotube films as a flexible, low-cost, solution-processed transparent electrode for photovoltaics is investigated. Then, photovoltaic modules are integrated with batteries into energy harvesting and storage systems with multiple power levels and form factors, optimized to deliver power to loads such as wearable medical sensors. The energy collecting potentials of these systems are evaluated under indoor and outdoor lighting conditions. Designing the solar module maximum power point to match the battery voltage, as well as optimizing load characteristics such as duty cycle, are shown to enable power systems with long-term wireless operation and high efficiency. Finally, screen-printed passive components are developed and demonstrated in a hybrid flexible voltage regulator circuit. In particular, high-quality printed spiral inductors satisfactory for power electronics applications are achieved through optimization of the geometry and fabrication. Overall, the high-performance devices and integrated system designs demonstrated here have the potential for significant impact in the areas of flexible, portable and large-area electronics.

Contents

Contents	i
1 Introduction and Background	1
1.1 Photovoltaic modules	3
1.1.1 Fundamentals of operation	3
1.1.2 Material choices	6
1.2 Integration of energy storage	9
1.2.1 Energy storage devices	9
1.2.2 Electrical considerations	11
1.2.3 Physical integration	11
1.3 Integration of power management electronics	14
1.3.1 Functions of power management electronics	14
1.3.2 Printed and flexible circuits	17
1.4 Outline of the thesis	22
1.5 References	23
2 Organic Photovoltaic Modules	35
2.1 Materials and structures	35
2.2 Current and area scaling	38
2.3 Voltage and series connection	39
2.4 Printed flexible solar modules	41
2.5 Conclusion	45
2.6 References	45
3 Carbon Nanotube Transparent Electrodes for Photovoltaics	50
3.1 Introduction	50
3.2 Transparent conductive film fabrication and performance	51
3.3 Flexible transparent conductive films	55
3.4 Applications in organic photovoltaics	57
3.5 Conclusion	60
3.6 References	62

4	Design of a Wearable Energy Harvesting and Storage Accessory	67
4.1	Introduction	67
4.2	Experimental details	68
4.3	System components	69
4.3.1	Batteries	69
4.3.2	Solar modules	70
4.4	Solar battery charging	74
4.4.1	Energy conversion and storage efficiency	76
4.4.2	Charging under full-day lighting profiles	78
4.5	Conclusion	79
4.6	References	80
5	Flexible Thin-Film Energy Harvesting and Storage Systems	84
5.1	Introduction	84
5.2	Flexible thin-film batteries	86
5.3	System design for pulse oximeter application	87
5.3.1	Experimental details	88
5.3.2	Solar module characteristics and battery charging	89
5.3.3	Battery and solar module powering loads	91
5.4	Energy systems with battery management	94
5.4.1	System with amorphous silicon solar module	95
5.4.2	System with organic solar module	97
5.4.3	Implications for maximum power point tracking	99
5.5	Conclusion	100
5.6	References	101
6	Printed Components for Power Electronics	105
6.1	Introduction	105
6.2	Experimental details	107
6.3	Inductors	108
6.3.1	Geometry and modeling	108
6.3.2	Ink and printing optimization	111
6.3.3	Optimized inductors for power electronics	114
6.4	Capacitors	115
6.5	Resistors	117
6.6	Circuits	118
6.6.1	RLC circuit	118
6.6.2	Voltage regulator	120
6.7	Conclusion	123
6.8	References	125
7	Conclusions and Future Work	129

7.1	Conclusions	129
7.2	Suggestions for future work	130
7.3	References	132

Acknowledgments

First and foremost, my deepest thanks go to my advisor, Professor Ana Claudia Arias, for creating an environment where I could work on what was important to me, her main concerns being that I remained happy, ambitious, and inspired. The resources and connections she provided for me and for the group as a whole made all of this possible.

For funding, I most gratefully acknowledge the National Science Foundation Graduate Research Fellowship and the Berkeley Chancellor's Fellowship.

The carbon nanotube transparent electrode project was made possible by Linde Nanomaterials. Amélie Catheline, Siân Fogden, Kee-Chan Kim, Kathleen Ligsay, Ce Ma, Graham McFarlane, and Kevin McKeigue were all invaluable collaborators. They provided the carbon nanotube materials, characterized the materials, and were involved in many important discussions about the direction of the project.

Additional materials for solar devices were provided by Zhihua Chen and Antonio Facchetti at Polyera. Portions of this work were performed at the Molecular Foundry, under the guidance of Biwu Ma, Teresa Chen, and Paul Ashby. I also thank Professors Vivek Subramanian, Rachel Segalman, and Ali Javey for access to the equipment in their labs. Thanks to Professor Alexandra von Meier for serving on my quals committee, and to Professor Kristofer Pister and Professor Liwei Lin for serving on both my quals committee and dissertation committee.

I have had the good fortune to work with fantastic labmates in the Flexible Electronic Devices and Systems Laboratory. Joe Corea, Adrien Pierre, and Claire Lochner joined the lab the same year as I did, when it had a floor and some walls and not much else. As the first students, we've had the unusual opportunity to shape the group's focus and personality. They have taught me important lessons along the way as well—to mess with heavy machinery confidently, and sometimes even fix it; to search for opportunities to make an impact, then have the dedication to follow through; to go outdoors and be reminded that the world is beautiful.

Designing solar energy harvesting and storage systems of course requires excellent energy storage devices. Abhinav Gaikwad and Alla Zamarayeva have been incredible collaborators in these projects, by sharing their batteries with me, teaching me the battery fundamentals, and discussing design strategies and project directions.

We've also built up quite a formidable solar team over the years. Thanks to Balthazar, Igal, Jerica, Adrien, Maggie, Natasha, Han, Paolo, and Aida for sharing their insights and working toward the common goal of making effective, cheap and versatile solar cells.

Thanks to Joe, Balthazar, Adrien, and Han for their work on the screen printing and blade coating processes that I have relied on, and all their helpful suggestions. Thanks to Igal and Jerica for performing SEM imaging, and thanks to Claire for providing OLEDs for me to use in demonstrations. I also must acknowledge Yasser and Mahsa for the many helpful discussions we've had about printed and flexible electronics.

Outside the lab, I must thank Patrick, Emmeline, Simon, James, and Michael for all the wonderful time spent playing music, eating, and adventuring.

I owe enormous thanks to my parents for being my science role models and for starting the family tradition of doing a PhD at Berkeley. Thanks to my dad for making Tuesdays better with our phone calls, and for sharing the ups and downs of paper and grant writing. Thanks to my mom for supporting me countless times in countless creative ways: from writing and life advice over lattes, to gifts of tweezers and scissors, to providing kittens for me to snuggle when I need a break.

Finally, thanks to Chris, who has been my ally and my inspiration throughout this journey. Here's to many more decades of changing the world!

Chapter 1

Introduction and Background

Development of large-scale, reliable and cost-effective photovoltaic (PV) power systems is critical for achieving a sustainable energy future, as the sun is the largest source of clean energy available to the planet [1]. Photovoltaics are also an ideal power source for remote locations without electric grid access [2], and are of interest for numerous smaller scale applications including consumer electronics and wearable devices, as well as energy harvesting from indoor light sources for low-power applications such as sensor nodes [3]. For indoor and outdoor applications alike, combining the solar module with energy storage and power management electronics can create a complete power system that can reliably meet the current and voltage demands of electronic loads. Energy storage devices such as batteries are necessary to manage the temporal variations in PV module output, for example due to variations in solar irradiance, as well as variations in load. Power management electronics play a number of vital roles in PV systems, including preventing over-charging and over-discharging of the battery, ensuring maximum power is being extracted from the PV module, and converting the PV module's direct current (DC) output power to alternating current (AC) or to a different DC voltage.

Typically, power management circuits consist of discrete components acquired from various manufacturers and soldered to a rigid printed circuit board (PCB). Similarly, most commercial PV modules and batteries are rigid and bulky, and the conventional PV system implementation involves connecting these disparate components with wires as shown in Figure 1.1. Over the past several years, however, flexible electronic materials and printing-based fabrication techniques have emerged as a potentially transformative set of technologies for photovoltaics, energy storage, and other electronics industries. The use of flexible electronic materials can reduce weight, improve portability, and simplify PV system installation [4–6], in addition to enabling entirely new electronics applications such as wearable sensors and smart labels [7–10]. Additive printing and coating techniques, shown in Figure 1.2, allow materials to be deposited over large areas at high speeds and low temperatures, enabling customizable electronic systems on plastic substrates with low cost and low embodied energy [10–12]. The successes of these technologies inspire visions of printed, flexible, integrated electronic systems such as that illustrated in Figure 1.3, in which flexible PV module and

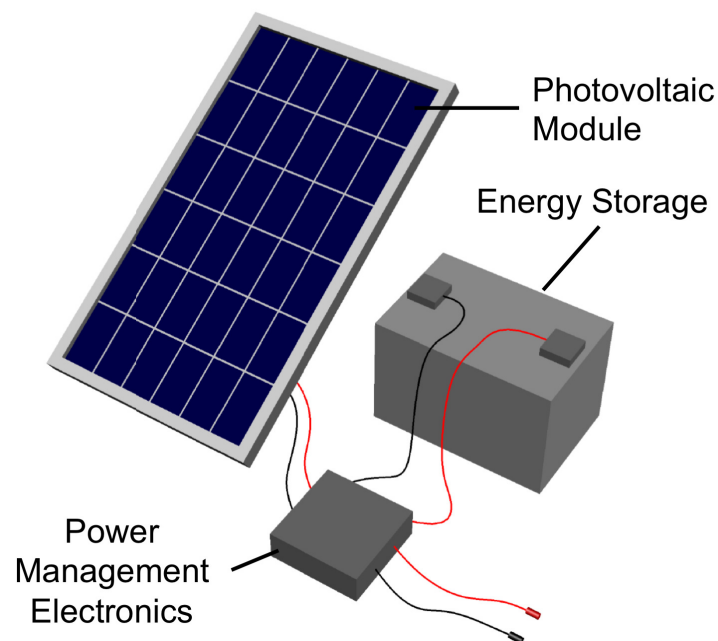


Figure 1.1: Illustration of a typical photovoltaic system including energy storage and power electronics.

battery layers are integrated with printed power management electronics and printed load devices.

To date, the vast majority of research on flexible and solution-processed devices has focused on the development and characterization of new materials, device architectures, and manufacturing processes. This is a critical stage in the development of a new technology, as it establishes performance benchmarks and gives insight into the fundamental physics that must be understood in order to design efficient devices. However, achieving an effective photovoltaic power system for a particular application requires not only high-performing individual components, but also co-design of the components and attention to application-specific constraints. For example, the various applications of photovoltaics impose different requirements in terms of cost, performance, mechanical properties, and degree of integration, and involve various lighting levels and load profiles. These constraints must drive system-level design choices such as system sizing and selection of power management electronics, as well as device-level choices such as the materials and manufacturing processes used for the photovoltaic and energy storage devices.

This thesis spans both levels of design through the development of solar cells and modules, power electronic components, and complete power systems. The thesis also explores the relationships between device characteristics, operating conditions, and system behavior. To provide background for this work, this chapter will introduce the operating principles and material choices for flexible photovoltaic modules; present design considerations, challenges,

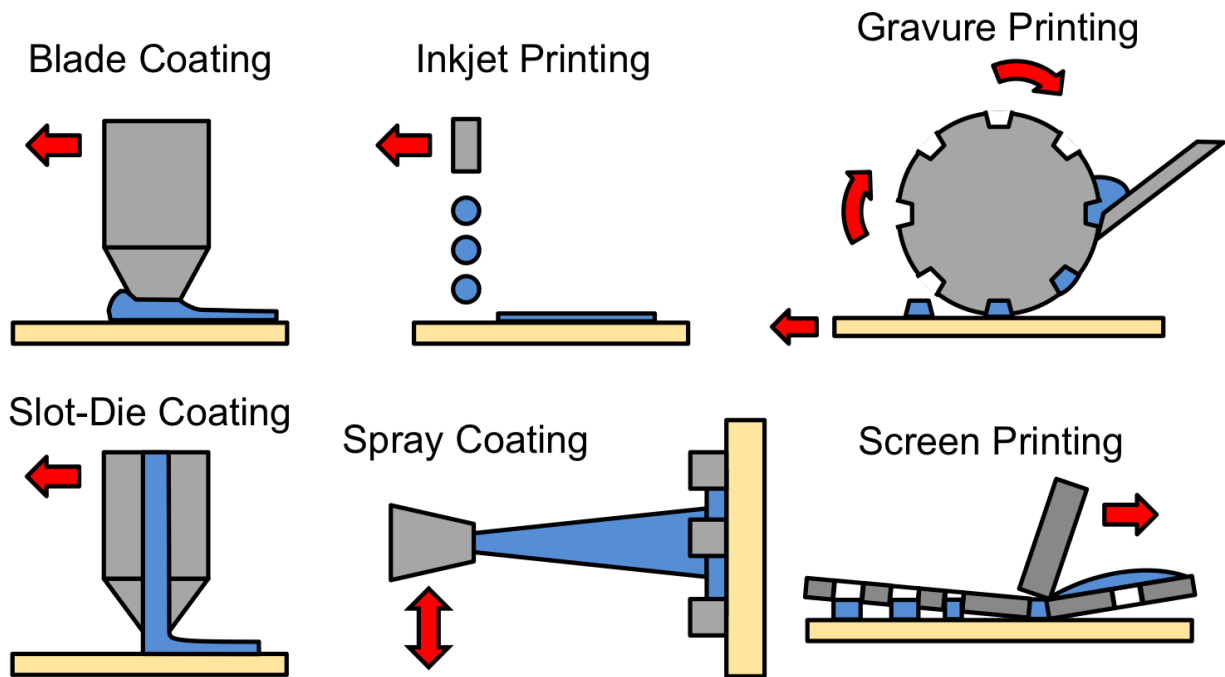


Figure 1.2: Illustrations of printing and coating techniques that are frequently used in the fabrication of electronics and energy devices.

and advances in the integration of energy storage and power electronics; and conclude with an outline of the thesis. Portions of this chapter are submitted as a review paper in [13].

1.1 Photovoltaic modules

1.1.1 Fundamentals of operation

The fundamental components of a photovoltaic cell are an active layer, consisting of one or more semiconducting materials that absorb light and generate a photocurrent, and two contacts that collect the current. A common structure for thin-film PV cells is shown in Figure 1.4 along with the basic principle of operation. Photons absorbed in the active layer generate electron-hole pairs (represented by “e⁻” and “h⁺” in the figure). To collect the electrons and holes as electric current, an electric field must be present across the device. This is accomplished by using multiple doping types in the active layer to create a p-n junction, or multiple materials to create a heterojunction, and/or by employing contacts with two different work functions. This built-in electric field causes photogenerated electrons and holes to flow in opposite directions until they are collected at their respective contacts, resulting in a net current. The back contact is typically a layer of a reflective metal, while

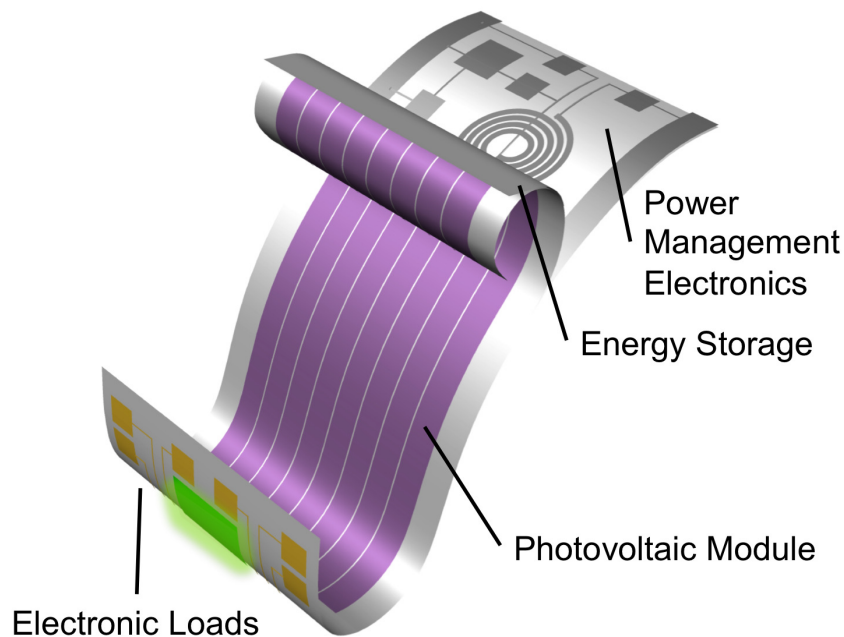


Figure 1.3: Concept illustration of a fully printed and flexible photovoltaic system integrating solar module, energy storage, power management and loads.

the front contact must transmit as much light as possible into the active layer. Typical front contact designs therefore include transparent conductive materials, such as conductive polymers and conductive oxides, or sparse arrays of non-transparent conductive structures, such as metal grids or wires.

In the dark, the solar cell acts as a diode, with a current-voltage characteristic shown schematically in Figure 1.5a. With increasing forward bias voltage, the current increases exponentially. Under illumination, a roughly constant photocurrent flows in the opposite direction as the dark (diode) current, shifting the current-voltage characteristic down on the y-axis as seen in Figure 1.5a. The resulting output power of the solar cell versus voltage is shown in 1.5b. To describe this behavior, the solar cell is typically modeled as a current source in parallel with a diode, as shown in Figure 1.6. To describe the non-idealities of the solar cell, two parasitic resistances are added to the model. The series resistance (R_s) represents losses due to the resistances of the active layer, contacts, and interfaces, and should be made as small as possible. The shunt resistance (R_{sh}) represents leakage pathways, for example due to nonuniform thickness of the active layer, and should be made as large as possible.

Under short circuit conditions (zero applied voltage to the solar cell), a relatively large photocurrent can be extracted, known as the short-circuit current (I_{sc}). This current depends on the number of photons absorbed in the active layer, which in turn depends on the spectrum and irradiance of the light source as well as the bandgap and thickness of the active layer.

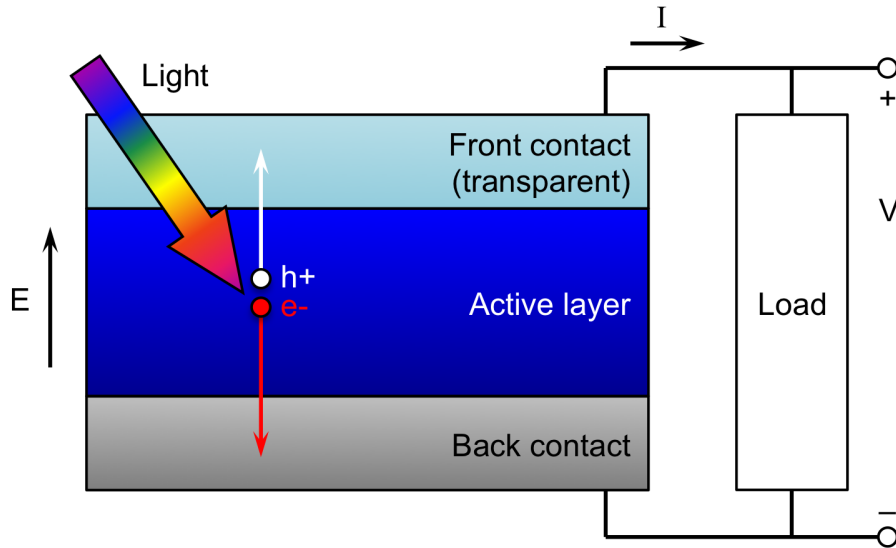


Figure 1.4: Illustration of the operating principle of a photovoltaic cell.

To a first approximation, it can be assumed that incident photons with energy greater than the bandgap are absorbed and those with energy less than the bandgap are not, as long as an appropriate active layer thickness is chosen. For a given spectrum, therefore, the short-circuit current is roughly proportional to the irradiance. Solar cell material sets are often compared in terms of the short-circuit current density J_{sc} , which is the current per unit area. At open circuit, the dark current and photocurrent are equal and opposite, resulting in no net current. The particular voltage at which this occurs is known as the open-circuit voltage, V_{oc} . The open-circuit voltage has a logarithmic dependence on the photocurrent, due to the exponential behavior of the dark current. It is limited by recombination, which increases the dark current, and by the built-in voltage of the cell. When a load is connected to the solar cell, the operating point will occur somewhere along the I-V curve between the open-circuit and short-circuit conditions, with the exact point determined by the load resistance.

Each solar cell also has a maximum power point (MPP), indicated in Figure 1.5, which is the point in its current-voltage curve at which the output power is maximized. The power, current, and voltage at this point are P_{max} , I_{max} , and V_{max} , respectively, and the power conversion efficiency (PCE) of the cell is defined as the ratio of P_{max} to the total power incident on the solar cell in the form of light. The fill factor (FF) is another common figure of merit used to evaluate solar cells, equal to the ratio of P_{max} to the theoretical maximum power, $I_{sc} \times V_{oc}$. Losses due to recombination, series resistance, and shunt resistance lead to a reduced fill factor.

Optimizing the materials, thicknesses, and manufacturing processes for the layers of the solar cell enables a cell with high J_{sc} , V_{oc} , FF, and therefore a high PCE to be achieved. To further increase current under a given illumination condition, for example to meet a certain

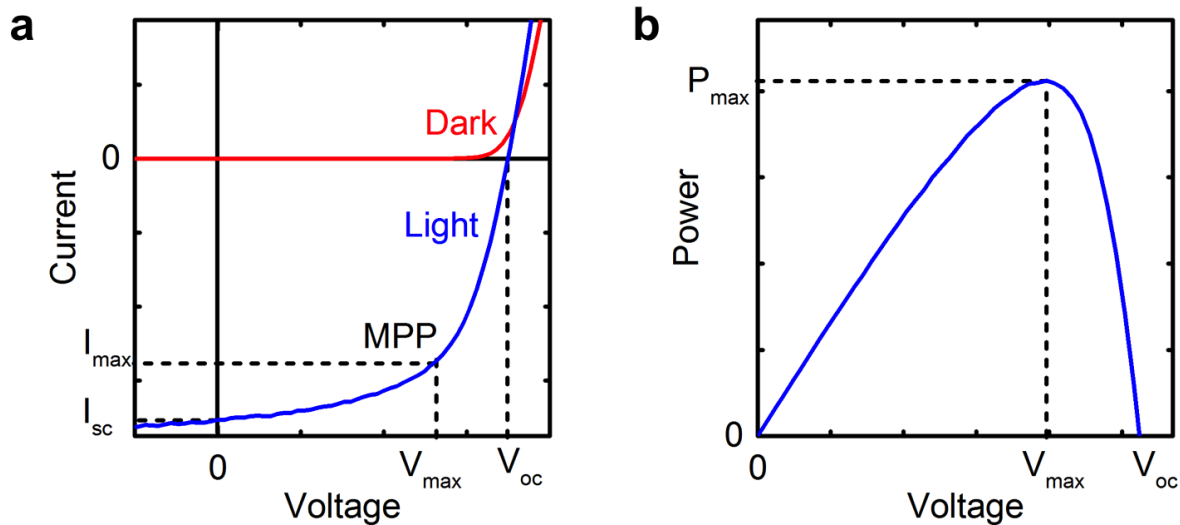


Figure 1.5: (a) Qualitative current-voltage characteristic (I-V curve) of a solar cell in the dark (red curve) and under illumination (blue curve). (b) Power-voltage curve of the same solar cell under the same illumination. Open-circuit voltage, short-circuit current, and maximum power point (MPP) are indicated.

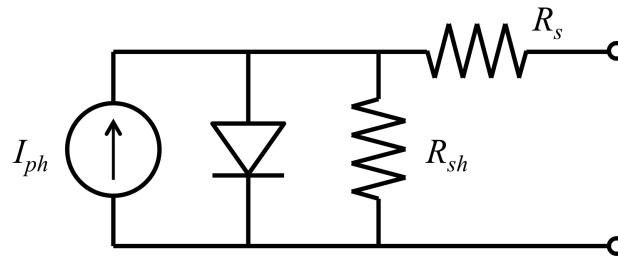


Figure 1.6: Standard equivalent circuit model of a solar cell. The current source represents the photocurrent, I_{ph} . The two parasitic resistances are the series resistance, R_s , and shunt resistance, R_{sh} .

application requirement, cell area can be increased or multiple cells can be connected in parallel. To increase voltage, multiple cells can be connected in series to form a module.

1.1.2 Material choices

Numerous material and manufacturing process options exist for photovoltaic modules. Ideally, a photovoltaic module would be composed of abundant, inexpensive materials that provide good long-term stability and power conversion efficiency under the expected oper-

ation conditions (indoors, outdoors, or both). Manufacturing processes should be scalable to large areas and multi-cell modules at high speed, and should have minimal energy consumption and material waste. A photovoltaic module technology with these characteristics will have low cost per watt, large electricity production potential, and short energy payback time, and will therefore be most appropriate for large-scale production [14, 15]. Although applications such as integration into rigid electronic products do not require the PV module to be mechanically flexible, flexibility is beneficial in many other situations. For example, the use of flexible materials can reduce solar module weight by eliminating the need for bulky protective packaging and allow the modules to be rolled or folded for transportation. As a result, flexible solar cells are ideal for applications such as portable lighting systems in off-grid rural regions [4] and portable power for the military [16]. Flexible solar modules are also advantageous for larger-scale installations and building-integrated photovoltaics because they can be installed very quickly (by simply unrolling) and can be laminated onto surfaces such as roofs and walls [5, 6, 17]. They are also of interest for powering flexible electronics such as health monitoring devices [8, 9] and smart packaging [18] because they can be located near the devices, enabling wireless operation, without compromising the system's flexibility or low profile. However, the solar industry is currently dominated by crystalline silicon, which is brittle and energy intensive to produce, and to a lesser extent the thin-film materials cadmium telluride and copper indium gallium selenide, which rely on rare elements [19]. Amorphous silicon, organics, and perovskites are promising alternatives for flexible and integrated applications based on abundant materials.

Amorphous silicon (a-Si) was the first thin-film PV technology to reach commercial production [20]. a-Si solar cells are typically deposited by plasma-enhanced chemical vapor deposition in a p-i-n structure: light is primarily absorbed in the central intrinsic region, and the built-in electric field aids in charge carrier collection. Although they have higher recombination rates and therefore lower efficiency than crystalline silicon, amorphous silicon solar cells can nevertheless have a shorter energy payback time due to the reduction in energy used to produce the cells [21]. Furthermore, the ability to manufacture a-Si solar cells at relatively low temperatures enables the use of a number of substrates, from common inexpensive plastics such as polyethylene terephthalate (PET) and polyethylene naphthalate (PEN) [22–24], to the cardboard used in food and beverage packaging [18]. Due to their low cost and the variety of form factors available, amorphous silicon solar cells are the most common type of PV device to be integrated into consumer products [3]. Specifically, since small flexible amorphous silicon PV modules have been commercially available for years, they have been the module of choice in a number of integrated flexible energy harvesting systems [25–31].

Organic photovoltaics (OPV) utilize semiconducting polymers and small molecules to form the active layer. Typically, an electron donor (usually a polymer) and an electron acceptor (usually a fullerene) are mixed in solution and cast together to form a bulk heterojunction, an interpenetrating network of donor and acceptor domains. Light absorbed in the donor generates excitons, which must diffuse to an interface with the acceptor where, assisted by the difference in electron affinity of the two materials, they split into free holes in

the donor and free electrons in the acceptor. The bulk heterojunction structure enables the active layer to simultaneously have sufficient thickness for light absorption (~ 100 nm) and domain sizes small enough (~ 10 nm) for efficient exciton collection [32]. Due to the very small thickness required for light absorption, OPVs can be fabricated with total thickness (including the substrate) less than $2 \mu\text{m}$ [33, 34], which is appealing for portable and wearable applications where weight must be minimized. Additionally, the chemical structure of OPV active materials can be customized to achieve a desired color, and the film thickness can be customized to produce semitransparent solar cells, making OPVs ideal for aesthetic and building-integrated applications [35–41]. OPVs have demonstrated similar record efficiencies to amorphous silicon cells in sunlight, in the range of 10–11% [42–44], and can offer higher performance under indoor lighting [45, 46]. Furthermore, due to the low embodied energy of solution-processed carbon-based materials, organic photovoltaics have the potential for energy payback times on the order of a few months, among the best of PV technologies [15]. Since OPVs can be fabricated at low cost and high speed using roll-to-roll coating processes, large-scale installations of OPV modules with areas in the tens of square meters have been demonstrated recently [6].

Perovskite solar cells are a very promising thin-film PV technology due to their high power conversion efficiencies: several recent reports have demonstrated 18% efficiency or higher [42, 47–49]. Perovskite solar cells evolved from dye-sensitized solar cells, which combine a light-absorbing material with mesoporous TiO_2 for electron collection [50]. Unlike conventional dye-sensitized solar cells, perovskite solar cells are solid-state devices, and typically utilize organometal lead trihalide perovskites as the absorbing layer along with an organic hole transporting layer. Although early perovskite solar cells were processed at high temperatures [51, 52], recent advances in low-temperature processing have enabled the use of inexpensive, flexible plastic substrates [53, 54]. Perovskites share many of the advantages of organic solar cells, including compatibility with high-speed solution-based fabrication processes [55], very short energy payback times [56], and the possibility of fabricating semitransparent cells [57].

The promise of organic and perovskite solar cells lies in the ability to fabricate them at large scale, on flexible substrates, using high-speed and low-energy manufacturing processes and low-cost abundant materials. However, most reports on these technologies to date, including those that have yielded the highest efficiencies, use small cell areas, rigid glass substrates, and fabrication processes such as spin coating that are not scalable to large areas or high throughput [11, 43, 48, 49, 54, 58]. To fully realize the potential of organic and perovskite solar cells, excellent performance and reliability must also be achieved using scalable processes and materials. Furthermore, modules must be designed to meet the needs of specific applications, combining cells in series as needed to reach the desired voltage and utilizing an appropriate area to provide the desired current under the expected illumination conditions. Since these challenges are now widely recognized, some efforts are under way (e.g., [55, 59–61]) to manufacture flexible modules in a manner that can be scaled up to high throughput and various module geometries.

1.2 Integration of energy storage

Energy storage is a vital component of a PV system. Solar irradiance is variable and often unpredictable during the day, and entirely unavailable at night. Many loads, on the other hand, require a constant amount of power, or must operate at night, as in the case of lighting. Other loads, such as sensor nodes, often require relatively large pulses of current for sensor operation or data transmission, with periods of much lower power consumption in between. A PV module sized to meet the sensor node's peak demand would be underutilized at non-peak times. Electrochemical energy storage devices such as batteries and supercapacitors address these issues by storing excess energy during periods of high irradiance or light load and releasing that energy as needed at a later time. Both batteries and supercapacitors can be produced in flexible form factors using scalable coating techniques, and are therefore of great interest for flexible power systems [12, 62–67]. To achieve an effective system, the materials and architecture of the energy storage device should be chosen for high performance under the expected operating conditions, and to ensure a good match with the solar module and load in terms of voltage, charge/discharge rate capability, and capacity. Additionally, the system design should take into account physical constraints imposed by the application, such as weight limits, flexibility requirements, and the location(s) where the system will be deployed.

1.2.1 Energy storage devices

An ideal energy storage device for applications in flexible PV systems would have a high specific energy (Wh/L or Wh/kg) so that sufficient energy storage capacity can be achieved in a thin, flexible form factor. The device would retain its capacity over a large number of charge-discharge cycles, so that it can function over the long term to offset daily variation of PV output as well as second- or minute-scale changes in load. It would also have high energy efficiency and low cost. Charge/discharge rate capability, usually defined by the highest charge or discharge rate the device can experience without a substantial drop in capacity or efficiency, is often an important figure of merit as well. Energy storage device architectures with high rate capability allow the peak PV current to be accepted and peak load current to be provided efficiently without necessarily requiring a large capacity.

Lithium-ion batteries are the industry leader for portable electronics due to their high specific energy, high energy efficiency, and long lifetime [68]. They are also beginning to replace lead-acid batteries in off-grid PV energy storage and nickel metal hydride (NiMH) batteries in electric and hybrid vehicles, despite their higher up-front cost, due to these characteristics and the potential for cost reduction as production scales up [69]. Lithium-ion batteries have also received a great deal of attention for integration into flexible electronic systems, and numerous lithium batteries have been demonstrated recently in planar flexible and stretchable forms as well as in the form of flexible wires or fibers for such applications [12, 62–67]. Thin active layers tend to provide higher rate capability and greater mechanical flexibility, but at the cost of a lower capacity per unit area. Efforts are therefore under

way to design batteries with simultaneously high capacity, rate capability and flexibility, for example through the use of nanostructured active materials [70] and current collectors [71]. While many state-of-the-art battery architectures are demonstrated on small (few cm^2) areas, larger-area (25 cm^2) flexible lithium-ion batteries have also been developed and integrated into higher-voltage multi-cell energy storage modules that could be combined with solar cells [72].

Alkaline chemistries such as silver-zinc and zinc-manganese are non-toxic and less reactive than lithium chemistries [73]. As a result, they can be processed in air and require less robust encapsulation, and are preferable for applications such as wearables where they will come into close contact with the human body [74, 75]. Silver-zinc, zinc-manganese, and lithium-ion batteries all tend to have similar practical values of specific energy, in the range of 135-150 Wh/kg [12]. However, the voltage of alkaline batteries (1-2 V) is low compared to the 3.6-4.2 V range of standard lithium-ion battery chemistry, requiring multiple batteries in series [74, 76–78] or power electronics to meet the voltage needs of many electronics. Rechargeable alkaline batteries have also tended to suffer from poor cycle life compared to lithium batteries [74, 79], due to irreversible processes such as migration of silver ions and zinc dendrite formation. However, these issues can be mitigated through the optimization of the electrolyte and separator materials [75, 80].

While state-of-the-art flexible batteries can charge and discharge as quickly as a few minutes [70], further increasing the charge or discharge rate can lead to reduced efficiency or longevity of the battery. Supercapacitors, on the other hand, can operate more rapidly, charging and discharging completely in a few seconds [67]. They also tend to have greater cycling stability than batteries: numerous flexible supercapacitors have been reported with lifetimes of many thousands of cycles [65]. Thus, it may be practical to use a supercapacitor as the sole energy storage component for applications in which a load, such as a sensor node with a bluetooth wireless communication module, requires large pulses of current relatively frequently [30]. However, capacitors also self-discharge more rapidly than batteries, making them unsuitable for long-term energy storage on the scale of days [81]. Combined energy storage schemes using both batteries and capacitors have therefore been proposed for many systems, so that both peak current and long-term energy storage demands can be met [2, 81–83].

Unlike batteries, the voltage of a supercapacitor is zero when the capacitor is fully discharged. As a result, if a supercapacitor connected to a PV module is allowed to discharge completely, the operating point of the PV module will be far away from the maximum power point, and the efficiency of charging will be low until the voltage has increased again. The efficiency can be improved by not allowing the capacitor to discharge completely, thus maintaining the PV module closer to its maximum power point; however, this reduces the usable energy storage capacity of the supercapacitor. This is the case when a battery and supercapacitor are connected in parallel: the supercapacitor is maintained at the same voltage as the battery. Alternatively, power conversion electronics can be added between the PV module and supercapacitor to maximize the efficiency, as will be discussed in more detail later in this chapter.

1.2.2 Electrical considerations

While power electronics are beneficial in many cases, designing the system to perform well without substantial power electronics is ideal, because additional manufacturing complexity, costs and potential points of failure can be avoided. Therefore, the voltage of the power system should be designed to match the requirements of the load devices whenever possible, so that power electronics are not required to convert to the load voltage. The PV module open-circuit voltage should be higher than the maximum voltage of the battery or supercapacitor, so that a full charge is possible. Since the open-circuit voltage of a PV module is roughly logarithmically dependent on the irradiance, attention should be paid to the range of possible open-circuit voltages when designing a system that will experience a range of illumination conditions. Furthermore, the system should be designed so that the operating voltage of the PV module is as close as possible to the maximum power point, as often as possible, so that maximum power is collected. For example, if the system uses a lithium-ion battery, which has a voltage between 3.8 and 4.0 V during the majority of the charging period, the maximum power point of the PV module should be in that range. Achieving the desired PV module voltage involves selecting the appropriate number of series-connected cells; finer tuning of the voltage is also possible through selection of the active layer and contact materials.

The power flows and energy storage capacity of the system are also crucial parameters that can be designed independently of the voltage. For reliable long-term operation without additional power sources, the average power generated by the PV module must be at least equal to the average load power consumption. The energy storage capacity should also be sufficient to overcome the variability in power generation and load. For example, in a standalone solar-powered system, the battery must have enough capacity to power the load during the night, and the solar module must be able to produce at least that much excess energy during the day. PV module current and battery capacity depend on the active area as well as the materials and thicknesses used for the active layers. Improvements in efficiency of thin-film PV modules and areal capacity of thin-film batteries allow these requirements to be met with smaller device footprints. In some applications, the duty cycle of the load can be varied to adjust the average power consumption depending on the amount of power available [83].

1.2.3 Physical integration

The initial electrical design and characterization of a solar energy harvesting and storage system can often be carried out without much attention to the physical integration and form factor of the system. However, to create a viable product for a particular market or application, it is necessary to select an appropriate structure and manufacturing process. There are many strategies for physically combining the components of a PV system, from manufacturing the components in individual packages and installing them in separate locations, to assembling individually manufactured flexible solar cells and storage devices into a single

stack, to single multifunctional devices that perform both energy harvesting and storage simultaneously. The ideal degree of integration and flexibility depends on the requirements of the application; common objectives include maximizing power per unit area, maximizing longevity of the system, minimizing weight, or enabling customization or replacement of components.

It is often advantageous to locate the energy storage and circuitry beneath the solar module, to minimize the footprint required to produce a given amount of power. If the energy storage, solar module, and substrate for the circuitry are all flexible, the entire system can be flexible, enabling attachment to flexible or curved surfaces or integration with flexible load devices. Several flexible PV power systems have therefore been produced by fabricating the solar module, energy storage device, and circuitry using separate manufacturing lines, then laminating the layers together [28, 84, 85]. For example, Krebs and coworkers have developed multiple designs for integrated solar-powered lamps based on in-house printed OPV modules and commercial lithium-ion batteries [4, 86, 87]. In the earliest of these designs [4], the circuitry was printed directly onto the back of the solar module, but due to frequent misalignments and malfunctions of the circuitry, yield was low and many functional solar modules were discarded. Later designs improved yield and reduced cost by utilizing a separate substrate for the circuitry [86, 87]. Since the lamps were distributed to the public, they needed to be durable. Therefore, additional layers were added to improve mechanical robustness, such as a top overlay and a spacer with similar thickness to the battery intended to reduce strain on the battery. Figure 1.7 shows the complete structure and photographs of one of these solar lamps [86].

There is also great interest in leveraging printing and coating techniques to fabricate the energy harvesting and storage devices directly on top of each other [67, 88–90]. These systems, often called photo-rechargeable devices, typically consist of a solar cell and energy storage device built on opposite sides of a shared electrode. The non-shared electrodes of the solar cell and energy storage device are shorted together, thus creating a parallel connection. These approaches could potentially improve the flexibility and weight of the completed power system, since the components are not encapsulated separately, as well as the simplicity of manufacturing and ease of use. The shared-electrode configuration has also been shown to reduce the series resistance, compared to externally connected devices [91]. Although these devices are promising in many respects, several challenges remain before they become viable for use on a large scale. First, the use of shared electrodes greatly constrains the design of the system, as the shared layer must perform well as both a solar cell electrode and a battery or supercapacitor electrode. The architecture and material choice for the other layers of the solar cell and energy storage device must also be compatible with the shared layer. For example, most of the integrated photo-rechargeable devices reported to date have utilized a dye-sensitized solar cell and a supercapacitor because both rely on similar nanostructured electrodes. Additionally, nearly all of the photo-rechargeable devices consist of a single solar cell and a single energy storage device, and as a result the system voltage is limited to the open-circuit voltage of the solar cell. A few higher-voltage photo-rechargeable devices have been demonstrated, through the use of tandem solar cells and series-connected solar cells,

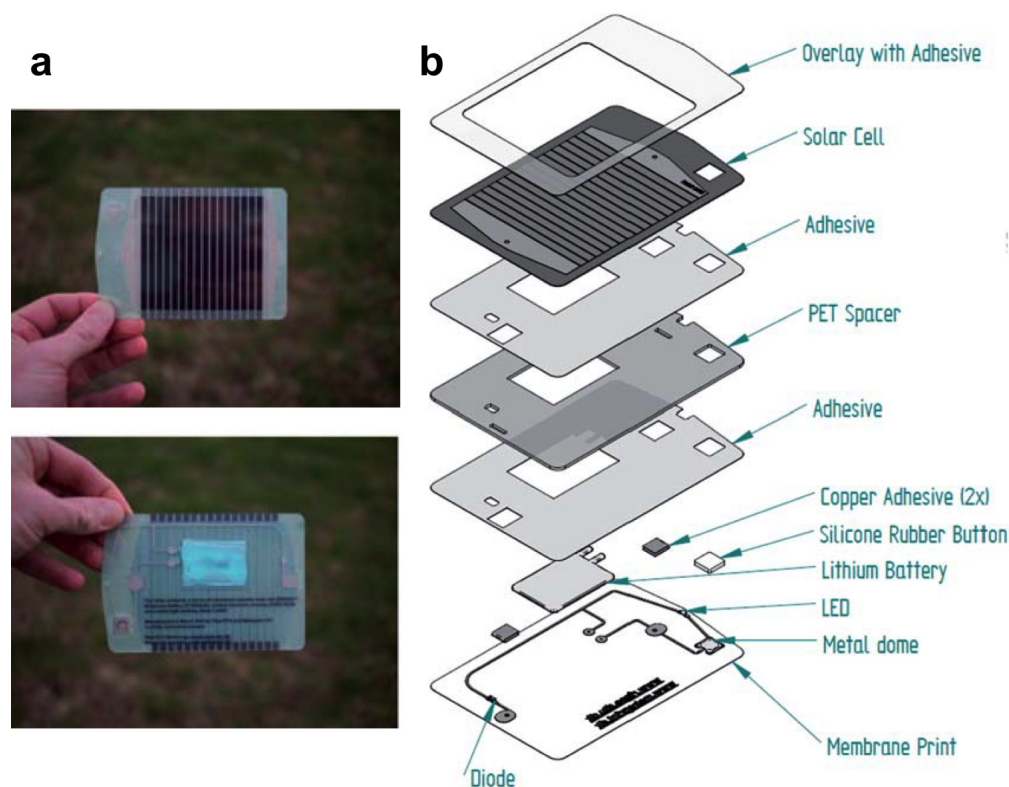


Figure 1.7: (a) Photographs and (b) structure of a solar lamp integrating an OPV module, lithium-ion battery, and light-emitting diode (LED). Reproduced from [86] with permission of the Royal Society of Chemistry.

but the structures and manufacturing processes for such devices remain fairly complex [91, 92]. Fabricating the solar module and battery separately, on the other hand, allows the use of battery chemistries with higher voltages than that of a single solar cell, enabling higher energy density than the fully integrated photo-rechargeable devices. The solar module can then be produced with the ideal number of series-connected cells to charge that battery.

Currently, the benefits of integrating a flexible battery or supercapacitor with the PV module, either by layering the components or as a single photo-rechargeable device, apply primarily to consumer products, portable systems and indoor energy harvesting applications. This is because batteries tend to be sensitive to extreme temperatures and have lifespans shorter than the often-cited 20-year PV module lifespan [3, 19, 68, 69]. Thus, for large-scale outdoor solar installations, which have high cost, are exposed to strong sunlight for long periods of time, and are expected to perform well for many years, it is generally preferable to locate the battery in a separate container where it can be kept away from the sun and can be replaced independently of the solar modules. There has been some investigation of flexible battery performance at elevated temperatures, but more research and optimization is still needed before batteries are ready for reliable long-term integration into outdoor PV

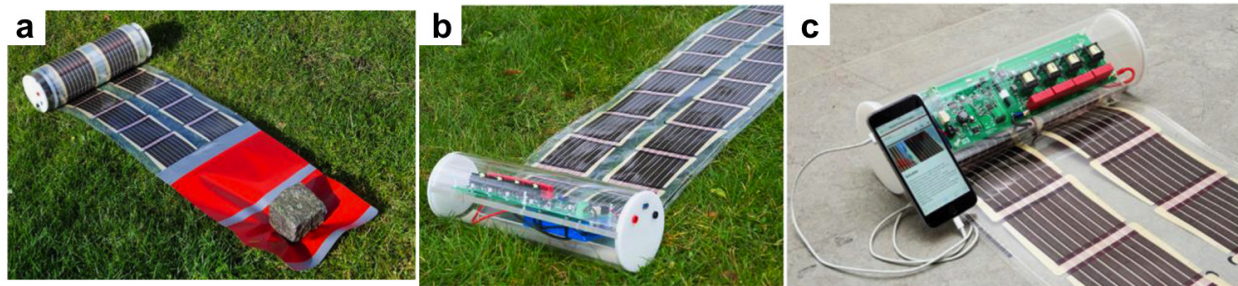


Figure 1.8: Photographs of a rollable solar charger, in which a flexible OPV module can be wrapped around a cylinder containing a rigid battery and power management electronics. Reprinted from [93] with permission from Elsevier.

systems [72]. As an example of a semi-integrated design, Garcia-Valverde et al. developed a portable 15 W PV system for outdoor applications as shown in Figure 1.8 [93]. This system consisted of a flexible OPV module that could be rolled around a plastic cylinder for transport; inside the cylinder was a rigid battery pack and power management electronics on a rigid circuit board. The battery's location underneath the circuit board kept it shaded from direct sunlight, while incorporating all the components into the cylinder form factor made the product user-friendly and free of external wiring.

1.3 Integration of power management electronics

In many lab-scale demonstrations of PV modules used with energy storage devices, the two components are connected directly to each other without any additional electronics, in order to prove the viability of a novel component architecture or the physical integration scheme for the components. However, power management electronics are necessary to transform these proofs of concept into robust systems that operate safely and efficiently under time-varying conditions. The functions of power management electronics include protecting batteries from over-charging or over-discharging, ensuring maximum power is extracted from the PV module even as illumination or load conditions change, and converting from the output power characteristics of the PV system to the requirements of the load. Characteristics such as amount of power, type of energy storage device, and variability of illumination conditions determine which types of power management electronics are needed. Figure 1.9 illustrates the common types of power management electronics in their respective locations in the system.

1.3.1 Functions of power management electronics

A blocking diode, the most basic addition to a PV system, is a diode connected in series between the PV module and the energy storage device. It allows current to flow out of the PV module but prevents discharge of the energy storage device into the PV module in the

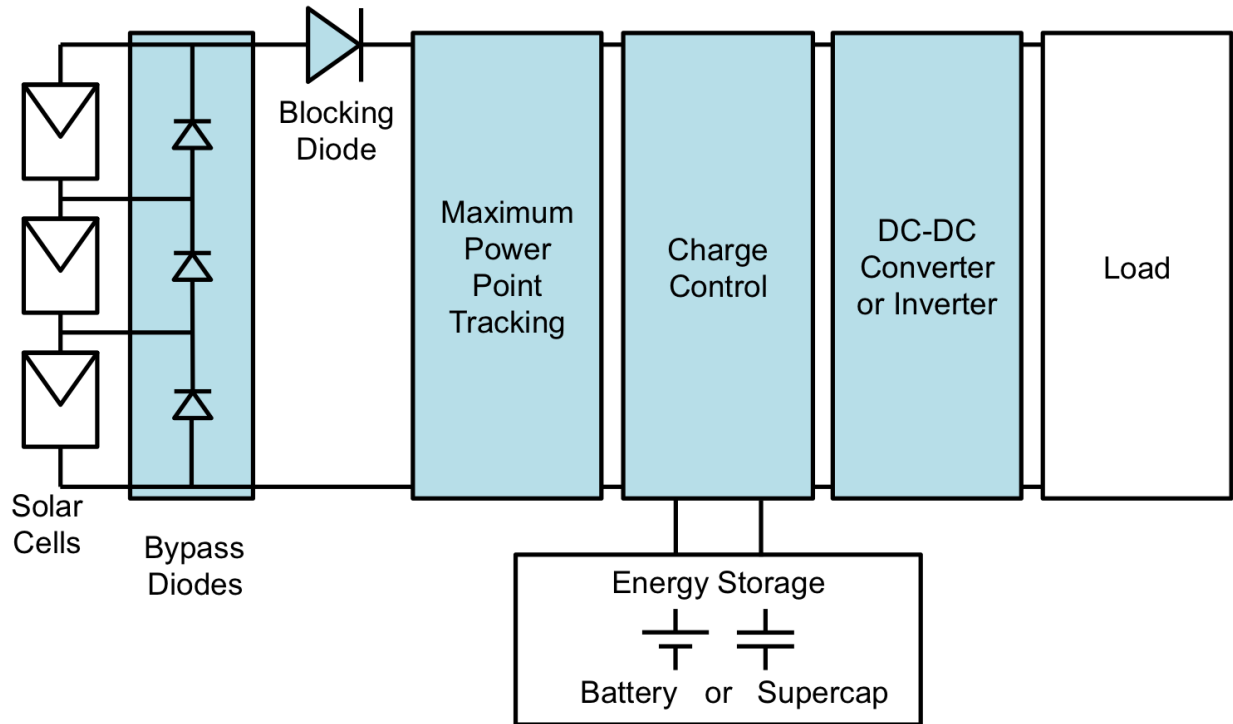


Figure 1.9: Schematic of a PV system, highlighting power management options (in blue) in their respective locations.

absence of light. Blocking diodes are therefore important components of systems that may be in the dark at times. As a result, even systems without any other power management electronics usually include a blocking diode [4, 25, 26, 85, 86, 94, 95]. In these systems, the PV module should be designed with a slightly higher voltage to account for the forward-bias voltage drop of the blocking diode, which is usually on the order of several tenths of a volt. In low-voltage systems, the power loss resulting from this voltage drop can be significant, but in higher-voltage systems it is negligible. Some systems have used an LED as the blocking diode, so the user can visually monitor whether the battery is charging [26, 85].

When multiple PV cells or modules are connected in series, and one or more of the cells is shaded, the current through the entire array is limited by the current of the shaded cell. As a result, diodes can also be connected in parallel with each cell, allowing current to bypass that cell if it becomes shaded. Bypass diodes are most common in large-area systems, where it is likely that the irradiance will vary over the area of the PV array. Alternatively, a switched-capacitor voltage balancing circuit can be used in place of bypass diodes and may offer higher energy collection efficiency [96].

In systems that include batteries, electronics known as battery management or charge controllers are important to maximize battery performance, longevity and safety. Batteries generally have a maximum voltage corresponding to a full charge, and a minimum voltage

corresponding to the fully discharged state; beyond these values irreversible damage can occur. The simplest form of battery management is a zener diode in parallel with the battery to prevent over-charging [87], but battery management integrated circuits (ICs) are also available that perform more complex functions. These functions include disconnecting the load if the battery voltage reaches a set minimum value (indicating that the battery has become fully discharged), and charging the battery using a specified charging profile. In constant current-constant voltage charging, for example, the battery is charged with constant current until it reaches its maximum voltage, then maintained at that voltage until the current decays to zero. Constant current-constant voltage charging allows the battery to be charged completely, at a higher rate than simple constant-current charging, without exceeding the voltage limits [12]. Battery management is particularly important when fast charging is desired, as well as in systems that experience unpredictable illumination or load.

DC-DC converters, circuits that convert from one DC voltage to another, have several potential applications in PV systems. First, the voltage of a system containing batteries or supercapacitors varies depending on the current and state of charge. If a load requires a constant voltage, or one that is not a multiple of the individual battery voltage, a DC-DC converter is needed. For example, organic circuits and light-emitting devices often require a voltage somewhat higher than that of a single lithium battery [97–101]. It can also be advantageous to print solar modules with very high voltages of hundreds to thousands of volts, to simplify assembly and minimize resistive losses, then convert to a lower voltage for use by loads [6, 59, 93]. A DC-DC converter can also be used to ensure that a PV module is operating at its maximum power point regardless of the battery or supercapacitor voltage or load impedance; this type of circuit is called a maximum power point tracker (MPPT). In general, DC-DC converter circuits consist of switches (implemented with transistors or diodes), passive components (inductors and/or capacitors) that perform short-term energy storage, and a control system. Figure 1.10 shows three common DC-DC converter circuits: the boost converter (a), which increases voltage; the buck converter (b), which decreases voltage; and a switched-capacitor voltage doubler, also known as a charge pump (c). In the buck and boost converters, a control system determines the duty cycle of the switches, which sets the conversion ratio, while in switched-capacitor converters the conversion ratio depends on the circuit topology. Depending on the control system, the same basic circuit design can be used to achieve different objectives, such as regulating the output voltage to a constant value, regulating the input voltage to a constant value, or maximizing the output power.

The efficiency of a maximum power point tracking circuit depends on what control algorithm is used, as well as the losses in the circuit components. Indirect MPPT approaches such as constant voltage and fractional open circuit voltage are desirable for small and portable systems, because fewer and smaller components can be used, potentially reducing cost and enabling integration [102]. However, direct MPPT schemes such as the perturb-and-observe and incremental conductance methods tend to have higher efficiency and versatility [103]. Thus, when considering MPPT strategies for a given PV system, it is important to consider the expected efficiencies with MPPT circuits of varying complexity, as well as with no MPPT at all. Since battery voltages tend to vary over a relatively small range (typically 10-15%)

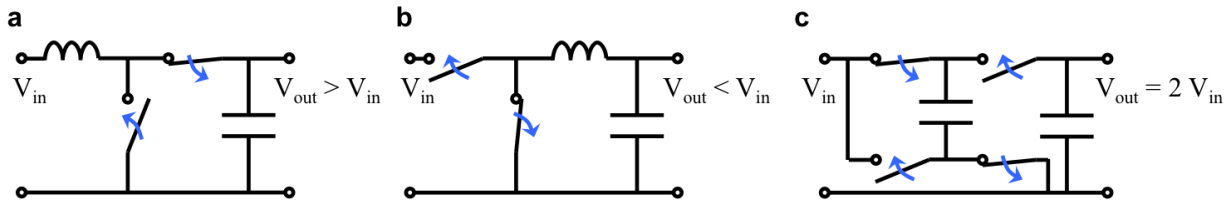


Figure 1.10: Schematics of common DC-DC converters: (a) boost converter, (b) buck converter, (c) charge pump. In each of the circuits, the condition of the switches (open or closed) corresponds to one of the two switching states. Each circuit alternates between this configuration and the opposite switching state, indicated by the blue arrows.

during charging [12, 63, 66, 75], the PV module can be maintained close to its maximum power point simply by choosing a battery with appropriate voltage. For low-cost, low-power systems, the best option may be to connect the PV module and battery directly with no MPPT, allowing cost and complexity to be minimized [104]. For large systems, on the other hand, a MPPT circuit is more desirable because the potential power loss due to the varying battery voltage is larger, the potential losses in the circuit components are smaller by comparison, and the cost of high-performance components is more easily justified. MPPT circuits can be even more advantageous in systems that use supercapacitors, because supercapacitor voltage ranges tend to be greater than those of batteries. When a supercapacitor is discharged, its voltage is zero, meaning a PV cell connected directly will be very far from its maximum power point. For this reason, the energy conversion and storage efficiency of solar supercapacitor charging has typically been about half of the power conversion efficiency of the solar cell [105–107]. Using a MPPT circuit to convert from the solar cell maximum power point voltage to the supercapacitor voltage could greatly increase the efficiency of this process.

Finally, PV systems may also include inverters, which convert from DC to AC power. An inverter is necessary if a system is connected to the grid, or used to power loads that are designed to plug into wall outlets. AC power is also of interest for wireless sensors because it can be transmitted wirelessly through coupled inductors, capacitors, or antennas, avoiding the need for physical connection between energy harvesting and load devices [29]. Like DC-DC converters, inverters often use a combination of transistors and passive components: the transistors are switched to generate an AC waveform, and the passive components filter the waveform to create a sinusoid with minimal distortion.

1.3.2 Printed and flexible circuits

Integration of power management electronics into flexible photovoltaic energy harvesting and storage systems can be accomplished through the use of conventional rigid components on flexible substrates, flexible components, or some combination of the two. Flexible printed circuit boards (flex-PCB) are an established technology in which conventional surface-mount

technology (SMT) components are attached using solder to photolithographically patterned copper-coated flexible plastic substrates. To fabricate a complex circuit such as MPPT, many components are soldered to the flex-PCB; as long as the components are relatively small and sparsely populated, the system remains flexible [28, 30]. The highly conductive copper interconnects and compatibility with SMT components such as silicon ICs allow power electronics with high efficiency at high power levels to be achieved in flex-PCB technology. For example, Acanski et al. demonstrated a MPPT circuit on flex-PCB with 87% efficiency at a power of 100 W, to be integrated into flexible PV panels [108]. Small and low-profile SMT packages (2.2 mm thick or less) were selected for all of the components to minimize bulk and maximize flexibility. The most challenging component to implement in such a low profile SMT package is usually the inductor, a critical part of many DC-DC converters. As a result, several planar spiral inductors for power electronics have been developed, using the PCB copper layers for the windings [108–112]. Several of these designs have incorporated magnetic cores, either by screen printing [109, 111] or laminating [108, 110] layers of magnetic materials onto the spirals.

As an alternative to flex-PCB, conductive materials can be printed directly onto plastic substrates to form the pads and interconnects. A number of techniques exist for attaching SMT components to printed pads at low temperature, including isotropically and anisotropically conductive tapes and metal-filled epoxies [113]. These techniques combined with the low curing temperature of many printable conductors enable the use of less expensive substrates with lower melting points, such as PET and PEN, in place of the polyimide that is typically used in flex-PCBs. Printing can also be employed to fabricate circuits directly on the back of a solar module [4]. Since printing processes are additive, they can potentially reduce process complexity and material waste compared to subtractive processes such as the etching of flex-PCBs [114]. Furthermore, since many types of electronic materials can be printed, including conductors, dielectrics, semiconductors, and magnetic materials, it is of interest to print the power electronic components themselves in addition to the interconnects [102]. Since many devices require the same materials, such as metal contacts, multiple components of a circuit can be printed simultaneously, allowing the entire circuit to be produced with a minimum number of steps by a single manufacturer. Replacing SMT components with printed thin-film components could also reduce weight and volume and improve the mechanical flexibility of the circuit.

Passive components—inductors, capacitors, and resistors—play important roles in DC-DC converters, as seen in Figure 1.10. Inductors and capacitors act as short-term energy storage elements in buck and boost converters and switched-capacitor converters, respectively, enabling the voltage conversion to take place. Capacitors additionally filter out voltage ripples in both types of converters. Resistor networks are used to measure voltages and currents, providing feedback to the control system in order to regulate the conversion ratio. To date, printed and flexible passive components have most often been designed for applications in radio frequency (RF) data transmission or energy harvesting [7, 115–124]. Several other reports have used passive components as a means of demonstrating novel materials, fabrication processes, or integration schemes [125–129]. While these works have not focused

on power electronics specifically, efforts such as minimizing resistance of printed coils [7, 115, 117, 125] may be useful in the design of components for power electronics applications. In one recent work by Van Tassell et al., printed and flexible capacitors were designed specifically for power electronics, using a high- k composite dielectric of barium titanate nanocrystals in an organic matrix [130]. These capacitors outperformed off-the-shelf capacitors in terms of both power density and cost, and were integrated into a 15 W switched-capacitor DC-DC converter with up to 90% efficiency.

Diodes are used in PV systems as blocking diodes, bypass diodes, and components of DC-DC converters. Similarly to the passive components, RF energy harvesting applications have spurred the development of a number of flexible thin-film diodes [118–121, 131, 132]. Since the output voltage of a simple RF rectifying antenna is lower than that required by some applications, voltage multiplying charge pump circuits have been integrated into some of the energy harvesters. In particular, 3x [118, 119] and 4x [120, 132] voltage multipliers have been demonstrated using printed diodes. Some of these diodes have used materials commonly used in OPVs, such as ZnO [119] and poly(3-hexylthiophene) (P3HT) [132], potentially enabling simultaneous fabrication in systems containing OPVs. Although the focus of these works has been on AC-DC converters, the same basic printed diode structures are also of interest for DC-DC charge pumps [120]. Additionally, since solar cells themselves behave as diodes in the dark, Steim et al. explored the use of organic bypass diodes integrated into organic PV modules [133]. These diodes utilized exactly the same materials and structure as the solar cells, but were intentionally shaded. By characterizing the solar module power output with one cell shaded, the authors found the organic bypass diodes to be just as effective as conventional Si or GaAs diodes, but with a greatly simplified manufacturing process.

While these recent reports of printed passive components and diodes show great promise for applications in power electronics, thin-film transistors (TFTs) present a greater challenge for such applications. Fundamental limitations, such as the limited mobility of disordered materials, as well as processing challenges, such as the difficulty of achieving short channel lengths and thin gate dielectrics with high yield by printing, limit the performance of TFTs. As a result, TFTs are generally characterized by high on-resistance and limited operating frequency, and remain the largest hurdle toward high-performing fully printed or thin-film power electronics. Nevertheless, several works have begun to explore the use of TFTs in power electronics, for example in DC-DC converters [31, 134–137], battery management [29], pulsed voltage multipliers [138], and as drive transistors for electrochromic displays [139]. Although achieving efficiencies competitive with those of conventional silicon ICs remains very challenging [134, 137], various techniques are being employed to improve the performance of TFT-based power electronics, including optimizing device dimensions [29, 135] and utilizing higher-mobility semiconductors [136].

A few recent reports have shown integrated TFT-based power electronics for photovoltaic energy harvesting applications. In one example, Fuketa et al. developed a flexible voltage regulating circuit based on complementary organic TFTs [31]. The circuit was a shunt regulator designed to protect the sensitive organic sensing circuitry in a PV-powered wearable healthcare device. By limiting the voltage of the PV module under high illuminance condi-

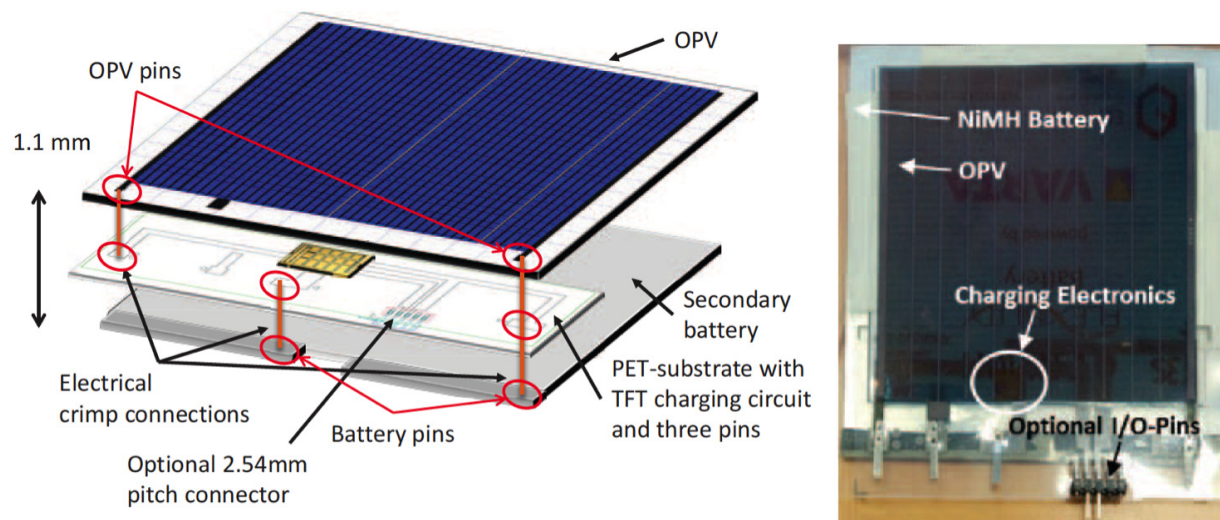


Figure 1.11: Schematic diagram and photograph of solar energy harvesting and storage system based on OPV module, NiMH battery, and IGZO TFT-based power management electronics [137]. ©2015 IEEE.

tions, the addition of the voltage regulator increased the operational illuminance range by a factor of 7.3. Although a battery was not used in this demonstration, a similar organic shunt regulator could also potentially be used to protect a battery from over-charging.

In Meister et al. [137] and Rieutort-Louis et al. [29], PV modules, batteries, and power management electronics were all implemented using thin-film technology to form integrated flexible PV systems. Meister et al. designed a system consisting of a thin-film OPV module, a thin-film NiMH battery, and indium gallium zinc oxide (IGZO) TFT-based power management electronics, in a layered structure as shown in Figure 1.11. Both a 6V/14.4mAh system and a 24V/5.5mAh system were demonstrated; the dimensions of each were selected to allow a full charge in 4 hours under full sun. A diode-connected TFT (gate and drain connected together) was used as a blocking diode. Since the PV open-circuit voltage dropped below the battery maximum voltage under low light conditions, charge pump circuits were designed to boost the voltage and enable low-light charging. The switching signals for the charge pumps were provided by IGZO TFT ring oscillators. The low efficiency of 4% for the charge pump was justified by the argument that even a low-efficiency charge pump expands the range of lighting conditions under which the system can operate: without it the voltage under low light would be too low to charge the battery at all.

The system in Rieutort-Louis et al. was designed specifically for indoor energy harvesting, and used amorphous silicon for both the PV module and the power management electronics, along with a lithium-ion battery pack [29]. The system was designed both to store energy locally for powering integrated “on-sheet” loads and to transfer power wirelessly to “off-sheet” loads, as shown in Figure 1.12. Therefore, the circuitry included battery management as well

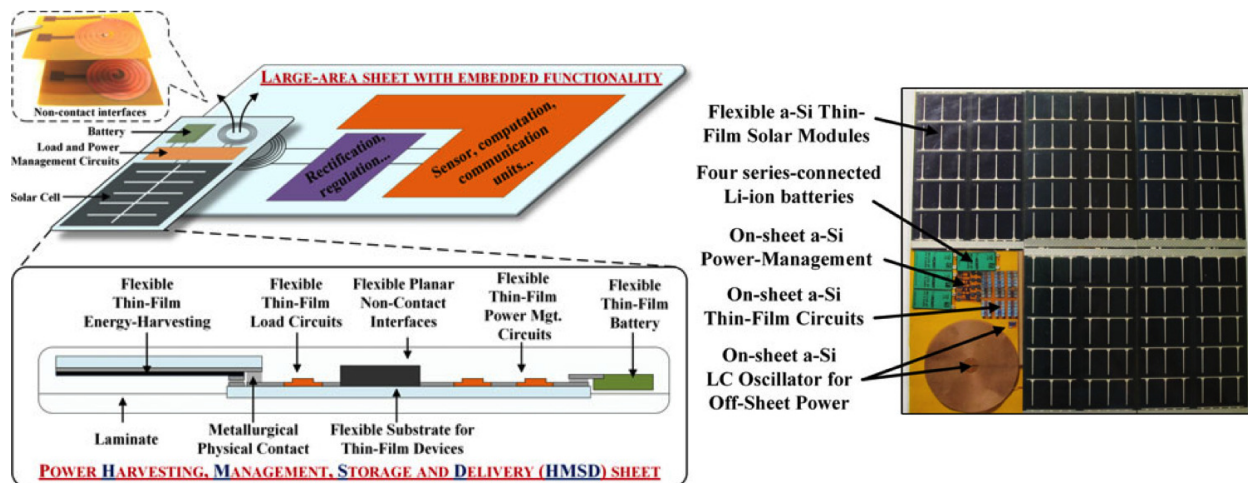


Figure 1.12: Schematic diagram and photograph of system using amorphous silicon solar module and electronics with lithium-ion battery, including inductive link for wireless power transfer [29]. ©2013 IEEE.

as an inverter and inductive interface for wireless power transfer. A power of nearly 5 mW could be delivered to on-sheet loads, at an efficiency of 60%, and up to 8 mW could be transferred wirelessly at an efficiency of 21% for powering off-sheet loads.

In light of the many challenges and opportunities of using thin-film components for power electronics, an important question facing the designer of a flexible PV system is which components to implement in thin-film technology. Fabricating all of the components in the same printing or coating process has the advantages of minimal process complexity and maximum design freedom for every component. Furthermore, avoiding SMT components entirely can potentially minimize bulk and maximize flexibility of the system. However, thin-film components generally have larger footprints and lower performance (particularly in the case of TFTs) relative to their SMT counterparts, leading to serious tradeoffs. For example, if the operating frequency of a DC-DC converter is reduced in order to increase TFT performance, then greater inductance and/or capacitance is needed, requiring larger footprints and potentially increasing losses in the passives.

Hybrid systems, consisting of some SMT and some thin-film components, are considered ideal for many other flexible electronics applications. In medical sensing, for example, thin-film sensors are preferable to interface with the flexible surfaces of the body, but silicon is needed for data processing [9]. Similarly, the hybrid approach may offer a good compromise for PV systems, in which the large-area components (PV module and battery) are printed and flexible, while the choice of technologies for the power management is made to achieve the best balance of performance and form factor. For example, since inductors are often the most bulky components in SMT form and most difficult to integrate into an IC, the ideal hybrid approach for an inductor-based DC-DC converter may consist of SMT components plus a thin-film inductor.

1.4 Outline of the thesis

The preceding sections of this chapter have identified some important areas for improvement for printed and flexible PV systems:

1. Reports of integrated power electronics tend to demonstrate either high performance using all conventional components, or lower performance with all thin-film components. Hybrid approaches, combining optimized thin-film components where possible with conventional components where necessary, could provide an improved balance of performance and form factor.
2. With a few notable exceptions, the bulk of the literature related to printed and flexible energy harvesting and storage focuses on the device level or the materials level. Leveraging these devices for applications also requires system-level design guided by application-specific requirements. Device characteristics, such as material choices and physical structures, should be selected in order to meet the needs of the system.
3. There is a large gap between the application potential of emerging PV technologies such as OPV and the current status of the technology. Meeting application requirements (as discussed in point 2) with OPV requires engineering modules to have certain electrical characteristics, as well as judicious choices of materials and manufacturing processes to balance electrical performance, mechanical properties, cost and scalability.

Investigating these three areas simultaneously could significantly advance the state of flexible photovoltaic power systems. In this thesis, therefore, all three areas are addressed. Chapter 2 discusses the fabrication of organic photovoltaic cells and modules using both spin coating and scalable blade coating techniques. Examples of cell and module design to achieve desired electrical characteristics are presented. Chapter 3 discusses the development of single-walled carbon nanotube networks as a potentially high-performing, flexible, and inexpensive transparent electrode for photovoltaics. The design and evaluation of solar energy harvesting and storage systems with two different power levels and form factors are discussed in Chapters 4 and 5. In Chapter 4, a custom organic photovoltaic module is designed for integration with a silver-zinc wire battery into a wearable energy bracelet. In Chapter 5, a flexible thin-film lithium-ion battery is paired with either a commercial off-the-shelf amorphous silicon solar module or a printed organic photovoltaic module. In both chapters, the energy harvesting capabilities of the systems are assessed under sunlight and indoor lighting conditions. Chapter 5 also discusses load-side optimization and the incorporation of battery management into the system. Finally, Chapter 6 discusses the development of printed and flexible passive components for power electronics, with a focus on inductors, and their integration into a hybrid DC-DC converter circuit. Conclusions and suggestions for future work are presented in Chapter 7.

1.5 References

1. Lewis, N. S. Powering the planet. *MRS Bulletin* **32**, 808–820 (2007).
2. Inganäs, O. & Admassie, S. 25th anniversary article: Organic photovoltaic modules and biopolymer supercapacitors for supply of renewable electricity: A perspective from Africa. *Advanced Materials* **26**, 830–848 (2014).
3. Apostolou, G. & Reinders, A. H. M. E. Overview of design issues in product-integrated photovoltaics. *Energy Technology* **2**, 229–242 (2014).
4. Krebs, F. C., Nielsen, T. D., Fyenbo, J., Wadstrøm, M. & Pedersen, M. S. Manufacture, integration and demonstration of polymer solar cells in a lamp for the "Lighting Africa" initiative. *Energy & Environmental Science* **3**, 512–525 (2010).
5. Darling, S. B. & You, F. The case for organic photovoltaics. *RSC Advances* **3**, 17633–17648 (2013).
6. Krebs, F. C., Espinosa, N., Hösel, M., Søndergaard, R. R. & Jørgensen, M. 25th anniversary article: Rise to power - OPV-based solar parks. *Advanced Materials* **26**, 29–39 (2014).
7. Nilsson, H.-E., Unander, T., Siden, J., Andersson, H., Manuilskiy, A., Hummelgard, M. & Gulliksson, M. System integration of electronic functions in smart packaging applications. *IEEE Transactions on Components, Packaging and Manufacturing Technology* **2**, 1723–1734 (2012).
8. Misra, V., Bozkurt, A., Calhoun, B., Jackson, T., Jur, J., Lach, J., Lee, B., Muth, J., Oralkan, O., Ozturk, M., Trolier-McKinstry, S., Vashaee, D., Wentzloff, D. & Zhu, Y. Flexible technologies for self-powered wearable health and environmental sensing. *Proceedings of the IEEE* **103**, 665–681 (2015).
9. Khan, Y., Ostfeld, A. E., Lochner, C. M., Pierre, A. & Arias, A. C. Monitoring of vital signs with flexible and wearable medical devices. *Advanced Materials* **28**, 4373–4395 (2016).
10. Street, R. A., Ng, T. N., Schwartz, D. E., Whiting, G. L., Lu, J. P., Bringans, R. D. & Veres, J. From printed transistors to printed smart systems. *Proceedings of the IEEE* **103**, 607–618 (2015).
11. Krebs, F. C. Fabrication and processing of polymer solar cells: A review of printing and coating techniques. *Solar Energy Materials and Solar Cells* **93**, 394–412 (2009).
12. Gaikwad, A. M., Arias, A. C. & Steingart, D. A. Recent progress on printed flexible batteries: Mechanical challenges, printing technologies, and future prospects. *Energy Technology* **3**, 305–328 (2015).
13. Ostfeld, A. E. & Arias, A. C. Flexible photovoltaic power systems: Integration opportunities, challenges and advances. *Submitted* (2016).

14. Wadia, C., Alivisatos, A. P. & Kammen, D. M. Materials availability expands the opportunity for large-scale photovoltaics deployment. *Environmental Science & Technology* **43**, 2072–2077 (2009).
15. Lizin, S., Van Passel, S., De Schepper, E., Maes, W., Lutsen, L., Manca, J. & Vanderzande, D. Life cycle analyses of organic photovoltaics: A review. *Energy & Environmental Science* **6**, 3136–3149 (2013).
16. Trautz, K. M., Jenkins, P. P., Walters, R. J., Scheiman, D., Hoheisel, R., Tatavarti, R., Chan, R., Miyamoto, H., Adams, J. G. J., Elarde, V. C. & Grimsley, J. Mobile solar power. *IEEE Journal of Photovoltaics* **3**, 535–541 (2013).
17. Jelle, B. P., Breivik, C. & Røkenes, H. D. Building integrated photovoltaic products: A state-of-the-art review and future research opportunities. *Solar Energy Materials and Solar Cells* **100**, 69–96 (2012).
18. Vicente, A., Águas, H., Mateus, T., Araújo, A., Lyubchyk, A., Siitonen, S., Fortunato, E. & Martins, R. Solar cells for self-sustainable intelligent packaging. *Journal of Materials Chemistry A* **3**, 13226–13236 (2015).
19. Fraunhofer ISE. *Photovoltaics Report* Freiburg, Germany, 2015. <<https://www.ise.fraunhofer.de/en/downloads-englisch/pdf-files-englisch/photovoltaics-report-slides.pdf>>.
20. Shah, A., Torres, P., Tscharnner, R., Wyrsh, N. & Keppner, H. Photovoltaic technology: The case for thin-film solar cells. *Science* **285**, 692–698 (1999).
21. Bhandari, K. P., Collier, J. M., Ellingson, R. J. & Apul, D. S. Energy payback time (EPBT) and energy return on energy invested (EROI) of solar photovoltaic systems: A systematic review and meta-analysis. *Renewable and Sustainable Energy Reviews* **47**, 133–141 (2015).
22. Söderström, T., Haug, F.-J., Terrazzoni-Daudrix, V. & Ballif, C. Optimization of amorphous silicon thin film solar cells for flexible photovoltaics. *Journal of Applied Physics* **103**, 114509 (2008).
23. Fernández, S., Santos, J., Munuera, C., García-Hernández, M. & Naranjo, F. Effect of argon plasma-treated polyethylene terephthalate on ZnO:Al properties for flexible thin film silicon solar cells applications. *Solar Energy Materials and Solar Cells* **133**, 170–179 (2015).
24. Wilken, K., Paetzold, U. W., Meier, M., Prager, N., Fahland, M., Finger, F. & Smirnov, V. Nanoimprint texturing of transparent flexible substrates for improved light management in thin-film solar cells. *Physica Status Solidi (RRL) - Rapid Research Letters* **9**, 215–219 (2015).
25. Kim, H. S., Kang, J. S., Park, J. S., Hahn, H. T., Jung, H. C. & Joung, J. W. Inkjet printed electronics for multifunctional composite structure. *Composites Science and Technology* **69**, 1256–1264 (2009).

26. Kim, J.-S., Ko, D., Yoo, D.-J., Jung, D. S., Yavuz, C. T., Kim, N.-I., Choi, I.-S., Song, J. Y. & Choi, J. W. A half millimeter thick coplanar flexible battery with wireless recharging capability. *Nano Letters* **15**, 2350–2357 (2015).
27. Gambier, P., Anton, S. R., Kong, N., Erturk, A. & Inman, D. J. Piezoelectric, solar and thermal energy harvesting for hybrid low-power generator systems with thin-film batteries. *Measurement Science and Technology* **23**, 015101 (2012).
28. Carmo, J. P., Gomes, J. M., Gonçalves, L. M. & Correia, J. H. A flexible thin-film for powering stand alone electronic devices. *Measurement* **46**, 4145–4151 (2013).
29. Rieutort-Louis, W., Huang, L., Hu, Y., Sanz-Robinson, J., Wagner, S., Sturm, J. C. & Verma, N. A complete fully thin-film PV harvesting and power-management system on plastic with on-sheet battery management and wireless power delivery to off-sheet loads. *IEEE Journal of Photovoltaics* **4**, 432–439 (2014).
30. Toh, W. Y., Tan, Y. K., Koh, W. S. & Siek, L. Autonomous wearable sensor nodes with flexible energy harvesting. *IEEE Sensors Journal* **14**, 2299–2306 (2014).
31. Fuketa, H., Hamamatsu, M., Yokota, T., Yukita, W., Someya, T. T., Sekitani, T., Takamiya, M., Someya, T. T. & Sakurai, T. *Energy-autonomous fever alarm armband integrating fully flexible solar cells, piezoelectric speaker, temperature detector, and 12V organic complementary FET circuits in 2015 IEEE International Solid-State Circuits Conference - (ISSCC) Digest of Technical Papers* (IEEE, San Francisco, CA, 2015), 1–3. doi:10.1109/ISSCC.2015.7063043.
32. Kippelen, B. & Brédas, J.-L. Organic photovoltaics. *Energy & Environmental Science* **2**, 251–261 (2009).
33. Kaltenbrunner, M., White, M. S., Glowacki, E. D., Sekitani, T., Someya, T., Sariciftci, N. S. & Bauer, S. Ultrathin and lightweight organic solar cells with high flexibility. *Nature Communications* **3**, 770 (2012).
34. Jean, J., Wang, A. & Bulović, V. In situ vapor-deposited parylene substrates for ultrathin, lightweight organic solar cells. *Organic Electronics* **31**, 120–126 (2016).
35. Krebs, F. C., Biancardo, M., Winther-Jensen, B., Spanggaard, H. & Alstrup, J. Strategies for incorporation of polymer photovoltaics into garments and textiles. *Solar Energy Materials and Solar Cells* **90**, 1058–1067 (2006).
36. Guo, F., Zhu, X., Forberich, K., Krantz, J., Stubhan, T., Salinas, M., Halik, M., Spallek, S., Butz, B., Spiecker, E., Ameri, T., Li, N., Kubis, P., Guldi, D. M., Matt, G. J. & Brabec, C. J. ITO-free and fully solution-processed semitransparent organic solar cells with high fill factors. *Advanced Energy Materials* **3**, 1062–1067 (2013).
37. Galagan, Y., Shanmugam, S., Teunissen, J., Eggenhuisen, T., Biezemans, A., Van Gijseghem, T., Groen, W. & Andriessen, R. Solution processing of back electrodes for organic solar cells with inverted architecture. *Solar Energy Materials and Solar Cells* **130**, 163–169 (2014).

38. Van der Wiel, B., Egelhaaf, H.-J., Issa, H., Roos, M. & Henze, N. *Market readiness of organic photovoltaics for building integration* in *MRS Proceedings* **1639** (Cambridge University Press, 2014). doi:10.1557/opl.2014.88.
39. Yim, J. H., Joe, S.-Y., Pang, C., Lee, K. M., Jeong, H., Park, J.-Y., Ahn, Y. H., de Mello, J. C. & Lee, S. Fully solution-processed semitransparent organic solar cells with a silver nanowire cathode and a conducting polymer anode. *ACS Nano* **8**, 2857–2863 (2014).
40. Berny, S., Blouin, N., Distler, A., Egelhaaf, H.-J., Krompiec, M., Lohr, A., Lozman, O. R., Morse, G. E., Nanson, L., Pron, A., Sauermann, T., Seidler, N., Tierney, S., Tiwana, P., Wagner, M. & Wilson, H. Solar trees: First large-scale demonstration of fully solution coated, semitransparent, flexible organic photovoltaic modules. *Advanced Science* **3**, 1500342 (2015).
41. Forberich, K., Guo, F., Bronnbauer, C. & Brabec, C. J. Efficiency limits and color of semitransparent organic solar cells for application in building-integrated photovoltaics. *Energy Technology* **3**, 1051–1058 (2015).
42. Green, M. A., Emery, K., Hishikawa, Y., Warta, W. & Dunlop, E. D. Solar cell efficiency tables (version 47). *Progress in Photovoltaics: Research and Applications* **24**, 3–11 (2016).
43. You, J., Dou, L., Yoshimura, K., Kato, T., Ohya, K., Moriarty, T., Emery, K., Chen, C.-C., Gao, J., Li, G. & Yang, Y. A polymer tandem solar cell with 10.6% power conversion efficiency. *Nature Communications* **4**, 1446 (2013).
44. Li, N. & Brabec, C. J. Air-processed polymer tandem solar cells with power conversion efficiency exceeding 10%. *Energy & Environmental Science* **8**, 2902–2909 (2015).
45. Lungenschmied, C., Dennler, G., Neugebauer, H., Sariciftci, S. N., Glatthaar, M., Meyer, T. & Meyer, A. Flexible, long-lived, large-area, organic solar cells. *Solar Energy Materials and Solar Cells* **91**, 379–384 (2007).
46. Minnaert, B. & Veelaert, P. *The appropriateness of organic solar cells for indoor lighting conditions* in *SPIE Photonics Europe* (eds Heremans, P. L., Coehoorn, R. & Adachi, C.) (International Society for Optics and Photonics, Brussels, Belgium, 2010), 77221P–1 – 77221P–11. doi:10.1117/12.854774. <<http://proceedings.spiedigitallibrary.org/proceeding.aspx?articleid=749480>>.
47. Zhou, H., Chen, Q., Li, G., Luo, S., Song, T.-B., Duan, H.-S., Hong, Z., You, J., Liu, Y. & Yang, Y. Interface engineering of highly efficient perovskite solar cells. *Science* **345**, 542–546 (2014).
48. Jeon, N. J., Noh, J. H., Yang, W. S., Kim, Y. C., Ryu, S., Seo, J. & Seok, S. I. Compositional engineering of perovskite materials for high-performance solar cells. *Nature* **517**, 476–480 (2015).

49. Nie, W., Tsai, H., Asadpour, R., Blancon, J.-C., Neukirch, A. J., Gupta, G., Crochet, J. J., Chhowalla, M., Tretiak, S., Alam, M. A., Wang, H.-L. & Mohite, A. D. High-efficiency solution-processed perovskite solar cells with millimeter-scale grains. *Science* **347**, 522–525 (2015).
50. Upadhyaya, H. M., Senthilarasu, S., Hsu, M.-H. & Kumar, D. K. Recent progress and the status of dye-sensitized solar cell (DSSC) technology with state-of-the-art conversion efficiencies. *Solar Energy Materials and Solar Cells* **119**, 291–295 (2013).
51. Lee, M. M., Teuscher, J., Miyasaka, T., Murakami, T. N. & Snaith, H. J. Efficient hybrid solar cells based on meso-superstructured organometal halide perovskites. *Science* **338**, 643–647 (2012).
52. Kim, H.-S., Lee, C.-R., Im, J.-H., Lee, K.-B., Moehl, T., Marchioro, A., Moon, S.-J., Humphry-Baker, R., Yum, J.-H., Moser, J. E., Grätzel, M. & Park, N.-G. Lead iodide perovskite sensitized all-solid-state submicron thin film mesoscopic solar cell with efficiency exceeding 9%. *Scientific Reports* **2**, 583–585 (2012).
53. Green, M. A., Ho-Baillie, A. & Snaith, H. J. The emergence of perovskite solar cells. *Nature Photonics* **8**, 506–514 (2014).
54. Jung, H. S. & Park, N.-G. Perovskite solar cells: From materials to devices. *Small* **11**, 10–25 (2015).
55. Hwang, K., Jung, Y.-S., Heo, Y.-J., Scholes, F. H., Watkins, S. E., Subbiah, J., Jones, D. J., Kim, D.-Y. & Vak, D. Toward large scale roll-to-roll production of fully printed perovskite solar cells. *Advanced Materials* **27**, 1241–1247 (2015).
56. Gong, J., Darling, S. & You, F. Perovskite photovoltaics: Life-cycle assessment of energy and environmental impacts. *Energy & Environmental Science* **8**, 1953–1968 (2015).
57. Eperon, G. E., Burlakov, V. M., Goriely, A. & Snaith, H. J. Neutral color semitransparent microstructured perovskite solar cells. *ACS Nano* **8**, 591–598 (2014).
58. Dou, L., You, J., Hong, Z., Xu, Z., Li, G., Street, R. A. & Yang, Y. 25th anniversary article: A decade of organic/polymeric photovoltaic research. *Advanced Materials* **25**, 6642–6671 (2013).
59. Sommer-Larsen, P., Jørgensen, M., Søndergaard, R. R., Hösel, M. & Krebs, F. C. It is all in the pattern- High-efficiency power extraction from polymer solar cells through high-voltage serial connection. *Energy Technology* **1**, 15–19 (2013).
60. Andersen, T. R., Dam, H. F., Hösel, M., Helgesen, M., Carlé, J. E., Larsen-Olsen, T. T., Gevorgyan, S. A., Andreasen, J. W., Adams, J., Li, N., Machui, F., Spyropoulos, G. D., Ameri, T., Lemaître, N., Legros, M., Scheel, A., Gaiser, D., Kreul, K., Berny, S., Lozman, O. R., Nordman, S., Välimäki, M., Vilkmann, M., Søndergaard, R. R., Jørgensen, M., Brabec, C. J. & Krebs, F. C. Scalable, ambient atmosphere roll-to-roll manufacture of encapsulated large area, flexible organic tandem solar cell modules. *Energy & Environmental Science* **7**, 2925–2933 (2014).

61. Di Giacomo, F., Zardetto, V., D'Epifanio, A., Pescetelli, S., Matteocci, F., Razza, S., Di Carlo, A., Licoccia, S., Kessels, W. M. M., Creatore, M. & Brown, T. M. Flexible perovskite photovoltaic modules and solar cells based on atomic layer deposited compact layers and UV-irradiated TiO₂ scaffolds on plastic substrates. *Advanced Energy Materials* **5**, 1401808 (2015).
62. Gwon, H., Hong, J., Kim, H., Seo, D.-H., Jeon, S. & Kang, K. Recent progress on flexible lithium rechargeable batteries. *Energy & Environmental Science* **7**, 538–551 (2014).
63. Hu, Y. & Sun, X. Flexible rechargeable lithium ion batteries: Advances and challenges in materials and process technologies. *Journal of Materials Chemistry A* **2**, 10712–10738 (2014).
64. Li, L., Wu, Z., Yuan, S. & Zhang, X.-B. Advances and challenges for flexible energy storage and conversion devices and systems. *Energy & Environmental Science* **7**, 2101–2122 (2014).
65. Wang, X., Lu, X., Liu, B., Chen, D., Tong, Y. & Shen, G. Flexible energy-storage devices: Design consideration and recent progress. *Advanced Materials* **26**, 4763–4782 (2014).
66. Zhou, G., Li, F. & Cheng, H.-M. Progress in flexible lithium batteries and future prospects. *Energy & Environmental Science* **7**, 1307–1338 (2014).
67. Vlad, A., Singh, N., Galande, C. & Ajayan, P. M. Design considerations for unconventional electrochemical energy storage architectures. *Advanced Energy Materials* **5**, 1402115 (2015).
68. Scrosati, B. & Garche, J. Lithium batteries: Status, prospects and future. *Journal of Power Sources* **195**, 2419–2430 (2010).
69. Diouf, B. & Podes, R. Potential of lithium-ion batteries in renewable energy. *Renewable Energy* **76**, 375–380 (2015).
70. Wang, X., Liu, B., Hou, X., Wang, Q., Li, W., Chen, D. & Shen, G. Ultralong-life and high-rate web-like Li₄Ti₅O₁₂ anode for high-performance flexible lithium-ion batteries. *Nano Research* **7**, 1073–1082 (2014).
71. Gaikwad, A. M., Khau, B. V., Davies, G., Hertzberg, B., Steingart, D. A. & Arias, A. C. A high areal capacity flexible lithium-ion battery with a strain-compliant design. *Advanced Energy Materials* **5**, 1401389 (2014).
72. Kim, J.-S., Lee, Y.-H., Lee, I., Kim, T.-S., Ryou, M.-H. & Choi, J. W. Large area multi-stacked lithium-ion batteries for flexible and rollable applications. *Journal of Materials Chemistry A* **2**, 10862–10868 (2014).
73. Ingale, N. D., Gallaway, J. W., Nyce, M., Couzis, A. & Banerjee, S. Rechargeability and economic aspects of alkaline zinc-manganese dioxide cells for electrical storage and load leveling. *Journal of Power Sources* **276**, 7–18 (2015).

74. Berchmans, S., Bandodkar, A. J., Jia, W., Ramírez, J., Meng, Y. S. & Wang, J. An epidermal alkaline rechargeable Ag-Zn printable tattoo battery for wearable electronics. *Journal of Materials Chemistry A* **2**, 15788–15795 (2014).
75. Zamarayeva, A. M., Gaikwad, A. M., Deckman, I., Wang, M., Khau, B., Steingart, D. A. & Arias, A. C. Fabrication of a high-performance flexible silver-zinc wire battery. *Advanced Electronic Materials* **2**, 1500296 (2016).
76. Gaikwad, A. M., Zamarayeva, A. M., Rousseau, J., Chu, H., Derin, I. & Steingart, D. A. Highly stretchable alkaline batteries based on an embedded conductive fabric. *Advanced Materials* **24**, 5071–5076 (2012).
77. Gaikwad, A. M., Steingart, D. A., Ng, T. N., Schwartz, D. E. & Whiting, G. L. A flexible high potential printed battery for powering printed electronics. *Applied Physics Letters* **102**, 233302 (2013).
78. Wang, Z. & Mitra, S. Development of flexible secondary alkaline battery with carbon nanotube enhanced electrodes. *Journal of Power Sources* **266**, 296–303 (2014).
79. Kettlgruber, G., Kaltenbrunner, M., Siket, C. M., Moser, R., Graz, I. M., Schwödiauer, R. & Bauer, S. Intrinsically stretchable and rechargeable batteries for self-powered stretchable electronics. *Journal of Materials Chemistry A* **1**, 5505–5508 (2013).
80. Ho, C. C., Evans, J. W. & Wright, P. K. Direct write dispenser printing of a zinc microbattery with an ionic liquid gel electrolyte. *Journal of Micromechanics and Microengineering* **20**, 104009 (2010).
81. MacKenzie, J. D. & Ho, C. Perspectives on energy storage for flexible electronic systems. *Proceedings of the IEEE* **103**, 535–553 (2015).
82. Kan, S. Y., Verwaal, M. & Broekhuizen, H. The use of battery-capacitor combinations in photovoltaic powered products. *Journal of Power Sources* **162**, 971–974 (2006).
83. Dieffenderfer, J. P., Beppler, E., Novak, T., Whitmire, E., Jayakumar, R., Randall, C., Qu, W., Rajagopalan, R. & Bozkurt, A. *Solar powered wrist worn acquisition system for continuous photoplethysmogram monitoring in Engineering in Medicine and Biology Society (EMBC), 2014 36th Annual International Conference of the IEEE (IEEE, Chicago, IL, 2014), 3142–3145. doi:10.1109/EMBC.2014.6944289.*
84. Dennler, G., Bereznev, S., Fichou, D., Holl, K., Ilic, D., Koeppel, R., Krebs, M., Labouret, A., Lungenschmied, C., Marchenko, A., Meissner, D., Mellikov, E., Méot, J., Meyer, A., Meyer, T., Neugebauer, H., Öpik, A., Sariciftci, N., Taillefumier, S. & Wörhle, T. A self-rechargeable and flexible polymer solar battery. *Solar Energy* **81**, 947–957 (2007).
85. Lee, Y.-H., Kim, J.-S., Noh, J., Lee, I., Kim, H. J., Choi, S., Seo, J., Jeon, S., Kim, T.-S., Lee, J.-Y. & Choi, J. W. Wearable textile battery rechargeable by solar energy. *Nano Letters* **13**, 5753–5761 (2013).

86. Krebs, F. C., Fyenbo, J. & Jørgensen, M. Product integration of compact roll-to-roll processed polymer solar cell modules: methods and manufacture using flexographic printing, slot-die coating and rotary screen printing. *Journal of Materials Chemistry* **20**, 8994–9001 (2010).
87. Krebs, F. C., Fyenbo, J., Tanenbaum, D. M., Gevorgyan, S. A., Andriessen, R., van Remoortere, B., Galagan, Y. & Jørgensen, M. The OE-A OPV demonstrator anno domini 2011. *Energy & Environmental Science* **4**, 4116–4123 (2011).
88. Chen, T., Yang, Z. & Peng, H. Integrated devices to realize energy conversion and storage simultaneously. *ChemPhysChem* **14**, 1777–1782 (2013).
89. Song, T. & Sun, B. Towards photo-rechargeable textiles integrating power conversion and energy storage functions: Can we kill two birds with one stone? *ChemSusChem* **6**, 408–410 (2013).
90. Schmidt, D., Hager, M. D. & Schubert, U. S. Photo-rechargeable electric energy storage systems. *Advanced Energy Materials* **6**, 1500369 (2016).
91. Wee, G., Salim, T., Lam, Y. M., Mhaisalkar, S. G. & Srinivasan, M. Printable photo-supercapacitor using single-walled carbon nanotubes. *Energy & Environmental Science* **4**, 413–416 (2011).
92. Guo, W., Xue, X., Wang, S., Lin, C. & Wang, Z. L. An integrated power pack of dye-sensitized solar cell and Li battery based on double-sided TiO₂ nanotube arrays. *Nano Letters* **12**, 2520–2523 (2012).
93. Garcia-Valverde, R., Villarejo, J. A., Hösel, M., Madsen, M. V., Søndergaard, R. R., Jørgensen, M. & Krebs, F. C. Scalable single point power extraction for compact mobile and stand-alone solar harvesting power sources based on fully printed organic photovoltaic modules and efficient high voltage DC/DC conversion. *Solar Energy Materials and Solar Cells* **144**, 48–54 (2016).
94. Jensen, J., Dam, H. F., Reynolds, J. R., Dyer, A. L. & Krebs, F. C. Manufacture and demonstration of organic photovoltaic-powered electrochromic displays using roll coating methods and printable electrolytes. *Journal of Polymer Science Part B: Polymer Physics* **50**, 536–545 (2012).
95. Ye, R. B., Yoshida, K., Ohta, K. & Baba, M. Integrated thin-film rechargeable battery on α -Si thin-film solar cell. *Advanced Materials Research* **788**, 685–688 (2013).
96. Stauth, J. T., Seeman, M. D. & Kesarwani, K. A resonant switched-capacitor IC and embedded system for sub-module photovoltaic power management. *IEEE Journal of Solid-State Circuits* **47**, 3043–3054 (2012).
97. Kopola, P., Tuomikoski, M., Suhonen, R. & Maaninen, A. Gravure printed organic light emitting diodes for lighting applications. *Thin Solid Films* **517**, 5757–5762 (2009).

98. Irimia-Vladu, M., Troshin, P. A., Reisinger, M., Shmygleva, L., Kanbur, Y., Schwabegger, G., Bodea, M., Schwödiauer, R., Mumyatov, A., Fergus, J. W., Razumov, V. F., Sitter, H., Sariciftci, N. S. & Bauer, S. Biocompatible and biodegradable materials for organic field-effect transistors. *Advanced Functional Materials* **20**, 4069–4076 (2010).
99. Smaal, W., Kjellander, C., Jeong, Y., Tripathi, A., Putten, B. V. D., Facchetti, A., Yan, H., Quinn, J., Anthony, J., Myny, K., Dehaene, W. & Gelinck, G. Complementary integrated circuits on plastic foil using inkjet printed n- and p-type organic semiconductors: Fabrication, characterization, and circuit analysis. *Organic Electronics* **13**, 1686–1692 (2012).
100. Lochner, C. M., Khan, Y., Pierre, A. & Arias, A. C. All-organic optoelectronic sensor for pulse oximetry. *Nature Communications* **5**, 5745 (2014).
101. Uno, M., Kanaoka, Y., Cha, B.-S., Isahaya, N., Sakai, M., Matsui, H., Mitsui, C., Okamoto, T., Takeya, J., Kato, T., Katayama, M., Usami, Y. & Yamakami, T. Short-channel solution-processed organic semiconductor transistors and their application in high-speed organic complementary circuits and organic rectifiers. *Advanced Electronic Materials* **1**, 1500178 (2015).
102. Ababei, C., Yuvarajan, S. & Schulz, D. L. Toward integrated PV panels and power electronics using printing technologies. *Solar Energy* **84**, 1111–1123 (2010).
103. Salas, V., Olías, E., Barrado, A. & Lázaro, A. Review of the maximum power point tracking algorithms for stand-alone photovoltaic systems. *Solar Energy Materials and Solar Cells* **90**, 1555–1578 (2006).
104. Nasiri, A., Zabalawi, S. A. & Mandic, G. Indoor power harvesting using photovoltaic cells for low power applications. *IEEE Transaction on Industrial Electronics* **56**, 4502–4509 (2009).
105. Fu, Y., Wu, H., Ye, S., Cai, X., Yu, X., Hou, S., Kafafy, H. & Zou, D. Integrated power fiber for energy conversion and storage. *Energy & Environmental Science* **6**, 805–812 (2013).
106. Skunik-Nuckowska, M., Grzejszczyk, K., Kulesza, P. J., Yang, L., Vlachopoulos, N., Haggman, L., Johansson, E. & Hagfeldt, A. Integration of solid-state dye-sensitized solar cell with metal oxide charge storage material into photoelectrochemical capacitor. *Journal of Power Sources* **234**, 91–99 (2013).
107. Xu, J., Wu, H., Lu, L., Leung, S.-F., Chen, D., Chen, X., Fan, Z., Shen, G. & Li, D. Integrated photo-supercapacitor based on bi-polar TiO₂ nanotube arrays with selective one-side plasma-assisted hydrogenation. *Advanced Functional Materials* **24**, 1840–1846 (2014).
108. Acanski, M., Popovic-Gerber, J. & Ferreira, B. *Design of a flexible very low profile high step-up PV module integrated converter* in *2012 IEEE Energy Conversion Congress and Exposition (ECCE)* (IEEE, Raleigh, NC, 2012), 2942–2948. doi:10.1109/ECCE.2012.6342365.

109. Brandon, E., Wesseling, E., Chang, V. & Kuhn, W. Printed microinductors on flexible substrates for power applications. *IEEE Transactions on Components and Packaging Technologies* **26**, 517–523 (2003).
110. Waffenschmidt, E., Ackermann, B. & Wille, M. *Integrated ultra thin flexible inductors for low power converters* in *IEEE 36th Conference on Power Electronics Specialists, 2005* (IEEE, Recife, Brazil, 2005), 1528–1534. doi:10.1109/PESC.2005.1581833.
111. Bang, D. & Park, J. Ni-Zn ferrite screen printed power inductors for compact DC-DC power converter applications. *IEEE Transactions on Magnetics* **45**, 2762–2765 (2009).
112. Kundrata, J. & Baric, A. *Design of a planar inductor for DC-DC converter on flexible foil applications* in *MIPRO, 2012 Proceedings of the 35th International Convention* (IEEE, Opatija, Croatia, 2012), 54–59. <<http://ieeexplore.ieee.org/xpls/icp.jsp?arnumber=6240613>>.
113. Andersson, H. A., Manuilskiy, A., Haller, S., Hummelgård, M., Sidén, J., Hummelgård, C., Olin, H. & Nilsson, H.-E. Assembling surface mounted components on ink-jet printed double sided paper circuit board. *Nanotechnology* **25**, 094002 (2014).
114. Subramanian, V., Chang, J. B., de la Fuente Vornbrock, A., Huang, D. C., Jagannathan, L., Liao, F., Mattis, B., Molesa, S., Redinger, D. R., Soltman, D., Volkman, S. K. & Zhang, Q. *Printed electronics for low-cost electronic systems: Technology status and application development* in *ESSDERC 2008 - 38th European Solid-State Device Research Conference* (IEEE, Edinburgh, UK, 2008), 17–24. doi:10.1109/ESSDERC.2008.4681691.
115. Redinger, D., Molesa, S., Yin, S., Farschi, R. & Subramanian, V. An ink-jet-deposited passive component process for RFID. *IEEE Transactions on Electron Devices* **51**, 1978–1983 (2004).
116. Leung, S. Y. Y. & Lam, D. C. C. Performance of printed polymer-based RFID antenna on curvilinear surface. *IEEE Transactions on Electronics Packaging Manufacturing* **30**, 200–205 (2007).
117. Lim, N., Kim, J., Lee, S., Kim, N. & Cho, G. Screen printed resonant tags for electronic article surveillance tags. *IEEE Transactions on Advanced Packaging* **32**, 72–76 (2009).
118. Jung, M., Kim, J. J., Noh, J., Lim, N., Lim, C., Lee, G., Kim, J. J., Kang, H., Jung, K., Leonard, A. D., Tour, J. M. & Cho, G. All-printed and roll-to-roll-printable 13.56-MHz-operated 1-bit RF tag on plastic foils. *IEEE Transactions on Electron Devices* **57**, 571–580 (2010).
119. Park, H., Kang, H., Lee, Y., Park, Y., Noh, J. & Cho, G. Fully roll-to-roll gravure printed rectenna on plastic foils for wireless power transmission at 13.56 MHz. *Nanotechnology* **23**, 344006 (2012).
120. Heljo, P., Lilja, K. E., Majumdar, H. S. & Lupo, D. High rectifier output voltages with printed organic charge pump circuit. *Organic Electronics* **15**, 306–310 (2014).

121. Jung, Y., Park, H., Park, J.-A., Noh, J., Choi, Y., Jung, M., Jung, K., Pyo, M., Chen, K., Javey, A. & Cho, G. Fully printed flexible and disposable wireless cyclic voltammetry tag. *Scientific Reports* **5**, 8105 (2015).
122. Hester, J. G., Kim, S., Bitto, J., Le, T., Kimionis, J., Revier, D., Saintsing, C., Su, W., Tehrani, B., Traille, A., Cook, B. S. & Tentzeris, M. M. Additively manufactured nanotechnology and origami-enabled flexible microwave electronics. *Proceedings of the IEEE* **103**, 583–606 (2015).
123. McKerricher, G., Perez, J. G. & Shamim, A. Fully inkjet printed RF inductors and capacitors using polymer dielectric and silver conductive ink with through vias. *IEEE Transactions on Electron Devices* **62**, 1002–1009 (2015).
124. Voutilainen, J.-V., Happonen, T., Hakkinen, J. & Fabritius, T. All silk-screen printed polymer-based remotely readable temperature sensor. *IEEE Sensors Journal* **15**, 723–733 (2015).
125. Bidoki, S. M., Nouri, J. & Heidari, A. A. Inkjet deposited circuit components. *Journal of Micromechanics and Microengineering* **20**, 055023 (2010).
126. Huang, L., Jia, Z., Kymissis, I. & O'Brien, S. High K capacitors and OFET gate dielectrics from self-assembled BaTiO₃ and (Ba,Sr)TiO₃ nanocrystals in the super-paraelectric limit. *Advanced Functional Materials* **20**, 554–560 (2010).
127. Kim, Y., Kim, H. & Yoo, H.-J. Electrical characterization of screen-printed circuits on the fabric. *IEEE Transactions on Advanced Packaging* **33**, 196–205 (2010).
128. Kang, B. J., Lee, C. K. & Oh, J. H. All-inkjet-printed electrical components and circuit fabrication on a plastic substrate. *Microelectronic Engineering* **97**, 251–254 (2012).
129. Chang, J., Zhang, X., Ge, T. & Zhou, J. Fully printed electronics on flexible substrates: High gain amplifiers and DAC. *Organic Electronics* **15**, 701–710 (2014).
130. Van Tassell, B., Yang, S., Le, C., Huang, L., Liu, S., Chando, P., Liu, X., Byro, A., Gerber, D. L., Leland, E. S., Sanders, S. R., Kinget, P. R., Kymissis, I., Steingart, D. & O'Brien, S. Metacapacitors: Printed thin film, flexible capacitors for power conversion applications. *IEEE Transactions on Power Electronics* **31**, 2695–2708 (2016).
131. Myny, K., Steudel, S., Vicca, P., Genoe, J. & Heremans, P. An integrated double half-wave organic Schottky diode rectifier on foil operating at 13.56 MHz. *Applied Physics Letters* **93**, 093305 (2008).
132. Mutlu, S., Haydaroglu, I. & Sevim, A. O. Realization of polymer charge pump circuits using polymer semiconductors. *Organic Electronics* **12**, 312–321 (2011).
133. Steim, R., Schilinsky, P., Choulis, S. A. & Brabec, C. J. Flexible polymer photovoltaic modules with incorporated organic bypass diodes to address module shading effects. *Solar Energy Materials and Solar Cells* **93**, 1963–1967 (2009).
134. Marien, H., Steyaert, M., van Veenendaal, E. & Heremans, P. Organic dual DC-DC upconverter on foil for improved circuit reliability. *Electronics Letters* **47**, 278 (2011).

135. Marien, H., Steyaert, M. S. J., van Veenendaal, E. & Heremans, P. Analog building blocks for organic smart sensor systems in organic thin-film transistor technology on flexible plastic foil. *IEEE Journal of Solid-State Circuits* **47**, 1712–1720 (2012).
136. Hong, S.-H., Yang, I.-S., Kang, J.-S., Hwang, T.-H., Kwon, O.-K., Byun, C.-W., Cheong, W.-S., Hwang, C.-S. & Cho, K.-I. DC-DC converters using indium gallium zinc oxide thin film transistors for mobile display applications. *Japanese Journal of Applied Physics* **49**, 03CB05 (2010).
137. Meister, T., Ishida, K., Shabanpour, R., Boroujeni, B. K., Carta, C., Ellinger, F., Munzenrieder, N., Petti, L., Salvatore, G. A., Troster, G., Wagner, M., Ghesquiere, P., Kiefl, S. & Krebs, M. *Bendable energy-harvesting module with organic photovoltaic, rechargeable battery, and a-IGZO TFT charging electronics in 2015 European Conference on Circuit Theory and Design (ECCTD)* (IEEE, Trondheim, Norway, 2015), 1–4. doi:10.1109/ECCTD.2015.7300095.
138. Ng, T. N., Schwartz, D. E., Mei, P., Kor, S., Veres, J., Bröms, P. & Karlsson, C. Pulsed voltage multiplier based on printed organic devices. *Flexible and Printed Electronics* **1**, 015002 (2016).
139. Pastorelli, F., Schmidt, T. M., Hösel, M., Søndergaard, R. R., Jørgensen, M. & Krebs, F. C. The organic power transistor: Roll-to-roll manufacture, thermal behavior, and power handling when driving printed electronics. *Advanced Engineering Materials* **18**, 51–55 (2015).

Chapter 2

Organic Photovoltaic Modules

Organic photovoltaics (OPV) are of great interest for integrated energy harvesting applications for numerous reasons, including excellent flexibility [1], fabrication via high-speed roll-to-roll printing processes [2], low embodied energy [3], high performance under indoor light [4], and customization of materials and thicknesses to achieve colorful or semitransparent cells [5]. As a result of these many benefits, a vast body of work has been devoted to understanding the physics of organic solar cells and optimizing the materials, manufacturing processes, and device structures [6–9]. In this thesis, organic solar cells are primarily used as components in larger energy harvesting and storage systems. Therefore, this chapter will introduce the relevant characteristics and design considerations of OPVs that allow them to be optimized for system integration. For example, materials and module architectures can be selected to achieve high efficiency as well as to provide certain values of current and voltage in order to meet system requirements. Experimental demonstrations of these design principles are provided using solar cells made with a standard spin coating process. A printed, monolithically integrated OPV module is also developed for flexible electronics applications.

2.1 Materials and structures

The standard lab-scale OPV manufacturing process begins with a glass substrate coated with a transparent conductive film of indium tin oxide (ITO), which will serve as the anode (hole collecting electrode) of the cell. A transparent film of the high-work-function conducting polymer poly(3,4-ethylenedioxythiophene):poly(styrenesulfonate) (PEDOT:PSS) is spin-cast onto the ITO to improve the hole collection efficiency and voltage. The active layer, typically a bulk heterojunction consisting of a polymer electron donor and fullerene electron acceptor, is deposited next, by spin coating a solution containing both materials in the desired ratio. Finally, a low-work-function metal is evaporated to form the cathode.

The process of spin coating on glass substrates cannot be scaled to large areas or done in a roll-to-roll manner, and is therefore of limited use for large-scale manufacturing of solar cells. However, spin coating can be very fast and can give highly reproducible results on a

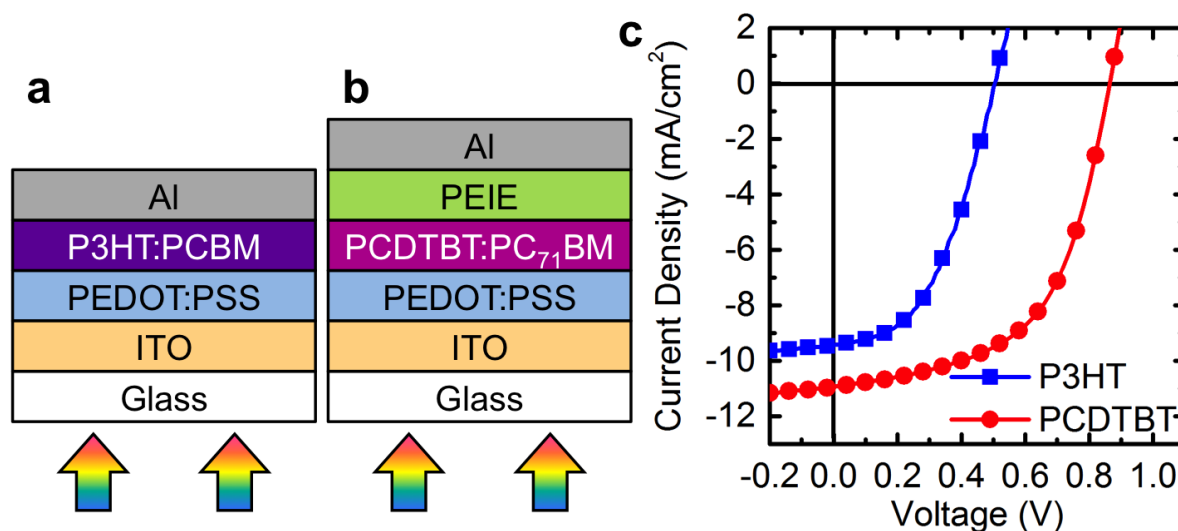


Figure 2.1: Material stacks for (a) P3HT and (b) PCDTBT based solar cells. (c) Typical current density-voltage characteristics obtained with the structures in (a) and (b).

lab scale, making it useful for material screening and prototyping. Spin-coated solar cells and modules can also be employed as the power source in low-power systems, and early-stage electrical design and characterization of such systems can be carried out prior to selecting a scalable OPV manufacturing process.

The most widely used OPV structure, shown in Figure 2.1a, has employed an active layer of poly(3-hexylthiophene) (P3HT) and [6,6]-phenyl-C₆₁-butyric acid methyl ester (PCBM) as the donor and acceptor, respectively, and aluminum as the cathode [10, 11]. Although many OPV material sets have demonstrated higher performance than this structure [12–16], the relationships between processing conditions, morphology and performance of the P3HT:PCBM cell have been exceptionally well characterized [17, 18]. As a result, the P3HT:PCBM active layer remains very useful when evaluating new materials and manufacturing processes for other layers in the solar cell. For example, P3HT:PCBM is used in Chapter 3 of this thesis as the active layer in solar cells employing a novel carbon nanotube transparent electrode [19].

One of the most well-studied higher-efficiency donor polymers is poly[N-9'-heptadecanyl-2,7-carbazole-alt-5,5-(4,7-di-2-thienyl-2',1',3'-benzothiadiazole)] (PCDTBT) [20]. PCDTBT has better energy level alignment with PCBM, reducing the energy lost in electron transfer and improving the open-circuit voltage [21]. Solar cell performance can be improved further by replacing PCBM with [6,6]-phenyl-C₇₁-butyric acid methyl ester (PC₇₁BM), which has stronger absorption in the visible spectrum and thus increases photocurrent [22]. Furthermore, the addition of a very thin dipole layer of polyethyleneimine ethoxylated (PEIE) between the active layer and cathode has been shown to improve photovoltaic performance by reducing the cathode work function [23]. Taking advantage of these materials' bene-

ficial characteristics, solar cells with excellent performance have been demonstrated using PCDTBT:PC₇₁BM active layers and PEIE/Al cathodes, in the structure shown in Figure 2.1b [24]. Solar modules using this cell structure are employed in battery charging systems in Chapters 4 and 5.

For many active layer materials, the thickness must be quite small ($\lesssim 200$ nm) to allow efficient extraction of photogenerated charges before they recombine. Since these thicknesses are on the same order as the wavelengths of the incident light, and the active layers are in contact with reflective metal surfaces (e.g. the aluminum cathode), optical interference effects occur within the active layer. Therefore, certain active layer thicknesses result in local maxima of absorption. For a given active layer material set, then, there are generally one or two optimal thicknesses that provide high absorption and efficient carrier extraction at the same time: 80 or 220 nm for P3HT:PCBM [11, 25] and 70-80 nm for PCDTBT:PC₇₁BM [20], for example. The fabrication process can also play an important role in the performance of OPV cells. For example, both active layers are commonly deposited from solution in 1,2-dichlorobenzene (DCB), which has been shown to produce bulk heterojunctions with small domain size, leading to efficient exciton dissociation [12]. For P3HT:PCBM solar cells, the crystallinity and transport properties can be improved by allowing the film to dry slowly, as well as by thermal annealing [17, 18]. For cells using PCDTBT, which is amorphous, on the other hand, these techniques do not improve the performance [12, 21]. Addition of several percent of a second solvent such as dimethyl sulfoxide (DMSO) can improve the nanoscale morphology and increase efficiency of PCDTBT cells [26].

To maximize the efficiency, thicknesses near the optimal values (about 220 nm for P3HT:PCBM and about 60 nm for PCDTBT:PC₇₁BM) were used in this work. The P3HT:PCBM cells were also allowed to dry slowly under a petri dish after spin coating and thermally annealed at 150°C, and the DMSO additive was employed in the PCDTBT:PC₇₁BM solution. Weight ratios of 1:1 for P3HT:PCBM and 1:3.7 for PCDTBT:PC₇₁BM were used, as these have been shown to yield high efficiencies [17, 24]. The substrates were glass (1.4 × 1.6 cm) coated with a 1-cm-wide stripe of ITO, obtained from Thin Film Devices. To form the hole transport layer, PEDOT:PSS (Clevios P VP AI 4083) was spin-cast to a thickness of 40 nm. The PCDTBT:PC₇₁BM devices used a cathode interlayer of 0.048% PEIE (Sigma-Aldrich) in ethanol spin-cast at 1250 rpm. Aluminum was thermally evaporated to form the cathodes, using a shadow mask to define the active areas of the cells. The active materials were obtained from Polyera (P3HT), SES Research (PCBM), PCAS (PCDTBT) and Solaris (PC₇₁BM).

Even with optimized fabrication, the fundamental differences in the energetic structures of the two material stacks lead to a substantial difference in performance. To illustrate the importance of material selection for OPV performance, Figure 2.1c compares typical current density-voltage characteristics obtained for the two cell types. The typical power conversion efficiency of the PCDTBT based cells (5.3%) is more than double that of the P3HT based cells (2.2%), due primarily to the increase in voltage.

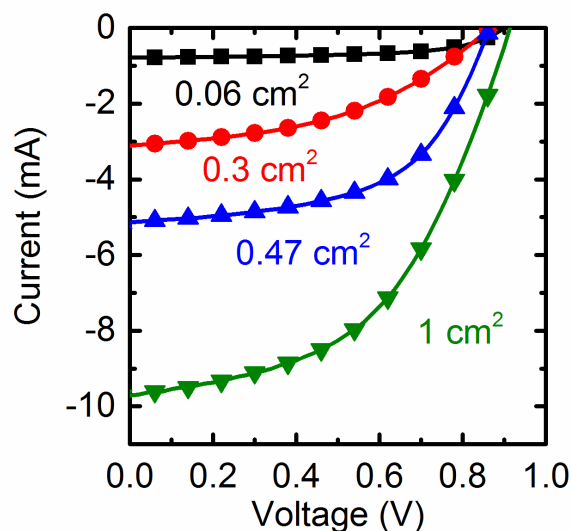


Figure 2.2: Current-voltage characteristics for PCDTBT-based solar cells with four different cell areas, 0.06 cm^2 , 0.3 cm^2 , 0.47 cm^2 , and 1 cm^2 , under solar illumination.

2.2 Current and area scaling

Applications typically require a particular output current from the solar module, for example to charge a battery at a certain rate or meet the current demand of a certain load. Since each OPV layer stack produces a particular photocurrent density (dependent on the material properties and thicknesses), the desired current can be achieved by scaling the active area of the cell.

An example of area scaling is shown in Figure 2.2 for PCDTBT-based solar cells. Four different cell areas are compared, 0.06 cm^2 , 0.3 cm^2 , 0.47 cm^2 , and 1 cm^2 . As expected, the short-circuit current scales approximately linearly with area for a range of areas. I_{sc} values of 3, 5, and 10 mA were measured for the 0.3 , 0.47 , and 1 cm^2 cell areas, corresponding to current densities of 10-11 mA/cm^2 . The smallest cells, 0.06 cm^2 in area, exhibited a slightly higher J_{sc} of $13 \text{ mA}/\text{cm}^2$, a phenomenon that has been reported previously [27]. If active layer material is present outside the active area defined by the contacts, charge carriers will be generated in that area as well. Some of these carriers will diffuse to the active area, where they are collected as additional photocurrent. The smaller the active area, the more significant this edge effect is. Furthermore, increasing cell area lengthens the distance charge carriers must travel within the electrodes, which may introduce more significant series resistance. A modest increase in series resistance will reduce the fill factor, while further increases in series resistance can also reduce the J_{sc} .

Thus, when designing an OPV cell for a particular application, the J_{sc} measured for a cell of an arbitrary area can be used to estimate the area required to achieve the desired current. However, due to the edge and series resistance effects, it is important to verify the

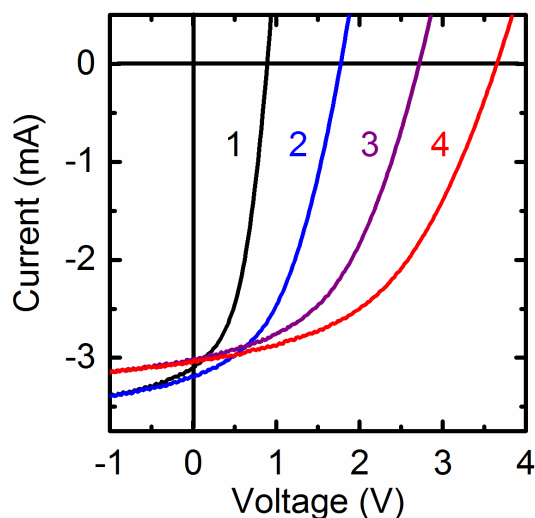


Figure 2.3: Current-voltage characteristics for one to four PCDTBT-based solar cells, 0.3 cm^2 in area, connected in series.

current of the exact cell structure prior to using it in a system.

2.3 Voltage and series connection

Most applications require a higher voltage than that produced by a single solar cell. For example, voltages on the order of 2 V and 4 V are needed to charge alkaline and lithium batteries, respectively [28, 29]. Many common integrated circuits require 3.3 V, while organic electronics and optoelectronics often need closer to 10 V [30–34]. To meet these requirements, multiple solar cells can be connected in series to form a module.

The total voltage of a series-connected module at any given current is equal to the sum of the individual cell voltages. An experimental demonstration of this principle is shown in Figure 2.3, in which up to 4 organic solar cells using the PCDTBT material system are connected in series. The open-circuit voltages measured for 2, 3, and 4 series-connected cells are 1.8, 2.7, and 3.6 V, respectively, or 2, 3, and 4 times the single-cell V_{oc} of 0.89 V.

The current through the series string is limited by the lowest individual cell current. For example, of the 4 cells in the example in Figure 2.3, the photocurrent of the third cell is slightly lower than that of the others. Therefore, when the first and second cells are connected in series (the curve labeled “2” in the figure), the current is similar to that of the first cell alone. When the third cell is added (the curve labeled “3”), however, the current is reduced.

For this reason, it is important to use cells with as similar performance as possible to form the module, so that maximum power is extracted from each cell. In standard silicon PV

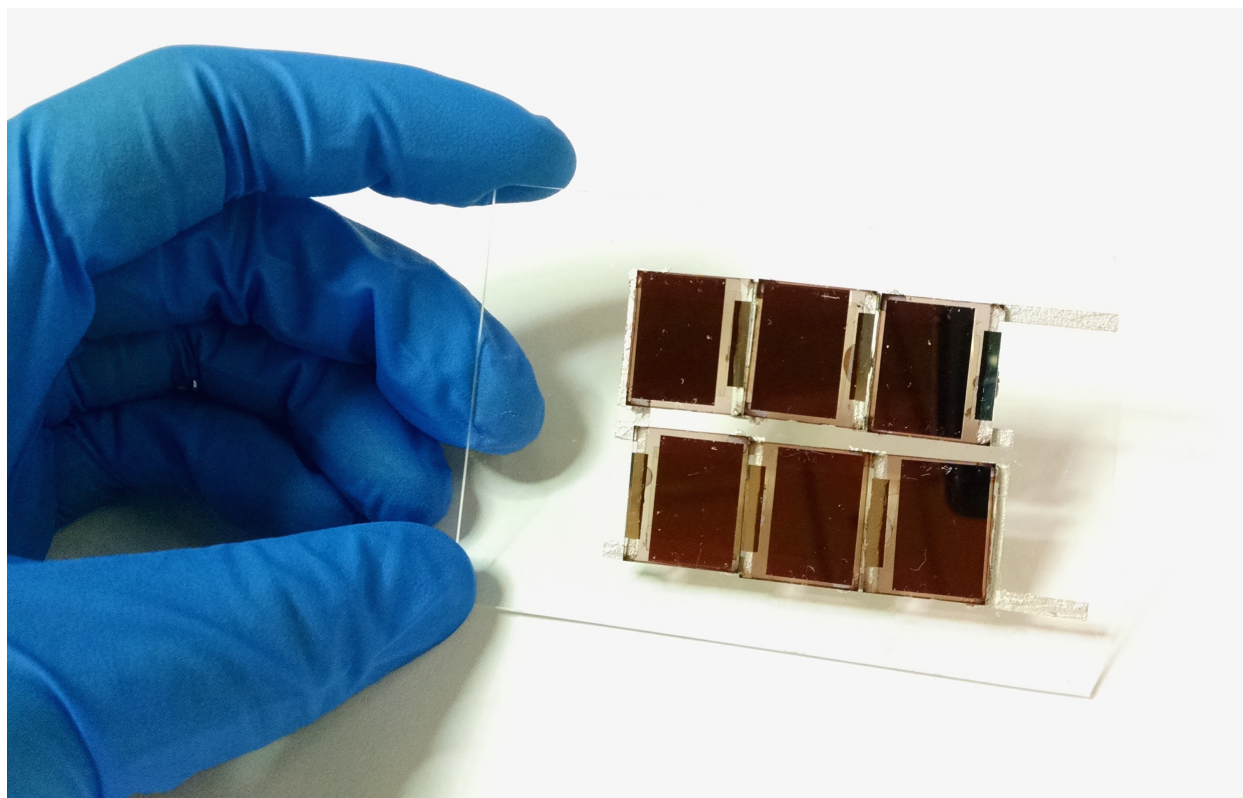


Figure 2.4: Photograph of organic solar module consisting of 6 spin-coated solar cells connected in series.

module fabrication, many cells are fabricated and characterized individually, then grouped based on their performance [35]. Modules are produced by assembling multiple cells from the same group on a common substrate, using conductive interconnects to create series connections between the cells. This approach ensures that similar cells are used in each module, and that any non-functioning or poorly-functioning cells are discarded rather than being incorporated into a module and reducing its efficiency.

A similar technique has been employed here to fabricate a module of organic solar cells. The cells in the module used the PCDTBT material system and had active area of 1×1 cm; typical cell performance is shown by the green line in Figure 2.2. Since each cell had a voltage of about 0.9 V at open circuit and about 0.6 V at the maximum power point, a module with 6 cells would be appropriate for applications in charging lithium batteries. Therefore, 6 cells were connected in series, as seen in the photograph in Figure 2.4. To create the module, silver interconnects were stencil printed onto a large glass slide. The cells were then bonded to the interconnects using silver-filled epoxy (MG Chemicals 8331-14G).

The current-voltage characteristic of the module is shown in Figure 2.5. The module voltage was 5.4 V at open circuit and 3.4 V at the maximum power point, in good agreement with the expected values based on the individual cell voltages. The maximum power output

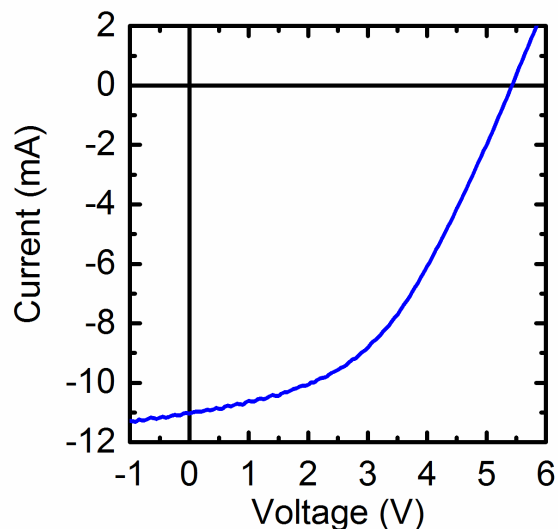


Figure 2.5: Current-voltage characteristic of solar module comprising 6 PCDTBT cells assembled in series.

was 27 mW, representing a power conversion efficiency of 4.5% over the active area. To create a module with similar voltage using the P3HT-based cells in Figure 2.1a, 11 or 12 cells would be needed, and the active area of the module would be doubled as a result.

2.4 Printed flexible solar modules

While spin coating is inherently limited to processing one small substrate at a time, continuous printing and coating processes such as slot-die coating, blade coating, and gravure printing can be used to manufacture OPV devices with much higher throughput [36]. These techniques can be performed in a roll-to-roll fashion and can easily coat material onto flexible substrates, enabling the manufacture of large-area flexible systems. Furthermore, by patterning each layer during or after printing, it is possible to fabricate monolithically integrated modules, in which all of the cells are fabricated simultaneously on a single substrate. This is an appealing alternative to assembling individual spin-coated cells into a module such as that shown in Figure 2.4, for multiple reasons. First, avoiding the steps of assembling the cells and the materials needed to attach them can improve production speed and reduce cost. Additionally, the need for durable substrates for the individual cells and a second substrate on which to assemble them can limit the flexibility of the resulting module. For monolithically integrated modules, on the other hand, only a single substrate is used, potentially improving flexibility.

Here, a process was developed to manufacture monolithically integrated printed OPV modules using blade coating on a flexible substrate. Blade coating was selected because it is

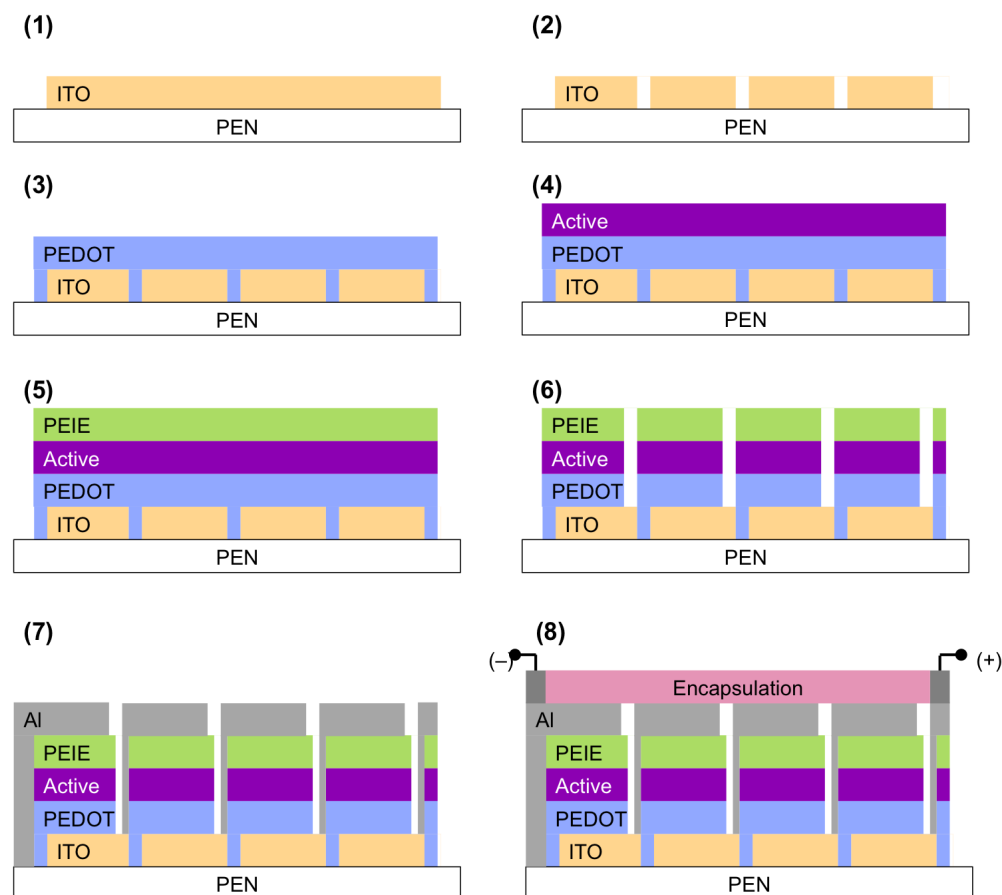


Figure 2.6: Process flow for fabrication of printed organic solar modules. (1) The process begins with an ITO-coated PEN substrate. (2) The ITO is etched to define cell areas. (3) PEDOT:PSS hole transport layer is deposited by blade coating. (4) Active layer is deposited by blade coating. (5) PEIE cathode interlayer is deposited by blade coating. (6) Organic layers are mechanically scribed to allow series connections. (7) Aluminum is evaporated to complete the cells and create series connections. (8) Silver paint contacts and encapsulation are applied to complete the module.

simple to perform on a small scale, and there are relatively few process variables to optimize: blade height, speed, and substrate temperature (in addition to the properties of the ink).

Figure 2.6 shows the fabrication process flow for the blade-coated solar modules. First, an ITO-coated polyethylene naphthalate (PEN) substrate (University Wafer) was etched in hydrochloric acid, using a Kapton tape mask to define cell areas. PEDOT:PSS (Clevios P VP AI 4083, diluted with 25% water) was blade coated at 90°C to form the hole transport layer, then baked at 160°C for 10 minutes to remove residual water. The samples were then transferred to a nitrogen glovebox for the remainder of the fabrication. The active layer solution, 1:3.7 PCDTBT:PC₇₁BM, with total concentration of 47 mg/ml in DCB with 10%

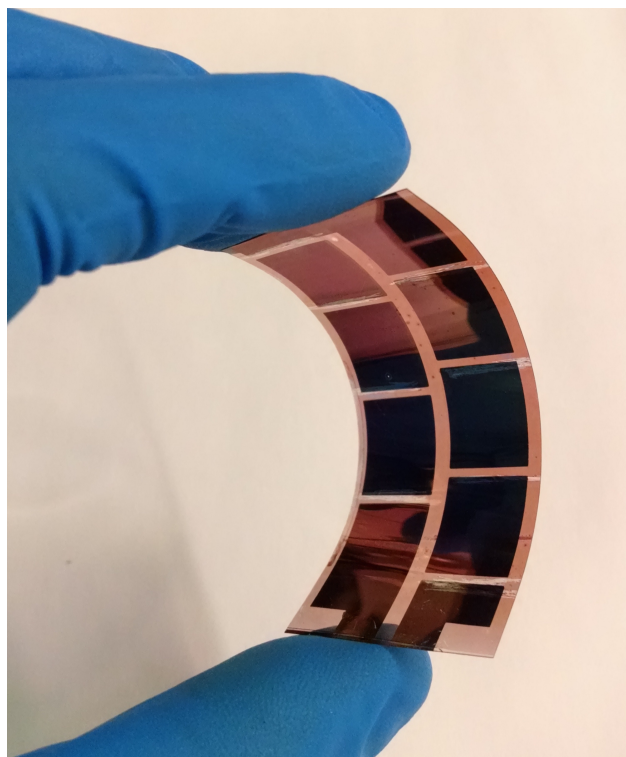


Figure 2.7: Photograph of 8-cell, monolithically integrated printed organic solar module.

DMSO, was blade coated at 80°C. PEIE, diluted to 0.048 wt% in ethanol, was blade coated at room temperature, then baked at 70°C for 10 minutes to remove residual solvent. All blade coating steps used a blade height of 200 μm and blade speed of about 0.8 m/min. To create series connections, the printed organic layers must be scribed to expose the underlying ITO. Here, this was done by mechanically scribing the layers using a wooden tool soaked in chlorobenzene. It can be accomplished with greater speed and precision (though with higher equipment cost) by laser scribing [37, 38]. Aluminum was thermally evaporated to form the cathodes of the cells, using a shadow mask which was aligned to the ITO patterns so that the edge of each cell's cathode overlapped slightly with the neighboring cell's anode as shown in Figure 2.6(7). Silver paint (Ted Pella) was applied to improve the durability of the module terminals. To increase the lifetime of the modules after removal from the glovebox, a PEN encapsulation layer was attached on top of the aluminum, using Delo Katiobond LP612 ultraviolet-curable epoxy.

A photograph of a finished printed module is shown in Figure 2.7. The modules consist of 8 cells, 1 \times 1 cm each, in a 2 \times 4 array. 2.5 mm of space was left between neighboring cells for the series connections, and an additional 2 mm was left between the two rows of cells. The total module dimensions, therefore, were 5 cm \times 2.2 cm, giving an aperture area of 11 cm² and geometric fill factor of 73%. Use of laser scribing could improve the geometric fill

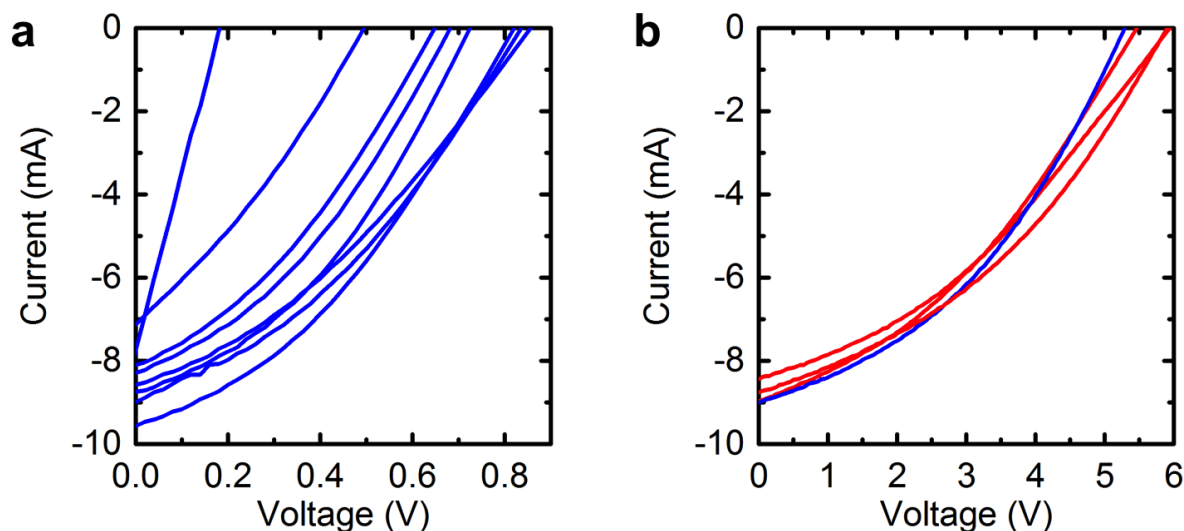


Figure 2.8: Performance of monolithically integrated printed OPV modules. (a) Current-voltage characteristics measured for the 8 printed organic solar cells that form one module. (b) Range of current-voltage characteristics measured for four printed organic solar modules, with 8 series-connected cells each, fabricated with the same process. The module consisting of the cells shown in (a) is identified by the blue line.

factor [37].

Four printed OPV modules were manufactured with this technique. Representative current-voltage characteristics for the 8 cells in one of the modules are shown in Figure 2.8a, while the characteristics of that entire module are shown (in blue) along with those of the other three modules (in red) in Figure 2.8b. It is clear from the cell data that leakage, leading to low shunt resistance, is a major factor limiting the performance of the modules. Two of the cells in Figure 2.8a, for example, show very significant shunt resistance issues, leading to low V_{oc} and fill factor. Other more minor variations in performance between cells may be due to non-uniformities in layer thicknesses, or drying time, which could influence the nanoscale morphology. Although there was a large spread in cell performance within each module, the current-voltage characteristics of the whole modules were remarkably similar to each other. The power conversion efficiency of the modules was 2.3% over the active area, or 1.7% over the aperture area. They produced a voltage of 5.7 ± 0.3 V at open circuit and 3.3 ± 0.2 V at maximum power point, again a useful range for lithium battery charging applications.

These results highlight an important challenge for monolithically integrated modules. When modules are produced by assembling individual cells, such as in Section 2.3, it is possible to select only high-performing cells to be incorporated into the module. For the monolithically integrated modules, on the other hand, it is not possible to select which cells to use. In this case, the consequence was that 8 cells were needed for the monolithic module to

reach the same voltages that could be achieved with 6 intentionally selected cells. Optimizing the thickness and uniformity of the organic layers, through tuning of the ink formulations and printing process parameters, could potentially improve upon these results. Greater uniformity and precision may also be achievable using slot-die coating, which has similar film formation physics to blade coating and can therefore use the same ink formulations and processing speeds [2, 39–41]. Then, in addition to the existing benefits of faster and easier manufacturing than assembled modules, monolithically integrated modules would also offer competitive performance.

2.5 Conclusion

This chapter has presented several fundamental design considerations for organic photovoltaic modules, using examples of spin-coated cells on glass as well as printed modules on flexible plastic. The choices of active layer materials, thickness, and processing conditions greatly impact cell voltage, current and efficiency. Similar power conversion efficiencies of 2.2% and 2.3% (over the active area) were obtained for small spin-coated cells using the glass/ITO/PEDOT:PSS/P3HT:PCBM/Al stack and for large-area printed 8-cell modules using the PEN/ITO/PEDOT:PSS/PCDTBT:PC₇₁BM/PEIE/Al stack, respectively. A higher power conversion efficiency of 5.3% is reported for spin-coated cells using the PCDTBT stack. For applications requiring a particular module voltage and current, the requirements can be met by connecting the appropriate number of cells in series and selecting the appropriate cell area, respectively.

The cell and module technologies discussed in this chapter are developed and applied further in several other chapters of the thesis. Spin-coated and blade-coated modules using the PCDTBT system are employed to charge batteries of two different chemistries in Chapters 4 and 5, respectively. Additionally, the P3HT cell is used as a model system in the following Chapter 3 to demonstrate the application of a new transparent electrode for photovoltaics.

2.6 References

1. Kaltenbrunner, M., White, M. S., Glowacki, E. D., Sekitani, T., Someya, T., Sariciftci, N. S. & Bauer, S. Ultrathin and lightweight organic solar cells with high flexibility. *Nature Communications* **3**, 770 (2012).
2. Krebs, F. C., Tromholt, T. & Jørgensen, M. Upscaling of polymer solar cell fabrication using full roll-to-roll processing. *Nanoscale* **2**, 873–886 (2010).
3. Lizin, S., Van Passel, S., De Schepper, E., Maes, W., Lutsen, L., Manca, J. & Vandezande, D. Life cycle analyses of organic photovoltaics: A review. *Energy & Environmental Science* **6**, 3136–3149 (2013).

4. Lungenschmied, C., Dennler, G., Neugebauer, H., Sariciftci, S. N., Glatthaar, M., Meyer, T. & Meyer, A. Flexible, long-lived, large-area, organic solar cells. *Solar Energy Materials and Solar Cells* **91**, 379–384 (2007).
5. Forberich, K., Guo, F., Bronnbauer, C. & Brabec, C. J. Efficiency limits and color of semitransparent organic solar cells for application in building-integrated photovoltaics. *Energy Technology* **3**, 1051–1058 (2015).
6. Günes, S., Neugebauer, H. & Sariciftci, N. S. Conjugated polymer-based organic solar cells. *Chemical Reviews* **107**, 1324–1338 (2007).
7. Brabec, C. J., Gowrisanker, S., Halls, J. J. M., Laird, D., Jia, S. & Williams, S. P. Polymer-fullerene bulk-heterojunction solar cells. *Advanced Materials* **22**, 3839–3856 (2010).
8. Po, R., Maggini, M. & Camaioni, N. Polymer solar cells: Recent approaches and achievements. *The Journal of Physical Chemistry C* **114**, 695–706 (2010).
9. Dou, L., You, J., Hong, Z., Xu, Z., Li, G., Street, R. A. & Yang, Y. 25th anniversary article: A decade of organic/polymeric photovoltaic research. *Advanced Materials* **25**, 6642–6671 (2013).
10. Peet, J., Senatore, M. L., Heeger, A. J. & Bazan, G. C. The role of processing in the fabrication and optimization of plastic solar cells. *Advanced Materials* **21**, 1521–1527 (2009).
11. Dang, M. T., Hirsch, L. & Wantz, G. P3HT:PCBM, best seller in polymer photovoltaic research. *Advanced Materials* **23**, 3597–3602 (2011).
12. Park, S. H., Roy, A., Beaupré, S., Cho, S., Coates, N., Moon, J. S., Moses, D., Leclerc, M., Lee, K. & Heeger, A. J. Bulk heterojunction solar cells with internal quantum efficiency approaching 100%. *Nature Photonics* **3**, 297–302 (2009).
13. He, Z., Zhong, C., Su, S., Xu, M., Wu, H. & Cao, Y. Enhanced power-conversion efficiency in polymer solar cells using an inverted device structure. *Nature Photonics* **6**, 593–597 (2012).
14. You, J., Dou, L., Yoshimura, K., Kato, T., Ohya, K., Moriarty, T., Emery, K., Chen, C.-C., Gao, J., Li, G. & Yang, Y. A polymer tandem solar cell with 10.6% power conversion efficiency. *Nature Communications* **4**, 1446 (2013).
15. Cabanetos, C., El Labban, A., Bartelt, J. A., Douglas, J. D., Mateker, W. R., Fréchet, J. M. J., McGehee, M. D. & Beaujuge, P. M. Linear side chains in benzo[1,2-b:4,5-b']dithiophene-thieno[3,4-c]pyrrole-4,6-dione polymers direct self-assembly and solar cell performance. *Journal of the American Chemical Society* **135**, 4656–4659 (2013).
16. Li, N. & Brabec, C. J. Air-processed polymer tandem solar cells with power conversion efficiency exceeding 10%. *Energy & Environmental Science* **8**, 2902–2909 (2015).

17. Li, G., Shrotriya, V., Huang, J., Yao, Y., Moriarty, T., Emery, K. & Yang, Y. High-efficiency solution processable polymer photovoltaic cells by self-organization of polymer blends. *Nature Materials* **4**, 864–868 (2005).
18. Chen, D., Nakahara, A., Wei, D., Nordlund, D. & Russell, T. P. P3HT/PCBM bulk heterojunction organic photovoltaics: correlating efficiency and morphology. *Nano Letters* **11**, 561–567 (2011).
19. Ostfeld, A. E., Catheline, A., Ligsay, K., Kim, K.-C., Chen, Z., Facchetti, A., Fogden, S. & Arias, A. C. Single-walled carbon nanotube transparent conductive films fabricated by reductive dissolution and spray coating for organic photovoltaics. *Applied Physics Letters* **105**, 253301 (2014).
20. Beaupré, S. & Leclerc, M. PCDTBT: En route for low cost plastic solar cells. *Journal of Materials Chemistry A* **1**, 11097 (2013).
21. Wakim, S., Beaupré, S., Blouin, N., Aich, B.-R., Rodman, S., Gaudiana, R., Tao, Y. & Leclerc, M. Highly efficient organic solar cells based on a poly(2,7-carbazole) derivative. *Journal of Materials Chemistry* **19**, 5351 (2009).
22. Zhang, F., Zhuo, Z., Zhang, J., Wang, X., Xu, X., Wang, Z., Xin, Y., Wang, J., Wang, J., Tang, W., Xu, Z. & Wang, Y. Influence of PC60BM or PC70BM as electron acceptor on the performance of polymer solar cells. *Solar Energy Materials and Solar Cells* **97**, 71–77 (2012).
23. Zhou, Y., Fuentes-Hernandez, C., Shim, J., Meyer, J., Giordano, A. J., Li, H., Winget, P., Papadopoulos, T., Cheun, H., Kim, J., Fenoll, M., Dindar, A., Haske, W., Najafabadi, E., Khan, T. M., Sojoudi, H., Barlow, S., Graham, S., Brédas, J.-L., Marder, S. R., Kahn, A. & Kippelen, B. A universal method to produce low-work function electrodes for organic electronics. *Science* **336**, 327–332 (2012).
24. Lechêne, B. P., Cowell, M., Pierre, A., Evans, J., Wright, P. K. & Arias, A. C. Organic solar cells and fully printed supercapacitors for indoor light energy harvesting. *Nano Energy* **26**, 631–640 (2016).
25. Moulé, A. & Meerholz, K. Minimizing optical losses in bulk heterojunction polymer solar cells. *Applied Physics B* **86**, 721–727 (2007).
26. Chu, T.-Y., Alem, S., Tsang, S.-W., Tse, S.-C., Wakim, S., Lu, J., Dennler, G., Waller, D., Gaudiana, R. & Tao, Y. Morphology control in polycarbazole based bulk heterojunction solar cells and its impact on device performance. *Applied Physics Letters* **98**, 253301 (2011).
27. Gupta, D., Bag, M. & Narayan, K. S. Area dependent efficiency of organic solar cells. *Applied Physics Letters* **93**, 163301 (2008).
28. Ostfeld, A. E., Gaikwad, A. M., Khan, Y. & Arias, A. C. High-performance flexible energy storage and harvesting system for wearable electronics. *Scientific Reports* **6**, 26122 (2016).

29. Zamarayeva, A. M., Gaikwad, A. M., Deckman, I., Wang, M., Khau, B., Steingart, D. A. & Arias, A. C. Fabrication of a high-performance flexible silver-zinc wire battery. *Advanced Electronic Materials* **2**, 1500296 (2016).
30. Kopola, P., Tuomikoski, M., Suhonen, R. & Maaninen, A. Gravure printed organic light emitting diodes for lighting applications. *Thin Solid Films* **517**, 5757–5762 (2009).
31. Irimia-Vladu, M., Troshin, P. A., Reisinger, M., Shmygleva, L., Kanbur, Y., Schwabegger, G., Bodea, M., Schwödiauer, R., Mumyatov, A., Fergus, J. W., Razumov, V. F., Sitter, H., Sariciftci, N. S. & Bauer, S. Biocompatible and biodegradable materials for organic field-effect transistors. *Advanced Functional Materials* **20**, 4069–4076 (2010).
32. Smaal, W., Kjellander, C., Jeong, Y., Tripathi, A., Putten, B. V. D., Facchetti, A., Yan, H., Quinn, J., Anthony, J., Myny, K., Dehaene, W. & Gelinck, G. Complementary integrated circuits on plastic foil using inkjet printed n- and p-type organic semiconductors: Fabrication, characterization, and circuit analysis. *Organic Electronics* **13**, 1686–1692 (2012).
33. Lochner, C. M., Khan, Y., Pierre, A. & Arias, A. C. All-organic optoelectronic sensor for pulse oximetry. *Nature Communications* **5**, 5745 (2014).
34. Uno, M., Kanaoka, Y., Cha, B.-S., Isahaya, N., Sakai, M., Matsui, H., Mitsui, C., Okamoto, T., Takeya, J., Kato, T., Katayama, M., Usami, Y. & Yamakami, T. Short-channel solution-processed organic semiconductor transistors and their application in high-speed organic complementary circuits and organic rectifiers. *Advanced Electronic Materials* **1**, 1500178 (2015).
35. Field, H. & Gabor, A. M. *Cell binning method analysis to minimize mismatch losses and performance variation in Si-based modules in Conference Record of the Twenty-Ninth IEEE Photovoltaic Specialists Conference, 2002* (IEEE, 2002), 418–421. doi:10.1109/PVSC.2002.1190548.
36. Krebs, F. C. Fabrication and processing of polymer solar cells: A review of printing and coating techniques. *Solar Energy Materials and Solar Cells* **93**, 394–412 (2009).
37. Kubis, P., Lucera, L., Machui, F., Spyropoulos, G., Cordero, J., Frey, A., Kaschta, J., Voigt, M. M., Matt, G. J., Zeira, E. & Brabec, C. J. High precision processing of flexible P3HT/PCBM modules with geometric fill factor over 95%. *Organic Electronics* **15**, 2256–2263 (2014).
38. Moon, S.-J., Yum, J.-H., Lofgren, L., Walter, A., Sansonnens, L., Benkhaira, M., Nicolay, S., Bailat, J. & Ballif, C. Laser-scribing patterning for the production of organometallic halide perovskite solar modules. *IEEE Journal of Photovoltaics* **5**, 1087–1092 (2015).
39. Chang, Y.-R., Chang, H.-M., Lin, C.-F., Liu, T.-J. & Wu, P.-Y. Three minimum wet thickness regions of slot die coating. *Journal of Colloid and Interface Science* **308**, 222–230 (2007).

40. Krebs, F. C., Fyenbo, J. & Jørgensen, M. Product integration of compact roll-to-roll processed polymer solar cell modules: methods and manufacture using flexographic printing, slot-die coating and rotary screen printing. *Journal of Materials Chemistry* **20**, 8994–9001 (2010).
41. Søndergaard, R. R., Hösel, M. & Krebs, F. C. Roll-to-roll fabrication of large area functional organic materials. *Journal of Polymer Science Part B: Polymer Physics* **51**, 16–34 (2013).

Chapter 3

Carbon Nanotube Transparent Electrodes for Photovoltaics

This chapter reports on solution-processed carbon nanotube transparent conductive films for photovoltaics, produced using a reductive dissolution process. These films show a nearly twofold improvement in the ratio of electrical conductivity to optical absorptivity versus those deposited from conventional aqueous dispersions, due to substantial de-aggregation and sizable nanotube lengths. The promise of these films as transparent electrodes has been demonstrated by their incorporation into organic solar cells with power conversion efficiency up to 2.3%, comparable to that of solar cells produced using standard indium tin oxide transparent electrodes. The carbon nanotube films offer improved flexibility and competitive performance compared to indium tin oxide on plastic substrates. Portions of the work in this chapter are published in [1].

3.1 Introduction

One of the great challenges in the field of organic electronics has been the replacement of the ubiquitous transparent electrode material, indium tin oxide (ITO), with an earth-abundant, low-cost, solution processable and flexible alternative [2–6]. While sputtered ITO films on glass offer very high transparency and low sheet resistance, ITO films on plastic substrates must be sputtered at a lower temperature and thus have poorer performance [7]. ITO films are also brittle, leading to irreparable cracking and failure of flexible electronic devices below a certain minimum bending radius [8]. In addition, due to the scarcity of indium and the large amount of energy required for deposition and patterning, ITO transparent electrodes are responsible for the vast majority of the energy consumption and cost of roll-to-roll fabricated organic devices such as organic photovoltaics (OPV) [3–5].

Several transparent conducting films (TCFs) have emerged as potential replacements for ITO, including conducting polymers [9], silver nanowires [10], graphene [6, 11], and single-walled carbon nanotubes (SWNTs). SWNTs are a promising alternative to ITO due to their

exceptional flexibility and conductivity; the great abundance of carbon; the potential for cost reduction due to economies of scale; and the ability to deposit nanotube networks from solution using additive, low-temperature printing and coating processes [6, 11–16]. Carbon nanotube TCFs have been successfully utilized in organic optoelectronic devices, including light-emitting diodes [12, 17–19], photodiodes [13], and photovoltaics [15, 16, 20–29], as well as transparent electronic devices such as capacitors, pressure sensors and strain sensors [30–33].

However, while SWNTs have the potential to form networks with simultaneously high conductivity and high transparency, experimentally measured conductivity of transparent SWNT networks tends to be much lower than that of ITO. This is in large part because the typical ink fabrication method, dispersing SWNTs in water with the aid of sonication, damages and shortens the SWNTs [24, 34]. Conductivity in thin SWNT networks follows percolation theory and is further limited by contact resistance at the tube-tube junctions. Therefore, to achieve high conductivity, a SWNT network should consist of individual tubes or small bundles, which have low contact resistance and a large number of percolation pathways, and the SWNTs should be of maximum length to minimize the number of junctions [35–37].

An alternative ink fabrication method known as reductive dissolution has been developed to produce solutions of highly dispersed and unbroken SWNTs [38–40]. In these processes, SWNTs are chemically reduced in the presence of an alkali metal either in liquid ammonia or in a naphthalenide solution in tetrahydrofuran. The reactive media is then removed, leaving a nanotubide salt that dissolves with only gentle mechanical stirring, without sonication, in a polar organic solvent such as dimethyl sulfoxide (DMSO) or dimethyl formamide. In this chapter, SWNT TCFs produced using the reductive dissolution technique demonstrate improved conductivity versus those deposited from aqueous dispersion. They also offer high performance on flexible plastic substrates. These SWNT TCFs are then employed in organic photovoltaic devices as the transparent anode.

3.2 Transparent conductive film fabrication and performance

Chemical vapor deposition (CVD) grown SWNTs were purified and processed at Linde Nanomaterials. SWNT ink fabrication, spray coating, and characterization by Raman spectroscopy and dynamic light scattering were all performed at Linde Nanomaterials by Dr. Amélie Catheline, Kathleen Ligsay, Dr. Kee-Chan Kim, and Dr. Siân Fogden. The organic SWNT ink (shown in Figure 3.1) was prepared using the liquid ammonia reductive dissolution technique developed by Fogden et al. [38, 39]. In this process, SWNTs were chemically reduced in the presence of sodium and liquid ammonia, and the resulting nanotubide salt was dissolved in DMSO with magnetic stirring. Processing and deposition of the organic ink was performed in a glovebox. After deposition by spray coating onto glass substrates, the



Figure 3.1: Photograph of a vial of organic SWNT ink, containing well-dispersed SWNTs in DMSO without sonication or surfactant.

films were maintained under clean dry air overnight to oxidize the nanotube to the neutral species. An aqueous SWNT dispersion was also produced, by sonicating SWNTs in water with sodium dodecylbenzenesulfonate surfactant, and deposited under ambient conditions by spray coating. For both organic and aqueous inks, the substrates were heated to 120°C during spray coating to ensure rapid drying and uniform coverage. Various SWNT film thicknesses were deposited, using multiple layers to produce thicker films ranging in thickness from about 20 to 100 nm. Thickness of the SWNT films was determined by scratching the films and measuring the step height with atomic force microscopy (AFM). Both aqueous and organic SWNT films were immersed in a solution of nitric acid (at least 1M) diluted to 10% in isopropanol, to remove residual surfactant or alkali metal salt and to p-dope the nanotubes. UV-visible transmittance and Raman spectroscopy showed no significant changes after the nitric acid treatment, indicating no significant damage to the nanotubes.

Figure 3.2 shows transmission electron micrographs (TEM) of SWNTs cast from the organic (a) and aqueous (b) inks; several micrographs from each ink were used to determine the bundle size distributions (c). Many individual nanotubes can be seen in the micrograph of the organic ink, and the vast majority of bundles were less than 10 nm in diameter. The aqueous ink, on the other hand, showed larger bundle sizes, very few individual tubes, and the presence of residual surfactant between the nanotubes even after the washing step. Dynamic light scattering, known as an efficient technique to analyze the SWNT length as described by Lucas et al. [34], confirmed that the SWNTs in the organic ink maintained

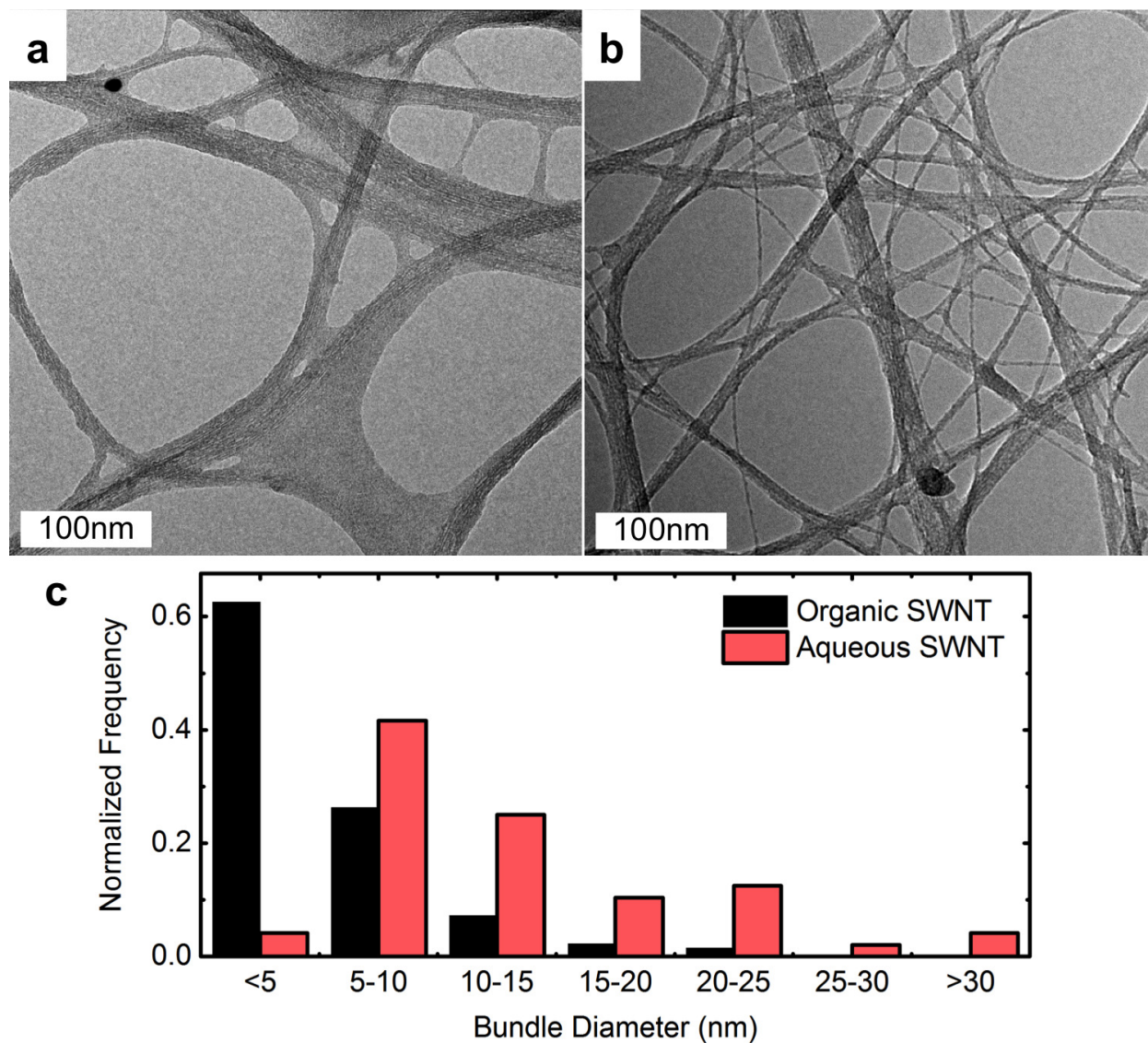


Figure 3.2: Transmission electron micrographs of SWNTs deposited from (a) aqueous and (b) organic inks. (c) Bundle size distributions for organic and aqueous inks [1]. Images taken by Dr. Amélie Catheline.

their original length of $\sim 20 \mu\text{m}$, while those in the aqueous dispersion were shortened to $1.9 \pm 0.2 \mu\text{m}$, considerably shorter than their original length [1].

The performance of a TCF is often quantified by the figure of merit (FOM) given by the ratio of the optical absorptivity to the electrical conductivity:

$$FOM = -R_{sheet} \ln(T) \quad (3.1)$$

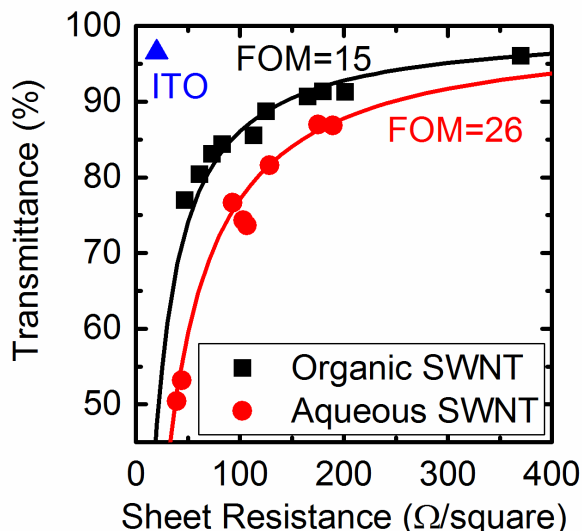


Figure 3.3: Sheet resistance and transmittance at 550 nm wavelength of SWNT films deposited from aqueous and organic inks, compared to a commercially available ITO film. The black and red solid lines correspond to constant FOM of 15 and 26, respectively.

where R_{sheet} is the sheet resistance in Ω/\square and T is the optical transmittance at $\lambda = 550$ nm. Thus, a lower FOM value indicates a higher performing TCF. For organic photovoltaics an FOM of 10 is considered adequate if a metal grid is used in conjunction with the TCF, while without a metal grid the FOM should be $\sim 10\times$ lower to minimize resistive losses [41].

To determine the FOM, the sheet resistance of the SWNT TCFs was measured using the 4-point probe technique, while the transmittance was measured by UV-visible spectroscopy. Sheet resistance and transmittance values are shown in Figure 3.3 for SWNT films of various thicknesses: the thinner the film, the more transparent. The performance of an ITO film on glass (Thin Film Devices, $20 \Omega/\square$, transmittance of 96.5%) is also shown. Due to the considerable SWNT length, smaller bundle size, and absence of surfactant, TCFs from the reductive process ink consistently afforded higher performance (average FOM = 15, minimum 12) than those from the aqueous dispersion (average FOM = 26, minimum 24). The performance of the aqueous SWNT film is in good agreement with that previously reported in the literature for spray-deposited aqueous dispersions [13], while the organic SWNT is competitive with some of the best performing carbon nanotube films [42–46]. AFM, transmittance, and spot-to-spot Raman measurements showed good uniformity and consistent results for each film. An AFM micrograph for an organic SWNT film, showing the topographical uniformity of the film, is given in Figure 3.4a.

Spin coating was also explored as a deposition method for the SWNT films, as it is a simple but powerful technique for fabricating prototype organic electronic devices. Similar FOMs were achieved for spin-coated SWNT films as for spray-coated films from the same inks. However, due to the low concentration of both organic and aqueous SWNT inks,

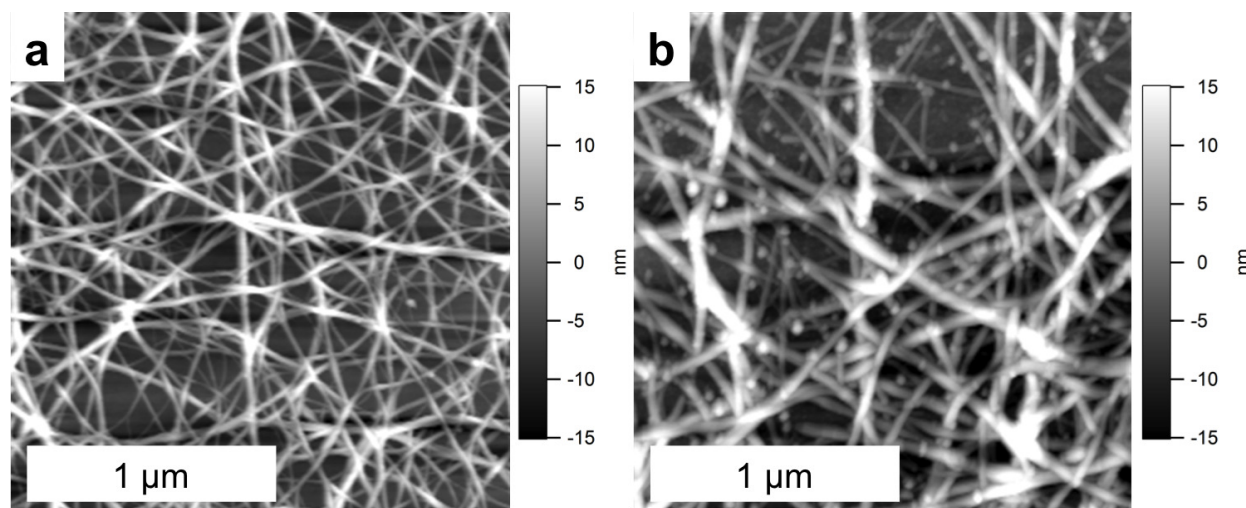


Figure 3.4: AFM images of SWNT films (a) spray-cast and (b) spin-cast from organic ink.

many sequential coats of ink were required to reach the sheet resistance range of interest for transparent electrode applications. Furthermore, since the substrates were at room temperature during spin coating, rather than the elevated temperatures used during spray coating, long spin times (> 1 minute) were needed to ensure adequate drying of the high-boiling point solvents. As a result, the spin-cast films exhibited poorer uniformity and greater aggregation of the nanotubes, as shown in the AFM image in Figure 3.4b. Thus, since spray coating produced higher quality films more quickly, and is also more suitable for large-scale and roll-to-roll production processes, it was selected as the SWNT film deposition method for the subsequent studies.

3.3 Flexible transparent conductive films

SWNTs are an appealing transparent electrode material for flexible electronics due to their excellent mechanical flexibility and the ability to deposit high-quality films at low enough temperatures to be compatible with plastic substrates. ITO, by contrast, is brittle, and films deposited at low temperature on plastic tend to have lower performance than those deposited at high temperature on glass [7, 8]. To assess the benefits of the reductive dissolution SWNT films for flexible applications, SWNT films were deposited on polyethylene terephthalate (PET) and polyethylene naphthalate (PEN) substrates, and their flexibility and electrical performance were compared with a commercially available ITO film on PET (Aldrich, $60 \Omega/\square$, 88% transmittance). The substrate temperature during spray coating was reduced from 120°C to 90°C to maintain the mechanical integrity of the plastic. Figure 3.5 shows a photograph of one of the flexible SWNT TCFs.

As shown in Figure 3.6a, both sheet resistance and transmittance of the ITO on PET,

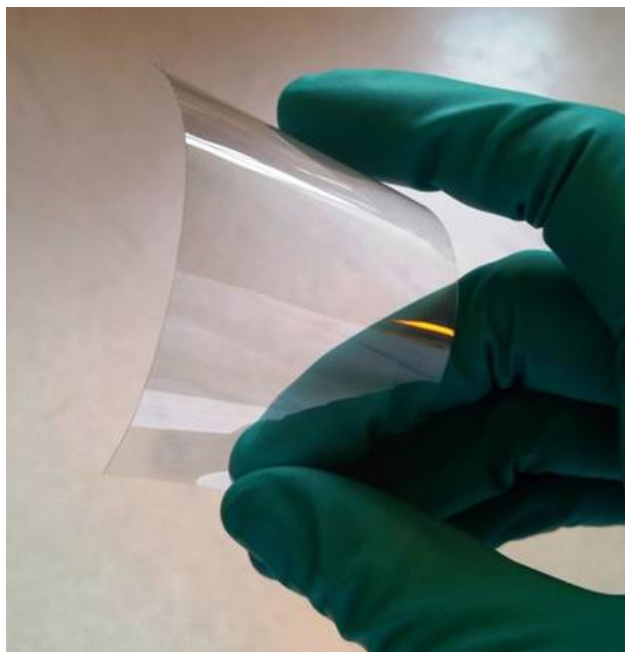


Figure 3.5: Photograph of a flexible transparent conductive film of SWNTs on a PET substrate.

which are typical for off-the-shelf ITO/PET films, are distinctly inferior to the ITO film on glass. For the SWNT films, on the other hand, the reduction in substrate temperature during spray coating on the PET had only a modest impact on the drying process, and no discernible impact on the properties of the SWNTs themselves. As a result, the performance of the SWNT films on PET was nearly identical to that of films on glass over a range of thicknesses, as shown in Figure 3.6a. The gap in performance between SWNT and ITO is therefore much smaller when flexibility is a requirement: the difference in FOM is only a factor of two on PET, compared to a factor of 20 on glass.

The flexibility of SWNT and ITO films on PET was assessed by measuring the sheet resistance of the films after bending to increasingly small radii of curvature. The ITO sheet resistance increased by 15% after bending to a 5.8 mm radius, and increased sevenfold when the bending radius was reduced to 4.8 mm, as shown in Figure 3.6b. The SWNT film, on the other hand, could be bent to a radius of 0.8 mm before a 15% increase in sheet resistance occurred, and even after folding and creasing the film (a bending radius approaching zero) the sheet resistance only increased by a factor of 2.5. These findings are in good agreement with previous studies of SWNT and ITO flexibility [12, 21]. Thus, in addition to their competitive optoelectronic performance compared to ITO on PET, the greater flexibility of SWNT films can offer a greater range of potential applications in flexible electronics.

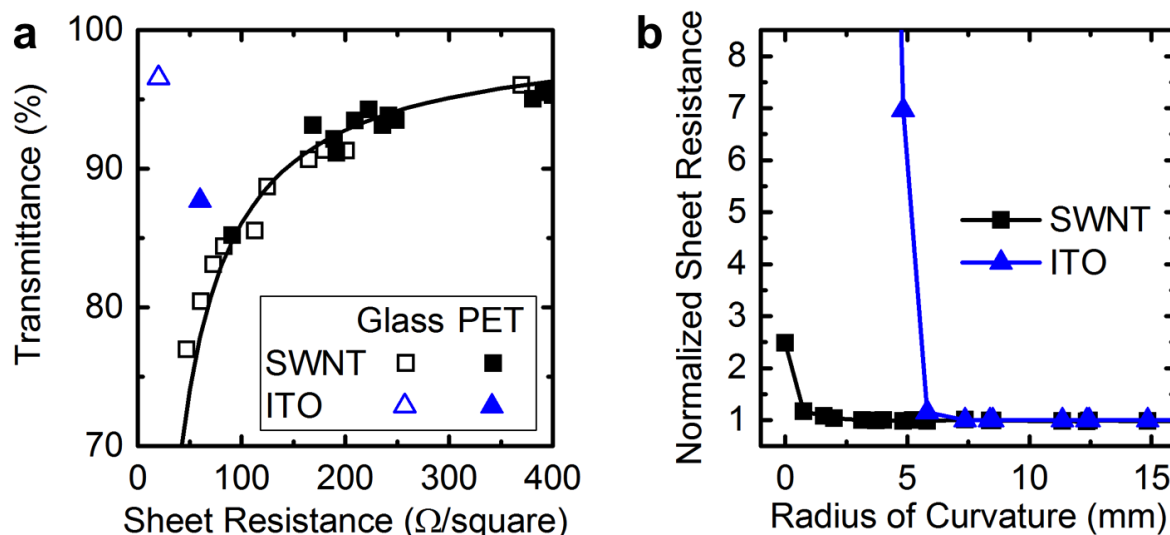


Figure 3.6: (a) Sheet resistance and transmittance at 550 nm wavelength of ITO and SWNT films on glass and PET. The black line corresponds to FOM of 15. (b) Sheet resistance of SWNT and ITO films on PET after bending to increasingly small radii, normalized to the sheet resistance of the flat film.

3.4 Applications in organic photovoltaics

The suitability of the organic SWNT films as a transparent electrode was assessed through their integration into OPV devices. OPVs were fabricated using thin ($311 \Omega/\square$, 93% transmittance) and thick ($78 \Omega/\square$, 78% transmittance) organic SWNT films on glass substrates, and compared with control devices fabricated on ITO-coated glass slides. A 40-nm-thick hole transporting layer of poly(3,4-ethylenedioxythiophene): poly(styrenesulfonate) (PEDOT:PSS, Clevis P VP AI 4083, mixed with 3% DMSO and 22% isopropanol to improve its conductivity and ability to wet the SWNT film) was spin-cast onto the TCFs and baked at 130°C for 10 minutes. The active layer, a 220-nm-thick bulk heterojunction of 1:1 poly(3-hexylthiophene) (P3HT, Polyera) and [6,6]-phenyl- C_{61} -butyric acid methyl ester (PCBM, SES Research) was spin-cast from a 1,2-dichlorobenzene solution and solvent annealed at room temperature under a petri dish overnight. Aluminum cathodes were deposited by thermal evaporation, and the solar cells were annealed at 150°C for 10 minutes. All active layer solution preparation and film processing was carried out in a glovebox. Each sample was patterned with several small cells (3 mm^2 each) with three different distances to the anode contact, as shown in Figure 3.7, to investigate the impact of this distance on the series resistance and fill factor (FF) of the resulting devices.

Figure 3.8 shows AFM images after the deposition of a 40-nm-thick PEDOT:PSS hole transporting layer (a) and a 220-nm-thick P3HT:PCBM bulk heterojunction active layer (b). The PEDOT:PSS partially filled the voids between nanotubes in the SWNT network,

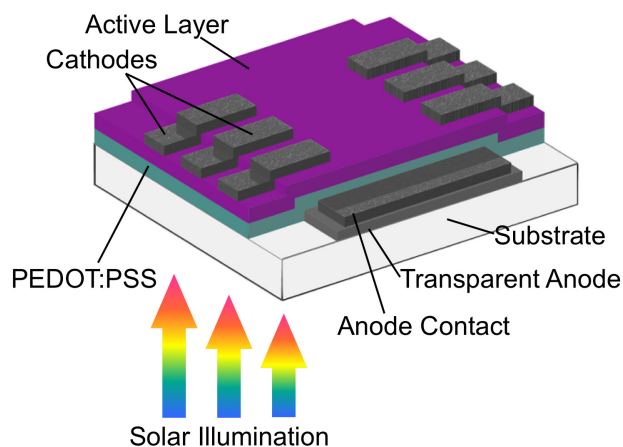


Figure 3.7: Illustration of the structure of organic solar cells used in this work.

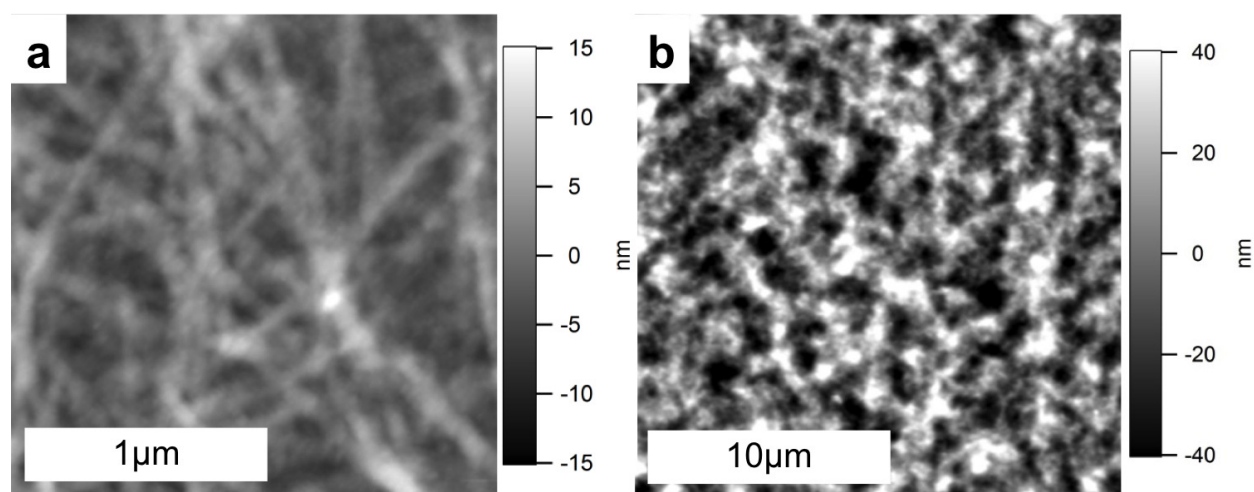


Figure 3.8: (a) AFM image of SWNT TCF coated with 40 nm of PEDOT:PSS. (b) AFM image of 220 nm thick P3HT:PCBM bulk heterojunction active layer on PEDOT:PSS-coated SWNT.

reducing the root-mean-square (RMS) surface roughness from about 10 nm to about 3 nm, although some texture from the SWNT network is still visible at the top of the PEDOT:PSS film. The addition of PEDOT:PSS also reduced the SWNT film sheet resistance by about 30% and the transmittance by about 4%. The much thicker bulk heterojunction active layer covered the remainder of the SWNT network topography.

Table 3.1 summarizes the performances obtained for the ITO- and SWNT-based solar cells, as measured under simulated air mass 1.5 global illumination. The ITO and thin SWNT each gave an average power conversion efficiency of 2.2% and maximum efficiencies of 2.5% and 2.3%, respectively. Figure 3.9a shows typical J-V characteristics for solar cells

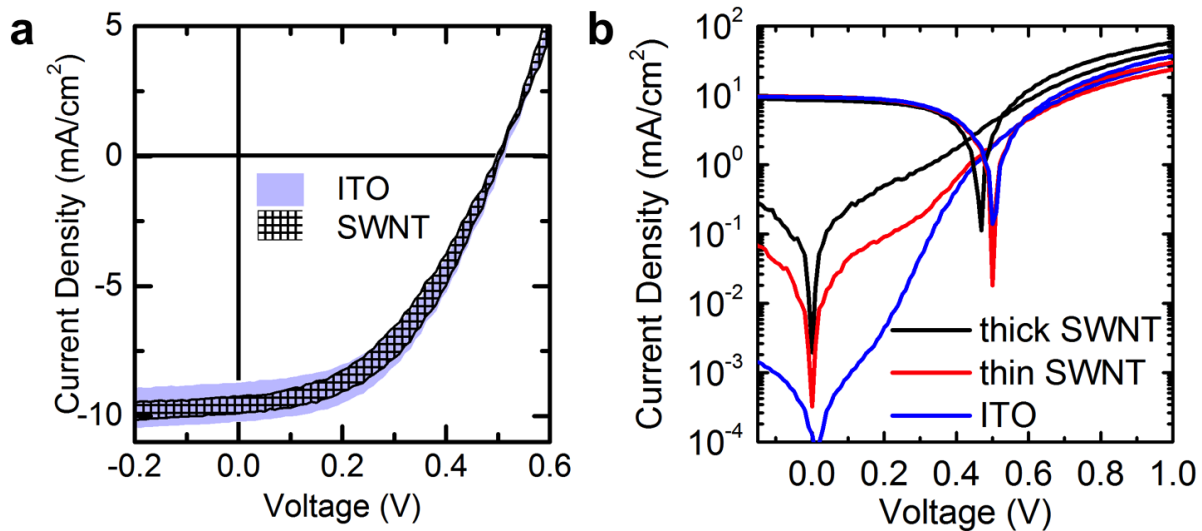


Figure 3.9: (a) Current density-voltage characteristics of solar cells using ITO and SWNT transparent electrodes. The light blue area corresponds to the typical J-V curve range for ITO-based solar cells and the crosshatched area corresponds to the typical range for cells with the thin SWNT transparent electrode. (b) Solar cell current density-voltage characteristics on a logarithmic scale, in the dark and under illumination.

Table 3.1: Average solar cell performance parameters using ITO, thin SWNT (311 Ω/\square , 93%T), and thick SWNT (78 Ω/\square , 78%T) transparent electrodes. Highest values of power conversion efficiency achieved for each TCF are given in parentheses.

TCF	V_{oc} (V)	J_{sc} (mA/cm ²)	FF	Efficiency (%)
ITO	0.50	9.4	0.47	2.2 (2.5)
SWNT, thin	0.50	9.6	0.45	2.2 (2.3)
SWNT, thick	0.47	8.6	0.52	2.1 (2.1)

with these two transparent electrodes, indicating that the performance of cells with the thin SWNT transparent electrode lies well within the typical range of the ITO solar cell performances. The devices using the thick SWNT film, however, had increased leakage currents due to the higher SWNT film roughness, resulting in a lower open-circuit voltage, as shown in Figure 3.9b. The lower transmittance of the thicker SWNT film also reduced the short-circuit current density slightly.

It is important to note that the highest OPV performance with the thin SWNT film was obtained with the shortest distance to the anode contact, which is 1 mm. The disadvantage of a transparent electrode with high sheet resistance such as this SWNT film is that it increases the series resistance of the solar cell, reducing the fill factor. This effect is amplified when charge carriers must travel a long distance within the transparent electrode before reaching

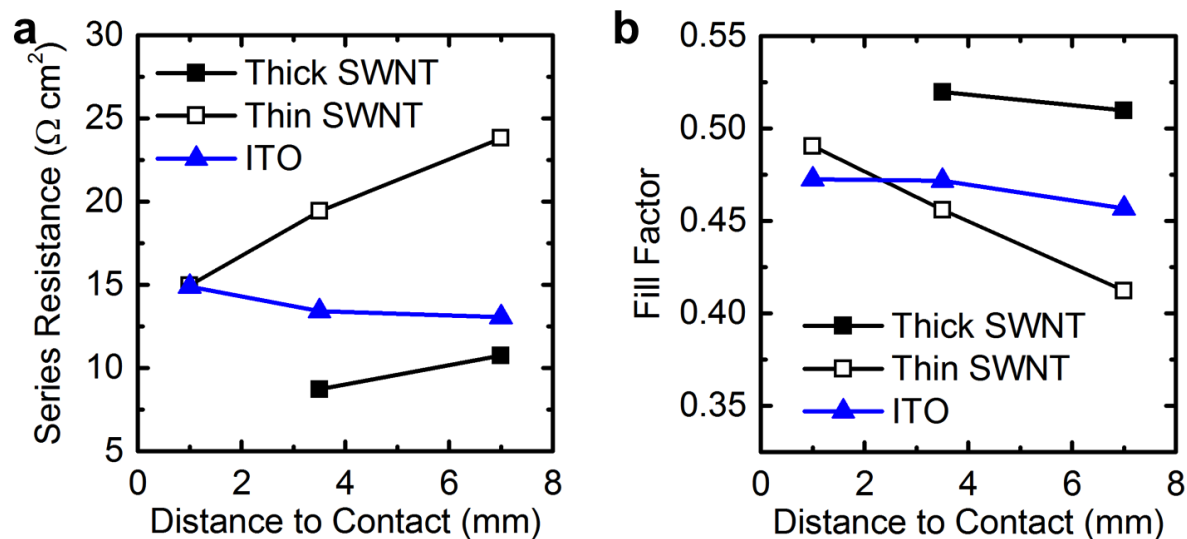


Figure 3.10: (a) Series resistance and (b) fill factor of organic solar cells versus distance to the anode contact.

a lower-resistance, opaque metal contact. Figures 3.10a and b show the increase in series resistance and reduction in fill factor, respectively, as the distance to the anode contact is increased. With the longest distance (7 mm), the effect of the series resistance was so severe for the solar cell with the thin SWNT film that the efficiency decreased to 2.0%, below that of the thick SWNT film. Cells with the lower-resistance TCFs (thick SWNT and ITO), on the other hand, had lower series resistance and a less significant reduction in FF for the longer distances.

Finally, flexible solar cells were demonstrated using a SWNT TCF on a flexible PEN substrate, as shown in Figure 3.11a. These cells employed a spray-cast organic SWNT film of intermediate thickness, with sheet resistance of $91 \Omega/\square$ and transmittance of 85%. The typical current-voltage characteristics obtained for the flexible solar cells are shown in Figure 3.11b. These cells also included a 1-nm-thick layer of lithium fluoride, evaporated on top of the active layer prior to depositing the aluminum, which has been previously shown to increase the V_{oc} and efficiency of OPV devices [47]. In this case, the V_{oc} was approximately 0.53 V, a slight improvement over the values reported in Table 3.1. The cells demonstrated an average power conversion efficiency of 1.8%.

3.5 Conclusion

SWNT transparent conductive films fabricated via reductive dissolution have been demonstrated as viable electrodes for photovoltaics. The films displayed improved conductivity-absorptivity ratios compared to films cast from a conventional aqueous dispersion method,

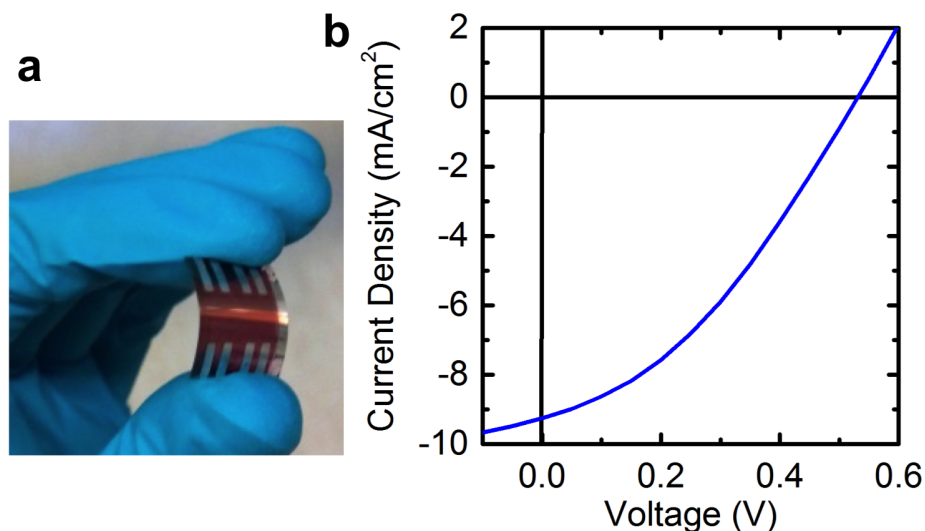


Figure 3.11: (a) Photograph and (b) current density-voltage characteristics of flexible solar cells using a SWNT transparent electrode.

due to the presence of individual, unbroken nanotubes. Deposition via a scalable spray coating process was shown to produce films with good spatial uniformity and minimal aggregation of the SWNTs. The SWNT films are competitive with ITO transparent electrodes on plastic substrates, but have much greater mechanical flexibility, showing little change in sheet resistance even after bending to sub-1mm bending radius.

The SWNT films have been integrated as the transparent electrode in organic solar cells on glass and flexible plastic substrates, using the standard active layer of P3HT:PCBM. Thicker SWNT films led to solar cells with slightly lower open-circuit voltage and short-circuit current, due to relatively high leakage currents and low transmittance, but with the highest fill factor. Thinner SWNT films, on the other hand, gave performance nearly identical to that of solar cells using ITO, but increasing the distance to the anode contact increased the series resistance and reduced the fill factor, due to the higher TCF sheet resistance. Overall, average power conversion efficiencies of 2.2% were achieved with both the thin SWNT film and the ITO.

For applications in large area modules, OPV devices should have higher efficiencies and larger active area than those presented in this work. Higher efficiencies can be achieved through further optimization of the processing conditions for the P3HT:PCBM, the use of alternative active layer materials (see, e.g., Pierre et al. [48] and Lechêne et al. [49]), or an interlayer between active layer and cathode to reduce the work function [50]. To achieve larger active areas while minimizing losses due to series resistance, it will be necessary to add a metal grid to the SWNT film, as has been proposed in the past to supplement SWNT [21, 51], PEDOT:PSS [9], and ITO [52] TCFs. This requirement will become even more stringent if a lower-bandgap donor polymer or a fullerene with higher absorption is

used in the active layer, as the increase in photocurrent density would increase the resistive losses. The thin SWNT films could also find applications in solar cells designed for indoor light harvesting, where the effect of the series resistance would be negligible due to the reduced current. In this case, the reduced leakage compared to thicker SWNT films, and the improved transmittance compared to aqueous dispersion films of similar resistance, would be important features. Overall, the enhancement in TCF conductivity achieved with the reductive dissolution process represents an important step toward the viability of SWNT films as an ITO replacement for organic optoelectronics.

3.6 References

1. Ostfeld, A. E., Catheline, A., Ligsay, K., Kim, K.-C., Chen, Z., Facchetti, A., Fogden, S. & Arias, A. C. Single-walled carbon nanotube transparent conductive films fabricated by reductive dissolution and spray coating for organic photovoltaics. *Applied Physics Letters* **105**, 253301 (2014).
2. Krebs, F. C. Fabrication and processing of polymer solar cells: A review of printing and coating techniques. *Solar Energy Materials and Solar Cells* **93**, 394–412 (2009).
3. Espinosa, N., García-Valverde, R., Urbina, A. & Krebs, F. C. A life cycle analysis of polymer solar cell modules prepared using roll-to-roll methods under ambient conditions. *Solar Energy Materials and Solar Cells* **95**, 1293–1302 (2011).
4. Lizin, S., Van Passel, S., De Schepper, E., Maes, W., Lutsen, L., Manca, J. & Vanderzande, D. Life cycle analyses of organic photovoltaics: A review. *Energy & Environmental Science* **6**, 3136–3149 (2013).
5. Mulligan, C. J., Wilson, M., Bryant, G., Vaughan, B., Zhou, X., Belcher, W. J. & Dastoor, P. C. A projection of commercial-scale organic photovoltaic module costs. *Solar Energy Materials and Solar Cells* **120**, 9–17 (2014).
6. Du, J., Pei, S., Ma, L. & Cheng, H.-M. 25th anniversary article: Carbon nanotube- and graphene-based transparent conductive films for optoelectronic devices. *Advanced Materials* **26**, 1958–91 (2014).
7. Lungenschmied, C., Dennler, G., Neugebauer, H., Sariciftci, S. N., Glatthaar, M., Meyer, T. & Meyer, A. Flexible, long-lived, large-area, organic solar cells. *Solar Energy Materials and Solar Cells* **91**, 379–384 (2007).
8. Chen, Z., Cotterell, B., Wang, W., Guenther, E. & Chua, S.-J. A mechanical assessment of flexible optoelectronic devices. *Thin Solid Films* **394**, 201–205 (2001).
9. Manceau, M., Angmo, D., Jørgensen, M. & Krebs, F. C. ITO-free flexible polymer solar cells: From small model devices to roll-to-roll processed large modules. *Organic Electronics* **12**, 566–574 (2011).
10. Gaynor, W., Lee, J.-Y. & Peumans, P. Fully solution-processed inverted polymer solar cells with laminated nanowire electrodes. *ACS Nano* **4**, 30–34 (2010).

11. Arthur, D., Silvy, R. P., Wallis, P., Tan, Y., Rocha, J.-D. R., Resasco, D., Praino, R. & Hurley, W. Carbon nanomaterial commercialization: Lessons for graphene from carbon nanotubes. *MRS Bulletin* **37**, 1297–1306 (2012).
12. Hu, L., Li, J., Liu, J., Gruner, G. & Marks, T. Flexible organic light-emitting diodes with transparent carbon nanotube electrodes: Problems and solutions. *Nanotechnology* **21**, 155202 (2010).
13. Falco, A., Cinà, L., Scarpa, G., Lugli, P. & Abdellah, A. Fully-sprayed and flexible organic photodiodes with transparent carbon nanotube electrodes. *ACS Applied Materials & Interfaces* **6**, 10593–10601 (2014).
14. Wu, Z., Chen, Z., Du, X., Logan, J. M., Sippel, J., Nikolou, M., Kamaras, K., Reynolds, J. R., Tanner, D. B., Hebard, A. F. & Rinzler, A. G. Transparent, conductive carbon nanotube films. *Science* **305**, 1273–1276 (2004).
15. Van de Lagemaat, J., Barnes, T. M., Rumbles, G., Shaheen, S. E., Coutts, T. J., Weeks, C., Levitsky, I., Peltola, J. & Glatkowski, P. Organic solar cells with carbon nanotubes replacing In₂O₃:Sn as the transparent electrode. *Applied Physics Letters* **88**, 233503 (2006).
16. Cho, D.-Y., Eun, K., Choa, S.-H. & Kim, H.-K. Highly flexible and stretchable carbon nanotube network electrodes prepared by simple brush painting for cost-effective flexible organic solar cells. *Carbon* **66**, 530–538 (2014).
17. Zhang, D., Ryu, K., Liu, X., Polikarpov, E., Ly, J., Tompson, M. E. & Zhou, C. Transparent, conductive, and flexible carbon nanotube films and their application in organic light-emitting diodes. *Nano Letters* **6**, 1880–1886 (2006).
18. Williams, C. D., Robles, R. O., Zhang, M., Li, S., Baughman, R. H. & Zakhidov, A. A. Multiwalled carbon nanotube sheets as transparent electrodes in high brightness organic light-emitting diodes. *Applied Physics Letters* **93**, 183506 (2008).
19. Chien, Y.-M., Lefevre, F., Shih, I. & Izquierdo, R. A solution processed top emission OLED with transparent carbon nanotube electrodes. *Nanotechnology* **21**, 134020 (2010).
20. Du Pasquier, A., Unalan, H. E., Kanwal, A., Miller, S. & Chhowalla, M. Conducting and transparent single-wall carbon nanotube electrodes for polymer-fullerene solar cells. *Applied Physics Letters* **87**, 203511 (2005).
21. Rowell, M. W., Topinka, M. A., McGehee, M. D., Prall, H.-J., Dennler, G., Sariciftci, N. S., Hu, L. & Gruner, G. Organic solar cells with carbon nanotube network electrodes. *Applied Physics Letters* **88**, 233506 (2006).
22. Kymakis, E., Stratakis, E. & Koudoumas, E. Integration of carbon nanotubes as hole transport electrode in polymer/fullerene bulk heterojunction solar cells. *Thin Solid Films* **515**, 8598–8600 (2007).

23. Feng, Y., Ju, X., Feng, W., Zhang, H., Cheng, Y., Liu, J., Fujii, A., Ozaki, M. & Yoshino, K. Organic solar cells using few-walled carbon nanotubes electrode controlled by the balance between sheet resistance and the transparency. *Applied Physics Letters* **94**, 123302 (2009).
24. Tenent, R. C., Barnes, T. M., Bergeson, J. D., Ferguson, A. J., To, B., Gedvilas, L. M., Heben, M. J. & Blackburn, J. L. Ultrasoft, large-area, high-uniformity, conductive transparent single-walled-carbon-nanotube films for photovoltaics produced by ultrasonic spraying. *Advanced Materials* **21**, 3210–3216 (2009).
25. Barnes, T. M., Bergeson, J. D., Tenent, R. C., Larsen, B. A., Teeter, G., Jones, K. M., Blackburn, J. L. & van de Lagemaat, J. Carbon nanotube network electrodes enabling efficient organic solar cells without a hole transport layer. *Applied Physics Letters* **96**, 243309 (2010).
26. Kim, S., Yim, J., Wang, X., Bradley, D. D., Lee, S. & DeMello, J. C. Spin- and spray-deposited single-walled carbon-nanotube electrodes for organic solar cells. *Advanced Functional Materials* **20**, 2310–2316 (2010).
27. Tyler, T. P., Brock, R. E., Karmel, H. J., Marks, T. J. & Hersam, M. C. Electronically monodisperse single-walled carbon nanotube thin films as transparent conducting anodes in organic photovoltaic devices. *Advanced Energy Materials* **1**, 785–791 (2011).
28. Kim, Y. H., Sachse, C., Zakhidov, A. A., Meiss, J., Zakhidov, A. A., Müller-Meskamp, L. & Leo, K. Combined alternative electrodes for semi-transparent and ITO-free small molecule organic solar cells. *Organic Electronics* **13**, 2422–2428 (2012).
29. Kymakis, E., Stylianakis, M. M., Spyropoulos, G. D., Stratakis, E., Koudoumas, E. & Fotakis, C. Spin coated carbon nanotubes as the hole transport layer in organic photovoltaics. *Solar Energy Materials and Solar Cells* **96**, 298–301 (2012).
30. Feng, C., Liu, K., Wu, J.-S., Liu, L., Cheng, J.-S., Zhang, Y., Sun, Y., Li, Q., Fan, S. & Jiang, K. Flexible, stretchable, transparent conducting films made from superaligned carbon nanotubes. *Advanced Functional Materials* **20**, 885–891 (2010).
31. Lipomi, D. J., Vosgueritchian, M., Tee, B. C.-K., Hellstrom, S. L., Lee, J. A., Fox, C. H. & Bao, Z. Skin-like pressure and strain sensors based on transparent elastic films of carbon nanotubes. *Nature Nanotechnology* **6**, 788–792 (2011).
32. Sorel, S., Khan, U. & Coleman, J. N. Flexible, transparent dielectric capacitors with nanostructured electrodes. *Applied Physics Letters* **101**, 103106 (2012).
33. Cai, L., Song, L., Luan, P., Zhang, Q., Zhang, N., Gao, Q., Zhao, D., Zhang, X., Tu, M., Yang, F., Zhou, W., Fan, Q., Luo, J., Zhou, W., Ajayan, P. M. & Xie, S. Superstretchable, transparent carbon nanotube-based capacitive strain sensors for human motion detection. *Scientific Reports* **3**, 3048 (2013).
34. Lucas, A., Zakri, C., Maugey, M., Pasquali, M., Schoot, P. V. D. & Poulin, P. Kinetics of nanotube and microfiber scission under sonication. *The Journal of Physical Chemistry C* **113**, 20599–20605 (2009).

35. Hecht, D., Hu, L. & Gruner, G. Conductivity scaling with bundle length and diameter in single walled carbon nanotube networks. *Applied Physics Letters* **89**, 133112 (2006).
36. Lyons, P. E., De, S., Blighe, F., Nicolosi, V., Pereira, L. F. C., Ferreira, M. S. & Coleman, J. N. The relationship between network morphology and conductivity in nanotube films. *Journal of Applied Physics* **104**, 044302 (2008).
37. Nirmalraj, P. N., Lyons, P. E., De, S., Coleman, J. N. & Boland, J. J. Electrical connectivity in single-walled carbon nanotube networks. *Nano Letters* **9**, 3890–3895 (2009).
38. Fogden, S., Kim, K.-C., Ma, C., Ligsay, K. & McFarlane, G. *Scalable single walled carbon nanotube separation: From process to product* in *Nanotechnology 2011: Advanced Materials, CNTs, Particles, Films and Composites* (eds Laudon, M. & Romanowicz, B. F.) **1** (Nano Science and Technology Institute, Boston, 2011), 163–166.
39. Fogden, S., Howard, C. A., Heenan, R. K., Skipper, N. T. & Shaffer, M. S. P. Scalable method for the reductive dissolution, purification, and separation of single-walled carbon nanotubes. *ACS Nano* **6**, 54–62 (2012).
40. Pénicaud, A., Poulin, P., Derré, A., Anglaret, E. & Petit, P. Spontaneous dissolution of a single-wall carbon nanotube salt. *Journal of the American Chemical Society* **127**, 8–9 (2005).
41. Rowell, M. W. & McGehee, M. D. Transparent electrode requirements for thin film solar cell modules. *Energy & Environmental Science* **4**, 131 (2011).
42. Shin, D.-W., Lee, J. H., Kim, Y.-H., Yu, S. M., Park, S.-Y. & Yoo, J.-B. A role of HNO₃ on transparent conducting film with single-walled carbon nanotubes. *Nanotechnology* **20**, 475703 (2009).
43. Kaskela, A., Nasibulin, A. G., Timmermans, M. Y., Aitchison, B., Papadimitratos, A., Tian, Y., Zhu, Z., Jiang, H., Brown, D. P., Zakhidov, A. & Kauppinen, E. I. Aerosol-synthesized SWCNT networks with tunable conductivity and transparency by a dry transfer technique. *Nano Letters* **10**, 4349–4355 (2010).
44. Liu, W.-B., Pei, S., Du, J., Liu, B., Gao, L., Su, Y., Liu, C. & Cheng, H.-M. Additive-free dispersion of single-walled carbon nanotubes and its application for transparent conductive films. *Advanced Functional Materials* **21**, 2330–2337 (2011).
45. Xiao, G., Tao, Y., Lu, J., Zhang, Z. & Kingston, D. Efficient fabrication of highly conductive and transparent carbon nanotube thin films on polymer substrates. *Journal of Materials Science* **46**, 3399–3404 (2011).
46. Mirri, F., Ma, A. W. K., Hsu, T. T., Behabtu, N., Eichmann, S. L., Young, C. C., Tsentelovich, D. E. & Pasquali, M. High-performance carbon nanotube transparent conductive films by scalable dip coating. *ACS Nano* **6**, 9737–9744 (2012).

47. Brabec, C. J., Shaheen, S. E., Winder, C., Sariciftci, N. S. & Denk, P. Effect of LiF/metal electrodes on the performance of plastic solar cells. *Applied Physics Letters* **80**, 1288 (2002).
48. Pierre, A., Lu, S., Howard, I. A., Facchetti, A. & Arias, A. C. Empirically based device modeling of bulk heterojunction organic photovoltaics. *Journal of Applied Physics* **113**, 154506 (2013).
49. Lechêne, B. P., Cowell, M., Pierre, A., Evans, J., Wright, P. K. & Arias, A. C. Organic solar cells and fully printed supercapacitors for indoor light energy harvesting. *Nano Energy* **26**, 631–640 (2016).
50. Zhou, Y., Fuentes-Hernandez, C., Shim, J., Meyer, J., Giordano, A. J., Li, H., Winget, P., Papadopoulos, T., Cheun, H., Kim, J., Fenoll, M., Dindar, A., Haske, W., Najafabadi, E., Khan, T. M., Sojoudi, H., Barlow, S., Graham, S., Brédas, J.-L., Marder, S. R., Kahn, A. & Kippelen, B. A universal method to produce low-work function electrodes for organic electronics. *Science* **336**, 327–332 (2012).
51. Wang, J., Zhang, J., Sundramoorthy, A. K., Chen, P. & Chan-Park, M. B. Solution-processed flexible transparent conductors based on carbon nanotubes and silver grid hybrid films. *Nanoscale* **6**, 4560–4565 (2014).
52. Choi, S., Potscavage, W. J. & Kippelen, B. Area-scaling of organic solar cells. *Journal of Applied Physics* **106**, 054507 (2009).

Chapter 4

Design of a Wearable Energy Harvesting and Storage Accessory

In this chapter, an organic photovoltaic module is designed for integration with a flexible wire battery into a wearable energy harvesting and storage bracelet. The impacts of the light source and illuminance on the power conversion efficiency of the solar module, the energy conversion and storage efficiency of the system, and the daily energy harvesting potential are investigated. Portions of this chapter have been submitted for publication in [1].

4.1 Introduction

One key area enabled by printed and flexible electronics is that of wearable systems for health and wellness applications. A vast array of wearable health sensors have been developed in recent years based on flexible and stretchable devices, for example to sense heart rate, blood pressure, body temperature, and blood oxygenation [2]. While some self-powered sensing elements such as piezoelectric pressure sensors and thermoelectric temperature sensors have been demonstrated [3–7], most devices require power to drive the sensing elements. In addition to the demands of the sensor itself, power is required to analyze the data collected and to communicate or display the result. The power demands of many wearable systems are on the order of a few milliwatts, and some are as low as a few microwatts [2, 8]. The basic requirement of power sources for these applications is to provide whatever power is needed without disrupting the wearer’s mobility or comfort. To avoid plugging wires into the module, on-board energy storage and reliable energy harvesting with sufficient capacity must be present. These power sources should be located near the sensor module, to minimize wiring and the associated resistive losses, discomfort, and system complexity.

Photovoltaics are of particular interest for powering wearable devices because the power density available from sunlight and even indoor light is relatively large compared to other ambient sources [9, 10]. Several novel solar cell structures have been demonstrated recently for wearable electronics applications, including flexible thin-film solar cells [11–14] and wire-

or fiber-shaped photovoltaic materials that can be woven into textiles [15–22]. Organic photovoltaics (OPV) are especially well suited for wearable applications because they can be flexible and lightweight, consist of non-toxic materials [23, 24], have low embodied energy [25], perform well under indoor light [26], and can be made in various colors to address aesthetic considerations [27]. Similarly, a number of flexible batteries have been developed for applications in wearable electronics, including many with wire or fiber architecture that can be twisted, wrapped, or woven into textiles [28–31]. Despite the advances in wearable energy harvesting and storage devices independently, though, relatively few studies have focused on the use of wearable solar cells to charge wearable batteries, particularly under the lighting conditions typically experienced by people in their daily routine [32–34].

While most wearable power sources are designed for integration into patches or clothing, accessories such as jewelry are also worn by many people and present an opportunity for the integration of power sources. In particular, a power source in the form of a bracelet would be ideal to power wearable sensors on the wrist, a location in which a number of biosignals can be measured [2]. Although flexibility is frequently mentioned as a strict requirement for wearable electronics, jewelry is an exception as it often contains a combination of rigid and flexible structures. Thus, a wide range of potential jewelry-integrated power source designs can be explored that include both rigid and flexible devices.

This chapter presents a wearable energy harvesting and storage bracelet based on an organic photovoltaic module and a wire-shaped silver-zinc battery. The voltage of the photovoltaic module is selected in order to charge the battery directly without the addition of circuitry such as maximum power point tracking. To determine how much energy would be available during a normal day from such an accessory, the effects of light source and illuminance on photovoltaic module performance are investigated. The rate and efficiency of battery charging from the photovoltaic module are characterized under sunlight and indoor lighting conditions, and battery charging profiles through typical workday lighting conditions are studied.

4.2 Experimental details

For the organic solar modules, indium tin oxide (ITO) coated glass substrates (Thin Film Devices) patterned with 4 stripes of ITO were cleaned in acetone followed by isopropanol, then plasma cleaned for 5 minutes. Poly(3,4-ethylenedioxythiophene): polystyrene sulfonate (PEDOT:PSS, Clevis P VP AI 4083) was spin-cast onto the ITO glass at 4000 rpm and baked on a hot plate at 130°C for 10 minutes. The active layer solution was made from poly[N-9'-heptadecanyl-2,7-carbazole-alt-5,5-(4,7-di-2-thienyl-2',1',3'-benzothiadiazole)] (PCDTBT, Saint-Jean Photochimie) and [6,6]-phenyl-C₇₁-butyric acid methyl ester (PC₇₁BM, Solaris) in a 1:3.7 weight ratio, with total concentration of 21 mg/ml, in 1,2-dichlorobenzene with 5% dimethyl sulfoxide. After heating overnight at 80°C to dissolve, the active layer solution was spin-cast in the glovebox at 1250 rpm to form a film with thickness of 55 nm, as measured with a Dektak profilometer. Polyethyleneimine ethoxylated (PEIE, Sigma-Aldrich) diluted

to 0.048 wt% in ethanol was spin-cast onto the samples at 1250 rpm. Samples were then baked at 70°C for 10 minutes. The organic layers were mechanically scribed to allow series connections to be made between the cells. 100 nm of aluminum was thermally evaporated to complete the modules. Modules were encapsulated using Delo Katiobond LP612 ultraviolet-curable epoxy and either glass or polyethylene naphthalate. The dimensions of each cell were 1.5×0.2 cm, giving an active area of 0.3 cm^2 . The size of the 4-cell modules, including the active area of the cells, the spaces between them and the contact areas, was 1.8×1.14 cm. Module efficiency was calculated based on this area, 2.05 cm^2 .

Batteries were fabricated by Alla Zamarayeva according to the procedure outlined in [1]. The batteries had silver-zinc chemistry and flexible wire architecture, previously studied in [35]. Battery current collectors were connected to the corresponding OPV module terminals using conductive epoxy (Circuit Works TDS CW 2400). Simulated air mass 1.5 solar illumination was provided using an Oriel Sol1A solar simulator. Indoor illumination was provided using either a compact fluorescent lamp (CFL, GE Energy Smart Daylight CFL 6500K) or light-emitting diode (LED, Feit Electric Dimmable A19 LED 3000 K) bulb. The height of the bulbs above the solar module was adjusted to produce either 300 lux or 3000 lux, using a Hamamatsu S2387-66R silicon photodiode to measure the power and a Thorlabs CCS200 spectrophotometer to measure the lamp spectra. A Keithley 2400 source-meter was used to measure the current-voltage characteristics of the OPV modules and to record the current and voltage during solar battery charging.

4.3 System components

4.3.1 Batteries

A silver-zinc alkaline chemistry was selected for the batteries because it is non-toxic, less reactive than lithium chemistries, and relies on an aqueous electrolyte [1]. These characteristics make silver-zinc batteries ideal for applications such as wearable devices where they will be in close contact with the human body [35, 36]. Furthermore, they are rechargeable and have high energy density [37, 38]. The batteries were made with a wire architecture so that they could wrap around the wrist to form a bracelet. The battery length was designed to provide a capacity of $\sim 6 \text{ mWh}$, a typical daily energy requirement for a low duty cycle resistive sensor system [39]. Fabrication and characterization of the batteries was performed by Alla Zamarayeva.

Typical charge-discharge curves for the batteries are shown in Figure 4.1 [1]. Charging and discharging rates of $C/4$ and $C/2$ were used, respectively, corresponding to a full charge in 4 hours and a full discharge in 2 hours. As seen in the figure, the battery voltage ranged from 1.6 V to 1.8 V during charging, and the battery capacity was approximately 4.7 mAh. These characteristics must be considered in the design of the solar module. The battery voltage must be considered because if the solar module is connected directly to the battery, without power conversion electronics, its voltage will be identical to the battery's. The battery

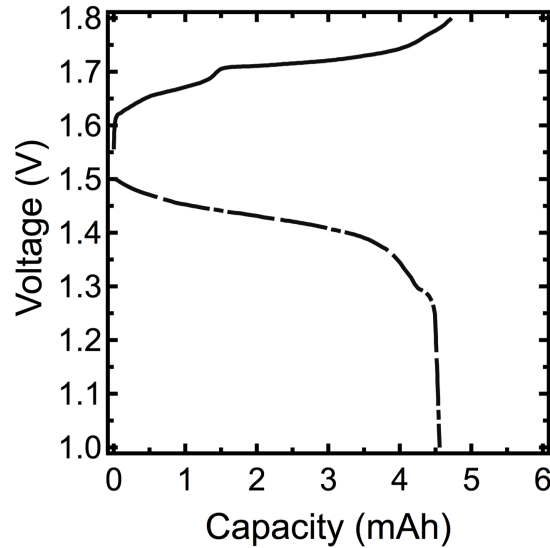


Figure 4.1: Charge (solid line) and discharge (dotted line) characteristics of the silver-zinc wire battery operated at $C/4$ charge rate and $C/2$ discharge rate [1]. Data collected by Alla Zamarayeva.

capacity is important because it sets the size of the solar module required to charge the battery in the desired amount of time. For example, if a full charge in 4 hours is desired, the solar module should be designed to produce an average current of 1.2 mA during charging. The current of the solar module depends on the materials used, the cell dimensions, the illumination conditions, and the voltage at which it is operated. Therefore, it is crucial to consider all of these variables in the design of the solar module and characterize its output under a realistic set of illumination conditions.

4.3.2 Solar modules

OPV modules were designed with conventional architecture as shown in Figure 4.2a, based on a PCDTBT:PC₇₁BM bulk heterojunction active layer. The modules used ITO coated glass substrates, a hole transport layer of PEDOT:PSS, and the cathode was aluminum with a dipole interlayer of PEIE. Glass substrates are known to be an excellent barrier against oxygen and moisture permeation into the organic solar cell, in addition to withstanding the high temperatures required for deposition of high quality ITO films [26]. Although flexibility is a requirement for electronics integrated into clothing or in close contact with skin, jewelry designs frequently use glass and other rigid materials, allowing the use of glass substrates for OPV modules in jewelry. Additionally, since wearable devices are expected to experience indoor light levels much of the time, the OPV modules were optimized for low light. It was previously reported that increasing the thickness of the cathode interlayer leads to improved low-light performance due to a reduction in dark current [40]. Thus, the OPV modules in

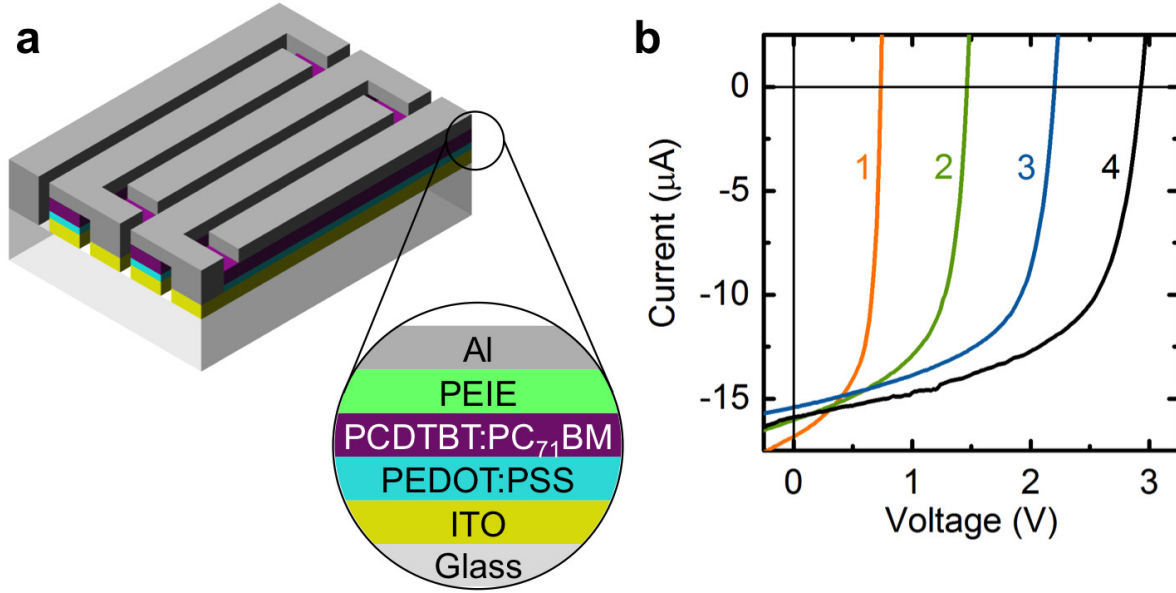


Figure 4.2: (a) Structure of 4-cell organic photovoltaic module. Structure drawn by Jerica Duey. (b) Current-voltage characteristics of 1-4 OPV cells in series, under CFL with illuminance of 300 lux.

Table 4.1: Performance parameters of single OPV cells and 4-cell modules, with dimensions of 1.5×0.2 cm per cell, under various lighting conditions.

Lighting		V_{OC} (V)	I_{SC} (mA)	FF	Module PCE (%)
Sunlight	Cell	0.87 ± 0.05	3.1 ± 0.3	0.45 ± 0.04	
	Module	3.6 ± 0.1	3.0 ± 0.1	0.42 ± 0.07	
CFL, 300 lux	Cell	0.72 ± 0.01	0.016 ± 0.001	0.60 ± 0.02	
	Module	2.7 ± 0.3	0.016 ± 0.0003	0.57 ± 0.06	
CFL, 3000 lux	Cell	0.81 ± 0.01	0.15 ± 0.01	0.62 ± 0.01	
	Module	3.1 ± 0.3	0.151 ± 0.006	0.61 ± 0.02	
LED, 300 lux	Module	2.4 ± 0.2	0.0082 ± 0.0001	0.54 ± 0.06	4.9 ± 0.5
LED, 3000 lux	Module	2.8 ± 0.3	0.075 ± 0.003	0.60 ± 0.02	5.9 ± 0.8

this work used the concentration and spin coating speed identified by Lechêne et al. to deposit the PEIE layer of optimum thickness.

Up to four cells, 1.5×0.2 cm each, were fabricated in series on a single substrate to form OPV modules. The cells and modules were characterized under 1-sun; 300 lux illuminance, a typical lighting condition for offices and other indoor locations [40]; as well as 3000 lux, corresponding to a location several centimeters below a typical indoor light source. The indoor light was provided with either a CFL or LED bulb. Performance parameters of cells

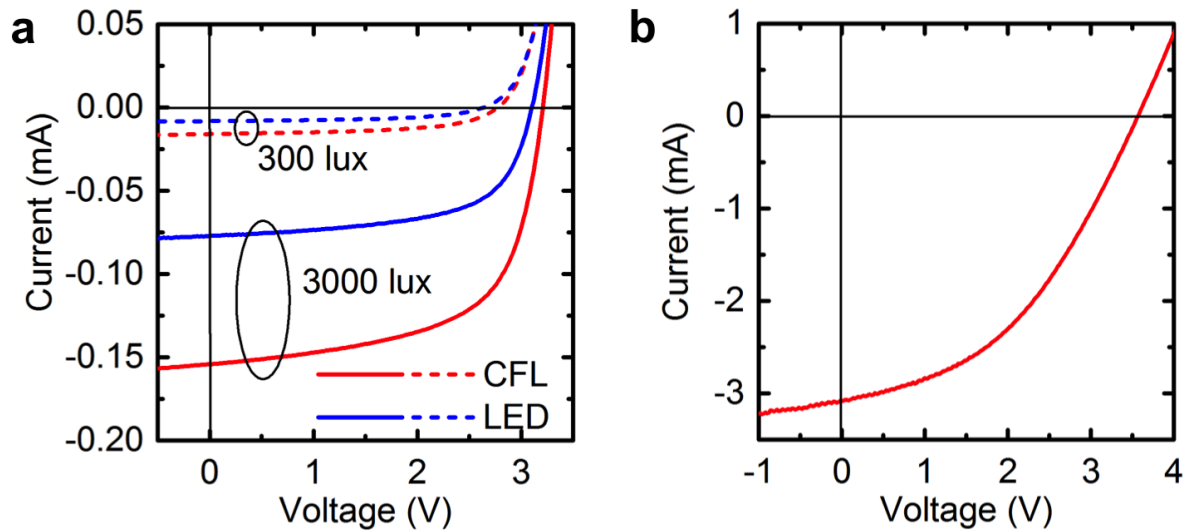


Figure 4.3: Current-voltage characteristics of 4-cell OPV module under various indoor lighting conditions (a) and sunlight (b).

and 4-cell modules under these conditions, as well as under simulated sunlight, are given in Table 4.1. Module power conversion efficiency (PCE) was calculated based on a 2.05 cm^2 module area, which includes the four cells themselves as well as the areas between them. Figure 4.2b shows the typical current-voltage characteristics of OPV modules with one to four series-connected cells, under CFL lighting of 300 lux. The module voltage is equal to the sum of the individual cell voltages, as expected, and the current and fill factor show little change as more cells are added in series, indicating that the cells are well matched. The 4-cell modules produce $25 \mu\text{W}$ of power under this lighting condition, which is adequate for many low-power electronics including radio frequency identification (RFID) and e-ink displays [8].

Figure 4.3a compares the output of the 4-cell modules under CFL and LED illumination of 300 and 3000 lux. Since the illuminance is weighted by the sensitivity of the human eye, light sources with the same illuminance (lux) but a different spectrum will provide a different irradiance (W/m^2). The irradiance corresponding to an illuminance of 300 lux is $0.180 \text{ mW}/\text{cm}^2$ for the CFL and $0.104 \text{ mW}/\text{cm}^2$ for the LED. The CFL emission spectrum also has a greater overlap with the absorption spectrum of the PCDTBT:PC₇₁BM active layer than the LED does [40]. The combination of these two factors resulted in 2x higher photocurrent and 30% higher PCE under the CFL than under the LED. Since the dark current of the OPV modules was low, on the order of 10^{-7} to $10^{-8} \text{ A}/\text{cm}^2$ at $\pm 0.5 \text{ V}$ bias as shown in Figure 4.4, leakage current was not expected to be a significant loss mechanism even under the low lighting of 300 lux. This was confirmed by the minimal difference in fill factor between the 300 lux and 3000 lux conditions. The $\sim 20\%$ increase in PCE when the illuminance was increased from 300 to 3000 lux was mainly due to the increase in open-circuit voltage. Overall, the CFL at 3000 lux resulted in the highest module PCE of 7.8%.

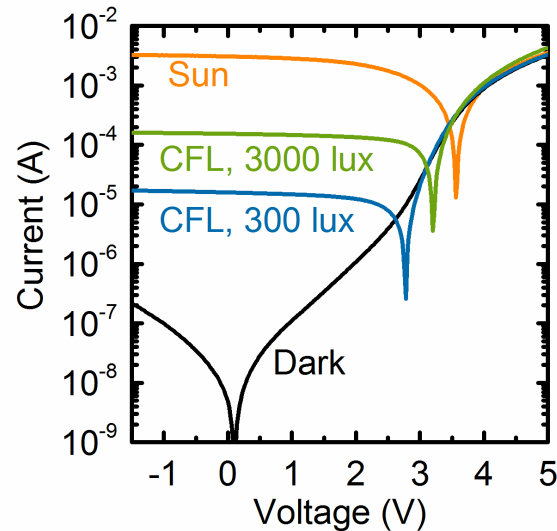


Figure 4.4: Semilog plot of the current-voltage characteristics of 4-cell OPV modules under sunlight, CFL with illuminance of 300 and 3000 lux, and in the dark.

The performance of the OPV module under simulated solar illumination is given in Figure 4.3b. The efficiency was lower than with the CFL or LED lighting, 2.2%, in part because a smaller portion of the solar spectrum lies within the active layer’s absorption window. The fill factor was also significantly reduced (from $>55\%$ to 45%) due to the increased impact of series resistance resulting from the higher current and particular module geometry. Nevertheless, the maximum power output under sunlight was 5 mW, sufficient to power many types of wearable health monitoring systems [39, 41, 42].

The performance of single OPV cells with a different geometry, 1.0×0.475 cm, under the same lighting conditions is included in Figure 4.5 and Table 4.2 for comparison. The fill factor, and therefore the power conversion efficiency, of these cells is notably higher than that of the 1.5×0.2 cm cells under sunlight, due to the reduced series resistance of this lower aspect ratio cell geometry. Under the lower lighting conditions, the losses due to series resistance are reduced for the 1.5×0.2 cm cells due to the lower current, and the fill factors are therefore more similar for the two geometries.

In the design of standalone solar cells and modules, open-circuit voltage, power conversion efficiency and maximum power point are common figures of merit used to quantify photovoltaic performance. However, when designing solar modules to be directly connected to batteries, the value of most interest is the power output over the battery voltage range during charging, which is ~ 1.6 - 1.8 V for the silver-zinc batteries employed in this work. Figure 4.6 shows the power output of OPV modules with 1-4 series-connected cells under sunlight and CFL lighting. Although the battery voltage range is closer to the maximum power point of a 3-cell solar module than that of a 4-cell module, the 4-cell module was selected for battery charging because it provides greater total power and therefore a faster charging

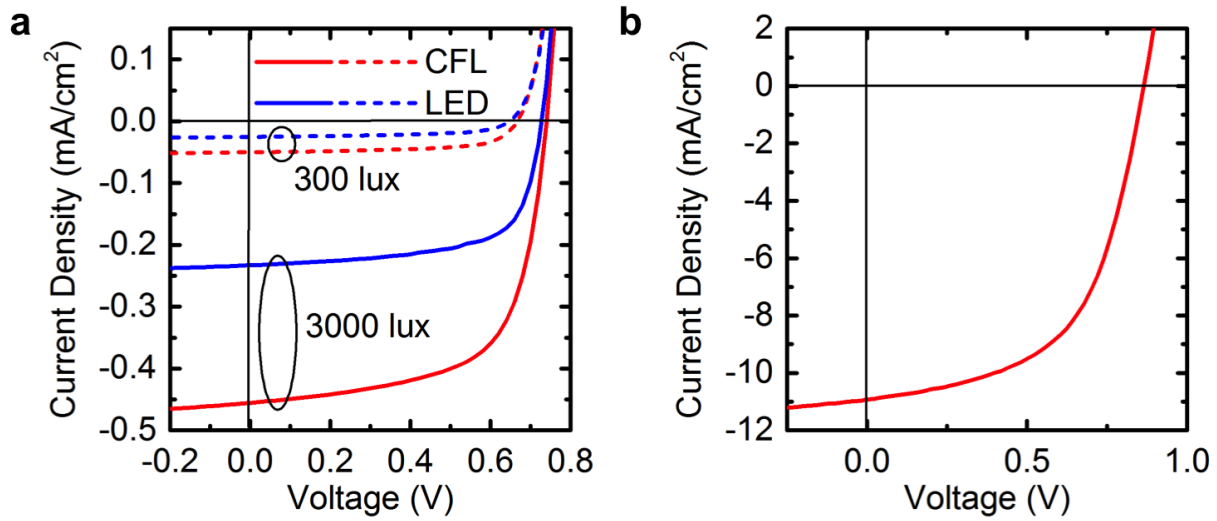


Figure 4.5: Current density-voltage characteristics of OPV cells with dimensions of 1.0×0.475 cm (area of 0.475 cm²) under various indoor lighting conditions (a) and sunlight (b).

Table 4.2: Performance parameters of OPV cells with dimensions of 1.0×0.475 cm (area of 0.475 cm²) under sunlight and various indoor lighting conditions.

Lighting	V_{OC} (V)	J_{SC} (mA/cm ²)	FF	Efficiency (%)
Sunlight	0.87 ± 0.02	10.9 ± 0.2	0.56 ± 0.02	5.3 ± 0.2
CFL, 300 lux	0.68 ± 0.03	0.0501 ± 0.0009	0.65 ± 0.02	12 ± 1
CFL, 3000 lux	0.74 ± 0.03	0.46 ± 0.02	0.66 ± 0.02	12 ± 1
LED, 300 lux	0.65 ± 0.03	0.0252 ± 0.0003	0.6 ± 0.1	9 ± 2
LED, 3000 lux	0.73 ± 0.02	0.233 ± 0.005	0.67 ± 0.01	11.0 ± 0.6

rate over that range. Additionally, since the battery voltage was below the maximum power point voltage of the 4-cell module, the module would be expected to produce nearly constant current during the entire charging period, particularly under the indoor lighting conditions when the fill factor is high. Furthermore, the open-circuit voltage of the 4-cell modules is well above the maximum battery voltage under all lighting conditions tested, leaving a sufficient margin for a blocking diode to be inserted between the OPV module and battery if needed in the future.

4.4 Solar battery charging

The OPV modules and batteries were connected together to characterize the solar charging process in a wearable energy harvesting and storage system. Figure 4.7 shows photographs of a bracelet consisting of a 4-cell OPV module with a wire battery integrated into the

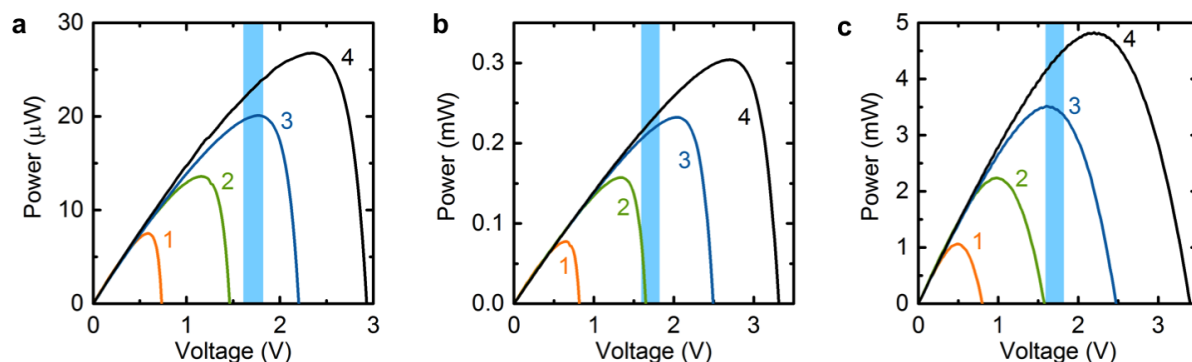


Figure 4.6: Power-voltage characteristics of 1-4 OPV cells in series, under CFL with illuminance of (a) 300 lux or (b) 3000 lux and (c) 1-sun. The blue shaded region represents the range of battery voltage during charging, 1.6-1.8V.



Figure 4.7: Photographs of photovoltaic module and wire battery integrated into a wearable bracelet [1]. Photographs taken by Alla Zamarayeva.

wristband, an example design of an energy harvesting and storage accessory. Since the OPV module was designed to have nearly constant current and near-maximum power output in the voltage range of the battery, interfacing electronics such as maximum power point tracking were not determined to be unnecessary. The OPV module was therefore connected directly to the battery, maintaining it at the same voltage as the battery throughout charging. The voltage across and current flowing into the battery during 12 hours of charging under the 3000 lux CFL are given in Figure 4.8a, showing the increase in battery voltage as it charged as well as the stability of the OPV module current. Figure 4.8b shows the voltage and current as the battery was charged completely under simulated sunlight. The duration of

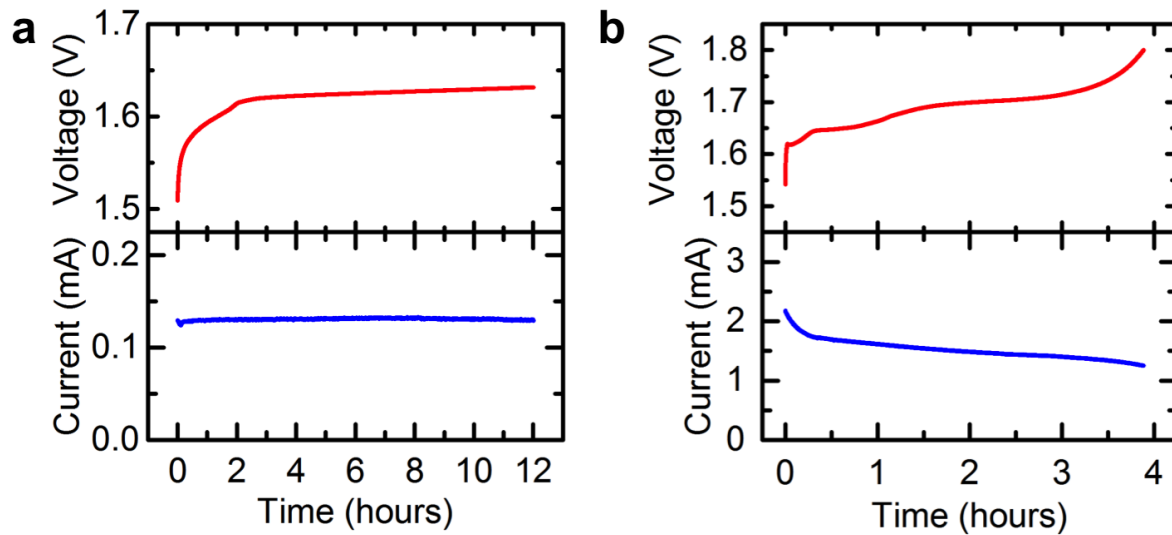


Figure 4.8: Voltage and current during battery charging. The OPV module is exposed to either CFL lighting with illuminance of 3000 lux (a) or sunlight (b).

the charge under sunlight, 4 hours, with an average current of 1.4 mA, is consistent with the measured capacity of the battery operated at this rate.

4.4.1 Energy conversion and storage efficiency

After each charging period, the battery was discharged at a current of 4 mA, and the energy transferred in each step of the energy conversion and storage process was calculated in order to determine the energy conversion and storage efficiency (ECSE), a figure of merit commonly used in solar supercapacitor charging systems [43]. The total energy incident on the OPV module was 160 J for the 12-hour charging period under the CFL (Figure 4.8a), and 2870 J for the 4-hour charging period in sunlight (Figure 4.8b). The resulting energy output of the module, delivered to the battery, was determined by integrating the power output over the duration of the charging period and found to be 9.16 J and 36.0 J for the CFL and sunlight conditions. The average OPV module efficiency over the charging period was therefore 5.7% and 1.3%, respectively. The deviation between these efficiency values and the PCE in Table 1 is due in part to the fact that the OPV module was not operating at its maximum power point during the charging period; instead, its voltage was set by the battery voltage. The efficiency under the 3000 lux CFL is in very good agreement with the power output at the battery voltage given in Figure 4.6b. Additionally, the values in Table 1 are averages of several modules, and there was substantial variation in performance from one module to the next under sunlight due in large part to variation in series resistance. The particular module used to charge the battery in Figure 4.8b was at the low end of the performance range, with maximum 1-sun PCE of 1.6% and current-voltage characteristics given in Figure

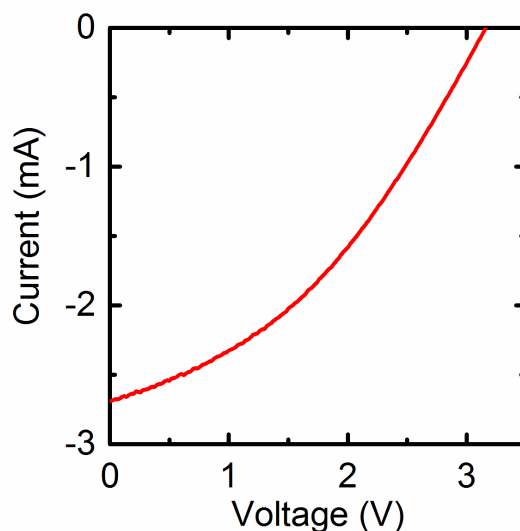


Figure 4.9: Current-voltage characteristic of the particular OPV module used to charge the wire battery under sunlight.

4.9. If an OPV module at the high end of the performance range had been used instead, the battery could be expected to charge nearly 40% faster. Thus, the variability of modules has a significant impact on the charging process. However, the improvement in efficiency for CFL illumination relative to sunlight is even greater than the variation in performance between individual modules.

When the battery was discharged at 4 mA following the CFL and sunlight charging periods, the energy extracted from the battery was 4.24 and 29.0 J, respectively, giving battery charge/discharge efficiencies of 46.3% and 80.6%. While the battery tended to exhibit a high coulombic efficiency (>96%), the battery efficiency defined in terms of energy is lower because it includes the losses due to the potential difference of $\sim 0.2\text{V}$ between charging and discharging, seen in Figure 4.1 [1]. In addition, lower efficiencies are obtained if the battery is not operated at an optimum ratio of charge rate to discharge rate. Charge-discharge profile plays an important role in the efficiency of silver-zinc batteries due to changes in the morphology of the silver electrode with each electrochemical cycle. Slow charging rates, such as the $\sim C/40$ rate of charging with the OPV module under CFL lighting, have been shown to result in formation of larger size silver oxide particles [35]. This leads to less efficient material access during the subsequent discharge due to ionic transport limitations. The sunlight conditions provided a higher charging rate ($\sim C/4$) and, thus, formation of smaller size silver oxide particles, which could be more readily reduced in the subsequent discharge. Therefore, the obtained battery efficiency results are in good agreement with previous reports on the cycling of similar silver-zinc batteries [35].

Finally, the ECSE was calculated as the ratio of the energy extracted from the battery during discharging to the energy incident on the OPV module during charging. The OPV

module efficiency and battery efficiency exhibited opposing trends with respect to light intensity: the OPV module efficiency was 4.4 times lower under sunlight than under the CFL, while the battery efficiency was 1.7 times higher. The ECSE, which is the product of these two efficiencies, was therefore 2.7 times higher under the CFL, 2.7% vs. 1.0%. Since the OPV module was the limiting factor in the 1-sun ECSE, improving the OPV module performance under sunlight should be the most effective way of improving the 1-sun ECSE. This could be accomplished by designing the module geometry to minimize series resistance, for example by using cells with a smaller aspect ratio such as those presented in Figure 4.5, as well as employing a more conductive transparent electrode. The low-light ECSE could be improved by using a smaller battery, so that the same OPV module current would equate to a larger charging rate and result in a more optimal silver electrode morphology. However, reducing the battery capacity would limit the amount of solar energy that can be stored and the type and duration of loads that can be powered. Instead, optimizing the battery design for high efficiency at low charging rates could enable high low-light performance without sacrificing energy storage capacity.

4.4.2 Charging under full-day lighting profiles

To assess the potential of these approaches to improve overall energy conversion and storage performance, it is necessary to consider typical lighting conditions the OPV module is likely to experience when integrated into a wearable system. For example, a case is considered in which the wearer walks to work in the sunlight, works under office lighting, takes a break to eat lunch outdoors, and then walks home after a few more hours in the office. To determine the relative contributions of indoor and outdoor light harvesting to the battery charge, the OPV modules were exposed to conditions simulating this day: 30 minutes of sunlight, 4 hours of indoor light, 1 hour of sunlight, 4 hours of indoor light, and 30 minutes of sunlight. The voltage and current into the battery were monitored throughout the day, using either 300 lux or 3000 lux CFL illumination for the indoor lighting condition, as shown in Figures 4.10a and 4.10b, respectively. Figures 4.10a and 4.10b also show the cumulative stored charge in the battery, equal to the integral of the current. While there was some variation in current during the sunlight phases, due to variation between modules and the changing battery voltage during charging, the currents during the indoor light phases were very stable and can be used to determine the effect of the indoor light intensity.

When the indoor illuminance was 300 lux, the amount of energy harvested was dominated by the amount of time spent in the sun. In the example day shown in Figure 4.10a, only 2.8% of the charge stored in the battery resulted from the indoor light harvesting. When the indoor illuminance was increased to 3000 lux, however, the charge collected during the indoor portions of the day increased correspondingly by a factor of 10, contributing 27% of the total charge. The slopes of the stored charge curves in Figures 4.10a and 4.10b can be used to visualize the charge contributions during the different lighting phases, clearly indicating that the 3000 lux condition contributed a significant fraction of the total charge while the 300 lux condition did not. Thus, if the system is expected to experience a lighting profile like

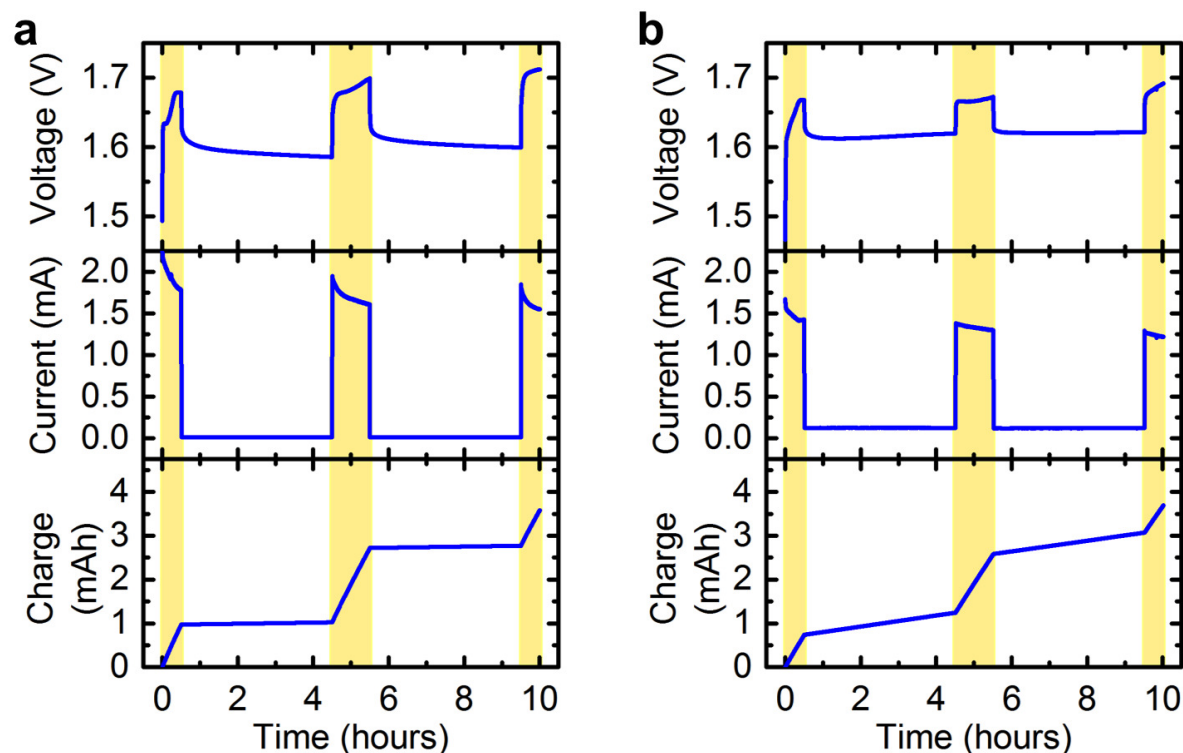


Figure 4.10: Voltage, current, and cumulative stored charge of solar battery charging during a simulated day of use. Yellow shaded areas indicate periods of exposure to sunlight. White areas correspond to CFL lighting with illuminance of 300 lux (a) or 3000 lux (b).

that in Figure 4.10a on most days, having a high 1-sun ECSE is far more important than having a high low-light ECSE, because the charge collected during the indoor phases is nearly negligible compared to that of the sunlight phases. On the other hand, if the system will frequently be exposed to higher indoor illuminance, such as in Figure 4.10b, the system should ideally have a high ECSE under both sunlight and indoor light because both sunlight and indoor phases would contribute significantly to the total charge. Since the battery was almost fully charged at the end of each day, reducing the battery capacity to improve the low-light ECSE is not desirable, and improving the battery efficiency under very low charge rate would be preferred.

4.5 Conclusion

In summary, organic photovoltaic modules were integrated with silver-zinc wire batteries for applications in wearable accessories such as an energy harvesting and storage bracelet. Photovoltaic performance was characterized with various numbers of cells in the module and various indoor and outdoor lighting conditions. Battery charging was demonstrated from the

photovoltaic module under multiple lighting conditions, including time-varying illumination representing the conditions a wearable device may be exposed to during its wearer's daily routine. While the energy harvested under typical indoor light was very small compared to that of sunlight, placing the device in closer proximity to an indoor light source greatly increased the charging rate, collecting an amount of energy that was significant compared to sunlight. By comparing the factors limiting energy conversion and storage efficiency under sunlight and indoor light, as well as the contribution of each lighting condition to the total energy stored in the battery, promising paths forward have been identified to improve system performance. The energy conversion and storage efficiency of the system was found to be limited by the OPV module under high light intensity and limited by the battery under low light intensity. Therefore, minimizing series resistance of the OPV module is most important to improve system performance under sunlight, while designing the battery structure for high efficiency at low charging rates is most important to improve low-light performance. For applications where both sunlight and indoor light are expected to contribute significantly to the stored energy, both of these improvements are necessary. Overall, this energy harvesting and storage system is able to collect and provide power ranging from microwatts to milliwatts, depending on the illumination, a relevant range for many electronic devices of interest for wearable systems.

4.6 References

1. Zamarayeva, A. M., Ostfeld, A. E., Wang, M., Duey, J. K., Deckman, I., Lechène, B. P., Davies, G., Steingart, D. A. & Arias, A. C. Flexible and stretchable power sources for wearable electronics. *Submitted* (2016).
2. Khan, Y., Ostfeld, A. E., Lochner, C. M., Pierre, A. & Arias, A. C. Monitoring of vital signs with flexible and wearable medical devices. *Advanced Materials* **28**, 4373–4395 (2016).
3. Yang, Y., Lin, Z.-H., Hou, T., Zhang, F. & Wang, Z. L. Nanowire-composite based flexible thermoelectric nanogenerators and self-powered temperature sensors. *Nano Research* **5**, 888–895 (2012).
4. Chiu, Y.-Y., Lin, W.-Y., Wang, H.-Y., Huang, S.-B. & Wu, M.-H. Development of a piezoelectric polyvinylidene fluoride (PVDF) polymer-based sensor patch for simultaneous heartbeat and respiration monitoring. *Sensors and Actuators A: Physical* **189**, 328–334 (2013).
5. Wu, N., Cheng, X., Zhong, Q., Zhong, J., Li, W., Wang, B., Hu, B. & Zhou, J. Cellular polypropylene piezoelectret for human body energy harvesting and health monitoring. *Advanced Functional Materials* **25**, 4788–4794 (2015).

6. Yang, P.-K., Lin, L., Yi, F., Li, X., Pradel, K. C., Zi, Y., Wu, C.-I., He, J.-H., Zhang, Y. & Wang, Z. L. A flexible, stretchable and shape-adaptive approach for versatile energy conversion and self-powered biomedical monitoring. *Advanced Materials* **27**, 3817–3824 (2015).
7. Yi, F., Lin, L., Niu, S., Yang, P. K., Wang, Z., Chen, J., Zhou, Y., Zi, Y., Wang, J., Liao, Q., Zhang, Y. & Wang, Z. L. Stretchable-rubber-based triboelectric nanogenerator and its application as self-powered body motion sensors. *Advanced Functional Materials* **25**, 3688–3696 (2015).
8. Wüsten, J. & Potje-Kamloth, K. Organic thermogenerators for energy autarkic systems on flexible substrates. *Journal of Physics D: Applied Physics* **41**, 135113 (2008).
9. Kim, S., Vyas, R., Bito, J., Niotaki, K., Collado, A., Georgiadis, A. & Tentzeris, M. M. Ambient RF energy-harvesting technologies for self-sustainable standalone wireless sensor platforms. *Proceedings of the IEEE* **102**, 1649–1666 (2014).
10. Roselli, L., Borges Carvalho, N., Alimenti, F., Mezzanotte, P., Orecchini, G., Virili, M., Mariotti, C., Goncalves, R. & Pinho, P. Smart surfaces: Large area electronics systems for internet of things enabled by energy harvesting. *Proceedings of the IEEE* **102**, 1723–1746 (2014).
11. Krebs, F. C., Biancardo, M., Winther-Jensen, B., Spanggard, H. & Alstrup, J. Strategies for incorporation of polymer photovoltaics into garments and textiles. *Solar Energy Materials and Solar Cells* **90**, 1058–1067 (2006).
12. Kaltenbrunner, M., White, M. S., Glowacki, E. D., Sekitani, T., Someya, T., Sariciftci, N. S. & Bauer, S. Ultrathin and lightweight organic solar cells with high flexibility. *Nature Communications* **3**, 770 (2012).
13. Kim, B. J., Kim, D. H., Lee, Y.-Y., Shin, H.-W., Han, G. S., Hong, J. S., Mahmood, K., Ahn, T. K., Joo, Y.-C., Hong, K. S., Park, N.-G., Lee, S. & Jung, H. S. Highly efficient and bending durable perovskite solar cells: Toward a wearable power source. *Energy & Environmental Science* **8**, 916–921 (2015).
14. O'Connor, T. F., Zaretski, A. V., Savagatrup, S., Printz, A. D., Wilkes, C. D., Diaz, M. I., Sawyer, E. J. & Lipomi, D. J. Wearable organic solar cells with high cyclic bending stability: Materials selection criteria. *Solar Energy Materials and Solar Cells* **144**, 438–444 (2016).
15. O'Connor, B., Pipe, K. P. & Shtein, M. Fiber based organic photovoltaic devices. *Applied Physics Letters* **92**, 193306 (2008).
16. Hou, S., Lv, Z., Wu, H., Cai, X., Chu, Z. & Zou, D. Flexible conductive threads for wearable dye-sensitized solar cells. *Journal of Materials Chemistry* **22**, 6549 (2012).
17. Pan, S., Yang, Z., Chen, P., Deng, J., Li, H. & Peng, H. Wearable solar cells by stacking textile electrodes. *Angewandte Chemie* **126**, 6224–6228 (2014).

18. Qiu, L., Deng, J., Lu, X., Yang, Z. & Peng, H. Integrating perovskite solar cells into a flexible fiber. *Angewandte Chemie (International ed. in English)* **53**, 10425–10428 (2014).
19. Yang, Z., Deng, J., Sun, X., Li, H. & Peng, H. Stretchable, wearable dye-sensitized solar cells. *Advanced Materials* **26**, 2643–7, 2613 (2014).
20. Li, R., Xiang, X., Tong, X., Zou, J. & Li, Q. Wearable double-twisted fibrous perovskite solar cell. *Advanced Materials* **27**, 3831–3835 (2015).
21. Yun, M. J., Cha, S. I., Seo, S. H., Kim, H. S. & Lee, D. Y. Insertion of dye-sensitized solar cells in textiles using a conventional weaving process. *Scientific Reports* **5**, 11022 (2015).
22. Zhang, N., Chen, J., Huang, Y., Guo, W., Yang, J., Du, J., Fan, X. & Tao, C. A wearable all-solid photovoltaic textile. *Advanced Materials* **28**, 263–269 (2016).
23. Burke, D. J. & Lipomi, D. J. Green chemistry for organic solar cells. *Energy & Environmental Science* **6**, 2053 (2013).
24. Krebs, F. C. & Jørgensen, M. Polymer and organic solar cells viewed as thin film technologies: What it will take for them to become a success outside academia. *Solar Energy Materials and Solar Cells* **119**, 73–76 (2013).
25. Lizin, S., Van Passel, S., De Schepper, E., Maes, W., Lutsen, L., Manca, J. & Vandezande, D. Life cycle analyses of organic photovoltaics: A review. *Energy & Environmental Science* **6**, 3136–3149 (2013).
26. Lungenschmied, C., Dennler, G., Neugebauer, H., Sariciftci, S. N., Glatthaar, M., Meyer, T. & Meyer, A. Flexible, long-lived, large-area, organic solar cells. *Solar Energy Materials and Solar Cells* **91**, 379–384 (2007).
27. Forberich, K., Guo, F., Bronnbauer, C. & Brabec, C. J. Efficiency limits and color of semitransparent organic solar cells for application in building-integrated photovoltaics. *Energy Technology* **3**, 1051–1058 (2015).
28. Li, L., Wu, Z., Yuan, S. & Zhang, X.-B. Advances and challenges for flexible energy storage and conversion devices and systems. *Energy & Environmental Science* **7**, 2101–2122 (2014).
29. Wang, X., Lu, X., Liu, B., Chen, D., Tong, Y. & Shen, G. Flexible energy-storage devices: Design consideration and recent progress. *Advanced Materials* **26**, 4763–4782 (2014).
30. Zhou, G., Li, F. & Cheng, H.-M. Progress in flexible lithium batteries and future prospects. *Energy & Environmental Science* **7**, 1307–1338 (2014).
31. Vlad, A., Singh, N., Galande, C. & Ajayan, P. M. Design considerations for unconventional electrochemical energy storage architectures. *Advanced Energy Materials* **5**, 1402115 (2015).

32. Dennler, G., Bereznev, S., Fichou, D., Holl, K., Ilic, D., Koeppel, R., Krebs, M., Labouret, A., Lungenschmied, C., Marchenko, A., Meissner, D., Mellikov, E., Méot, J., Meyer, A., Meyer, T., Neugebauer, H., Öpik, A., Sariciftci, N., Taillemaite, S. & Wöhrle, T. A self-rechargeable and flexible polymer solar battery. *Solar Energy* **81**, 947–957 (2007).
33. Lee, Y.-H., Kim, J.-S., Noh, J., Lee, I., Kim, H. J., Choi, S., Seo, J., Jeon, S., Kim, T.-S., Lee, J.-Y. & Choi, J. W. Wearable textile battery rechargeable by solar energy. *Nano Letters* **13**, 5753–5761 (2013).
34. Kim, J.-S., Ko, D., Yoo, D.-J., Jung, D. S., Yavuz, C. T., Kim, N.-I., Choi, I.-S., Song, J. Y. & Choi, J. W. A half millimeter thick coplanar flexible battery with wireless recharging capability. *Nano Letters* **15**, 2350–2357 (2015).
35. Zamarayeva, A. M., Gaikwad, A. M., Deckman, I., Wang, M., Khau, B., Steingart, D. A. & Arias, A. C. Fabrication of a high-performance flexible silver-zinc wire battery. *Advanced Electronic Materials* **2**, 1500296 (2016).
36. Berchmans, S., Bandodkar, A. J., Jia, W., Ramírez, J., Meng, Y. S. & Wang, J. An epidermal alkaline rechargeable Ag-Zn printable tattoo battery for wearable electronics. *Journal of Materials Chemistry A* **2**, 15788–15795 (2014).
37. Karpinski, A., Makovetski, B., Russell, S., Serenyi, J. & Williams, D. Silver-zinc: Status of technology and applications. *Journal of Power Sources* **80**, 53–60 (1999).
38. Gaikwad, A. M., Arias, A. C. & Steingart, D. A. Recent progress on printed flexible batteries: Mechanical challenges, printing technologies, and future prospects. *Energy Technology* **3**, 305–328 (2015).
39. MacKenzie, J. D. & Ho, C. Perspectives on energy storage for flexible electronic systems. *Proceedings of the IEEE* **103**, 535–553 (2015).
40. Lechêne, B. P., Cowell, M., Pierre, A., Evans, J., Wright, P. K. & Arias, A. C. Organic solar cells and fully printed supercapacitors for indoor light energy harvesting. *Nano Energy* **26**, 631–640 (2016).
41. Misra, V., Bozkurt, A., Calhoun, B., Jackson, T., Jur, J., Lach, J., Lee, B., Muth, J., Oralkan, O., Ozturk, M., Trolrier-McKinstry, S., Vashaee, D., Wentzloff, D. & Zhu, Y. Flexible technologies for self-powered wearable health and environmental sensing. *Proceedings of the IEEE* **103**, 665–681 (2015).
42. Van Bavel, M., Leonov, V., Yazicioglu, R. F., Torfs, T., Van Hoof, C., Posthuma, N. E. & Vullers, R. J. Wearable battery-free wireless 2-channel EEG systems powered by energy scavengers. *Sensors & Transducers Journal* **94**, 103–115 (2008).
43. Schmidt, D., Hager, M. D. & Schubert, U. S. Photo-rechargeable electric energy storage systems. *Advanced Energy Materials* **6**, 1500369 (2016).

Chapter 5

Flexible Thin-Film Energy Harvesting and Storage Systems

In this chapter, flexible energy harvesting and storage systems are created by pairing thin-film lithium-ion batteries with thin-film amorphous silicon or organic photovoltaic modules. Battery charging under sunlight and indoor light, with and without battery management circuitry, is demonstrated. It is shown how, by selecting the appropriate load duty cycle, the average load current can be matched to the solar module current and the battery can be maintained at a constant state of charge. It is also shown how matching the solar module voltage to the battery voltage enables high system efficiency to be achieved without maximum power point tracking. Portions of the work presented in this chapter are published in [1].

5.1 Introduction

The previous chapter presented a wearable energy harvesting and storage system designed in the form of a bracelet, comprising a rigid photovoltaic (PV) module and a flexible wire battery wristband. The constraints imposed by the aesthetics and form factor limit the components of such an accessory to relatively small sizes, resulting in solar module output of a few mW in full sunlight and battery capacity of a few mWh. While this size of system is adequate for powering small loads such as low-power wearable sensors [2–4], loads with higher-power components or higher duty cycles may require a larger source. Wireless communication and light-emitting devices, in particular, require relatively large current pulses on the order of many milliamps. For example, the reported peak current consumption of Bluetooth Low Energy wireless communication in a wearable sensor module was 18 mA [3], and a smart watch such as the Samsung Gear 2 consumes up to 48 mA during calls [5].

This chapter reports on flexible thin-film energy harvesting and storage systems that can meet these higher power demands. The flexible thin-film architecture is highly versatile and can be scaled to various areas to provide the desired solar module current or battery capacity for the application of interest. To date, numerous flexible thin-film rechargeable batteries and

energy harvesting technologies have been reported [6–19]. These devices cover a wide range of sizes and applications, from wearable patches that harvest energy from body temperature or motion [14–16] to large-area rollable modules of flexible solar cells [19] or batteries [10] for portable off-grid power. However, an effective energy harvesting and storage system requires not only high-performing individual devices, but also good compatibility between system components. When designing such a system, it is necessary to consider both average and peak power consumption of the load, and then select the type and dimensions of the battery and energy harvester in order to power the load efficiently for the desired length of time.

PV module selection criteria for battery charging applications have been discussed in Chapters 1 and 4, but are reiterated here as selecting an appropriate PV module is crucial for the design of the thin-film system as well. The selection of an appropriate PV module for a particular battery and application depends on the expected illumination conditions, as irradiance can vary by a factor of 100 or more from typical indoor lighting to sunny outdoor conditions [20]. The short-circuit current of a PV module is roughly proportional to the irradiance of the incident light, while the open-circuit voltage is only logarithmically dependent on the irradiance [21]. Ideally, the PV module should be able to provide power over the entire range of battery voltages and expected illumination conditions; in other words, the open-circuit voltage of the PV module should be at least equal to the maximum battery voltage. For most efficient utilization of the PV module, the maximum power point voltage of the PV module should be within the voltage range of the battery. A large-area PV module is desirable to provide a high charging current under low irradiance conditions. However, if the area of the module is too large, the charging current under high irradiance may induce a high potential drop in the battery and the battery would reach its upper voltage limit before becoming fully charged.

To date there have been several demonstrations of flexible thin-film PV modules charging both commercial [22, 23] and custom [24–26] flexible batteries, but the performance often suffers from limited battery lifetime [24, 25] or low battery capacity at high charging rates [25, 26]. Therefore, to achieve a high-performing system, it is critical to include a battery that has high capacity and high charge/discharge rate capability in addition to mechanical flexibility. Here, a flexible lithium-ion battery with exceptionally high capacity and rate capability is employed [1]. Solar battery charging is demonstrated using a commercial off-the-shelf amorphous silicon flexible solar module under multiple lighting conditions, as well as using a printed organic solar module. The battery and solar module are integrated into a hybrid energy system that also incorporates a blocking diode and battery management circuit, components which are necessary to maintain the efficiency, safety, and longevity of the system. Finally, load duty cycle optimization is shown to greatly extend the battery lifetime under indoor lighting conditions.

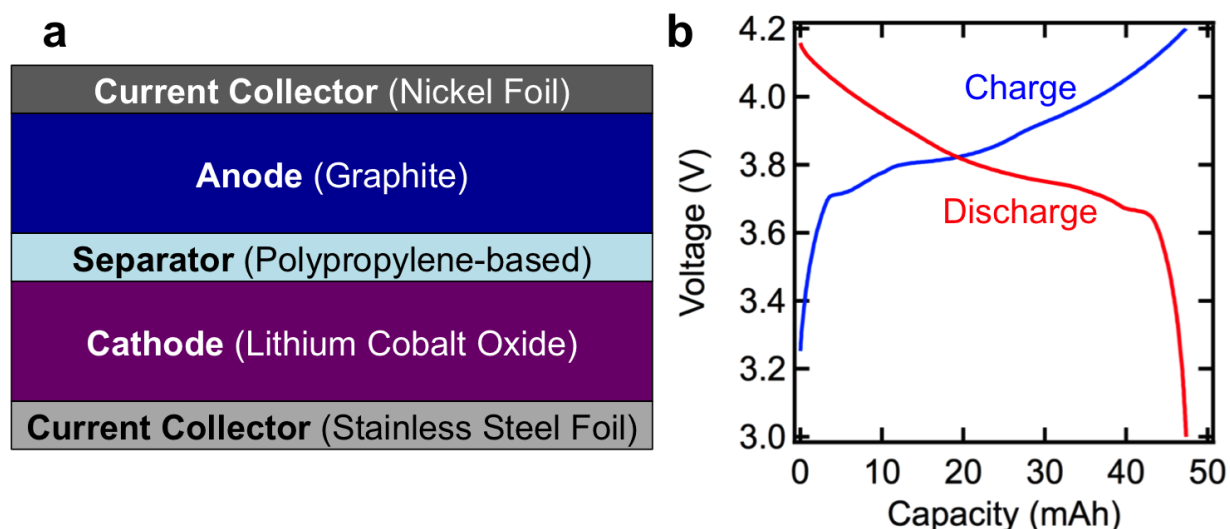


Figure 5.1: (a) Schematic illustration of printed flexible thin-film lithium-ion battery. (b) Charge-discharge curve of a 48 mAh battery cycled between 4.2 and 3.0 V at C/5 rate [1]. Data collected by Dr. Abhinav Gaikwad.

5.2 Flexible thin-film batteries

Since the same battery structure is used in all of the systems discussed in this chapter, an overview of the battery characteristics is provided here. Flexible thin-film lithium-ion batteries were designed and fabricated by Dr. Abhinav Gaikwad with the structure shown in Figure 5.1a, using the processes described in [1]. The batteries used a common architecture combining a blade-coated graphite anode and a blade-coated lithium cobalt oxide cathode, and utilized thin, highly conductive, and mechanically robust flexible foils as the current collectors. Due to optimization of the thicknesses and composition of the layers, these batteries had energy density of 6.98 mWh/cm^2 , considerably higher than that of other flexible lithium-ion batteries in the literature [26–32]. They displayed over 90% capacity retention at high discharge rates up to 3C (corresponding to a full discharge in 20 minutes). For a 50 mAh battery, for example, this translates to a discharge current of 150 mA. The battery was also highly flexible and rechargeable, demonstrating excellent capacity retention of $\sim 99\%$ after 100 charge/discharge cycles at C/5 rate (i.e., full charge or discharge in 5 hours) and 600 cycles of mechanical flexing [1]. A representative charge-discharge characteristic of this battery structure is shown in Figure 5.1b, for a 2×2 inch battery with capacity of 48 mAh cycled at C/5 rate [1]. The capacity scales proportionally with the area of the battery, so the battery dimensions can be designed to provide whatever capacity is needed by the application.

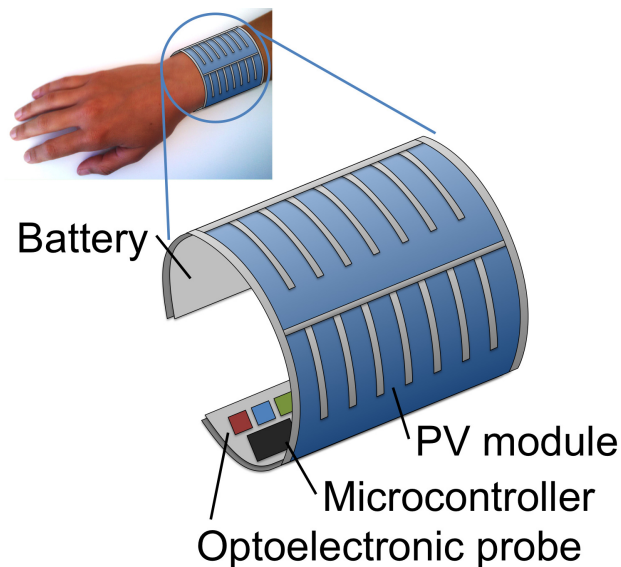


Figure 5.2: Illustration of activity-tracking wristband concept containing flexible battery, PV energy harvesting module, and pulse oximeter components.

5.3 System design for pulse oximeter application

In this section, the pulse oximeter is considered as an example wearable electronic load and a flexible energy harvesting and storage system is designed to meet its power requirements. The pulse oximeter monitors a patient's heart rate and blood oxygenation by measuring the light absorbed in the blood at two different wavelengths. Due to the high power consumption of the optoelectronic probe, the pulse oximeter requires a high current of 20 mA during each measurement, compared to 1 mA between measurements. The lifetime of the battery between charging events will depend on the oximeter's duty cycle—the fraction of the time that it is measuring—in addition to the battery capacity and the power available from energy harvesting. Thus, the design of a reliable power supply for this application requires a battery with high capacity and rate capability, as well as an energy harvester with relatively high power density (such as PV) and appropriate voltage to charge the battery. A solar powered pulse oximeter has recently been demonstrated using rigid components [33], but since the optoelectronic probe must be in close contact with the skin, making the components including the power supply flexible could greatly improve user comfort. Flexibility also improves signal integrity, since wrapping the device around a patient's finger reduces the parasitic current due to ambient light [34]. Ideally, the pulse oximeter system would be constructed as a single flexible piece as shown in Figure 5.2, comprising the optoelectronic probe, data processing electronics, and a flexible power source consisting of layered battery and PV module.

A 2×2 inch (48 mAh) flexible thin-film lithium-ion battery was integrated with a flexible thin-film amorphous silicon photovoltaic module to form the energy harvesting and storage system for this application. The system is shown schematically in Figure 5.3a and a pho-

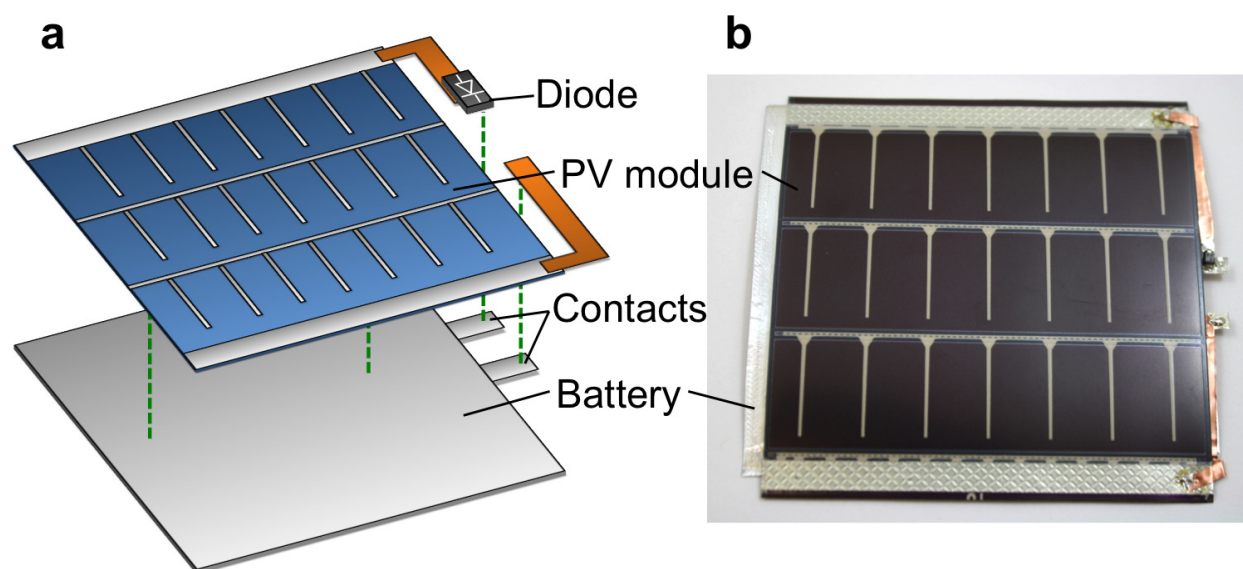


Figure 5.3: (a) Diagram and (b) photograph of a flexible energy harvesting and storage system comprising PV module, battery, and surface-mount Schottky diode, showing the components and attachment points.

tograph is given in Figure 5.3b. Since both PV module and battery are flexible, the entire system can also be flexed and attached to flexible or curved surfaces, as shown in Figure 5.4. The behavior of the energy system was characterized under multiple lighting conditions and load duty cycles, and its ability to power the pulse oximeter was verified. The results presented in this section are published in [1].

5.3.1 Experimental details

Fabrication and characterization of the flexible lithium-ion battery was performed by Dr. Abhinav Gaikwad as described in [1]. Flexible amorphous silicon photovoltaic modules (Powerfilm MPT3.6-75) were used for energy harvesting. The PV module current-voltage characteristics and battery charging characteristics were obtained using a Keithley 2400 source-meter under conditions representing both indoor and outdoor illumination. The “outdoor” condition, air mass (AM) 1.5 global illumination with irradiance of 100 mW/cm^2 , was simulated with an Oriel Sol1A solar simulator. Two indoor conditions were compared, using a 13W compact fluorescent light (CFL) bulb at two different distances from the PV module, 5 cm and 16 cm. Irradiance was approximately 4.8 and 0.9 mW/cm^2 respectively for the two distances, as measured using a photodiode (Hamamatsu 66R) and spectrometer (Thorlabs CCS 200). A flexible power supply integrating a PV module, battery and blocking diode (Schottky diode, ON Semiconductor MBRM130LT3G) was also constructed, as shown in Figures 5.3 and 5.4. The electrical connections were made using a combination of copper

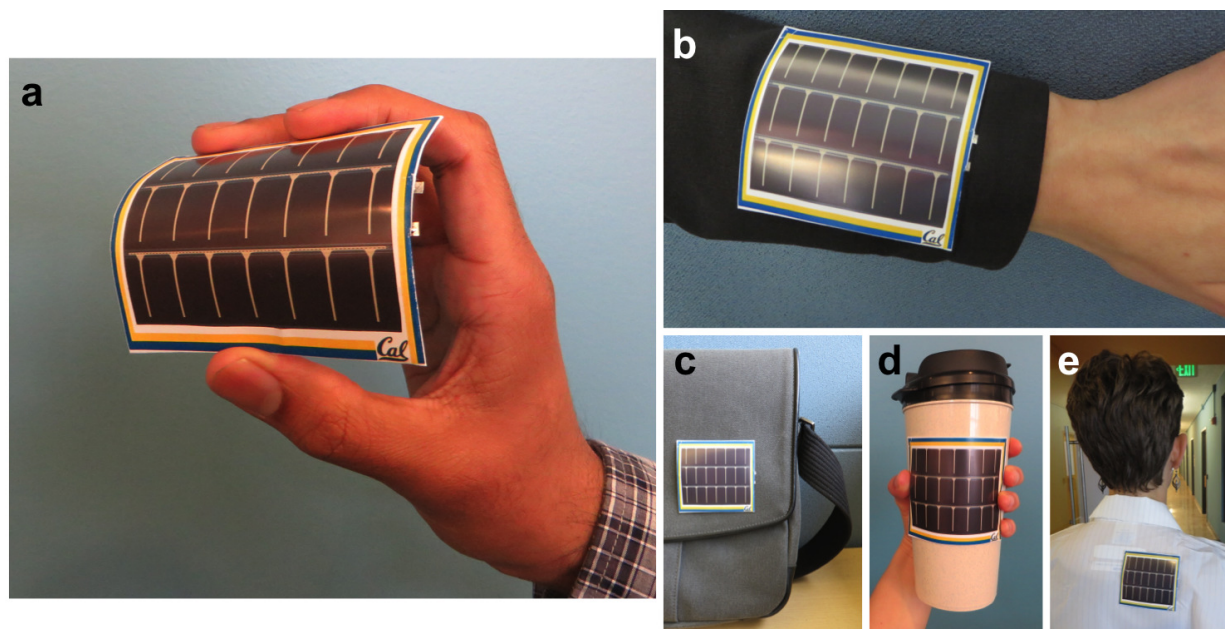


Figure 5.4: Photographs of the flexible energy harvesting and storage system being flexed in the hand (a) and on various flexible and curved surfaces: jacket sleeve (b), bag (c), travel mug (d), and lab coat (e).

foil, conductive epoxy, and soldering.

To characterize the behavior of the battery with both solar module and load connected simultaneously, the Keithley source-meter was configured to repeatedly draw 20 mA for a specified time, followed by 1 mA for a specified time, simulating the power consumption of the pulse oximeter during its “on” and “off” states. The PV module was exposed to either 4.8 or 0.9 mW/cm² of light using the CFL as before. The source-meter monitored the load current and voltage throughout the process.

5.3.2 Solar module characteristics and battery charging

To create an energy storage and harvesting system, the flexible lithium-ion battery was combined with a flexible amorphous silicon PV module having similar dimensions and compatible voltage. The current-voltage characteristics of the PV module are shown in Figure 5.5a under three lighting conditions: a CFL at two different heights to produce irradiance of 0.9 and 4.8 mW/cm², and simulated solar illumination of 100 mW/cm². As expected, the current of the PV module was strongly dependent on the irradiance, while the voltage was only slightly affected; the maximum power point voltage was in the 3-4 V range for all three illumination conditions. The battery was charged from 3.6 V to 4.1 V by the PV module under each illumination condition, as shown in Figure 5.5b. As expected, the time for the battery to charge was inversely proportional to the average PV module current. When the

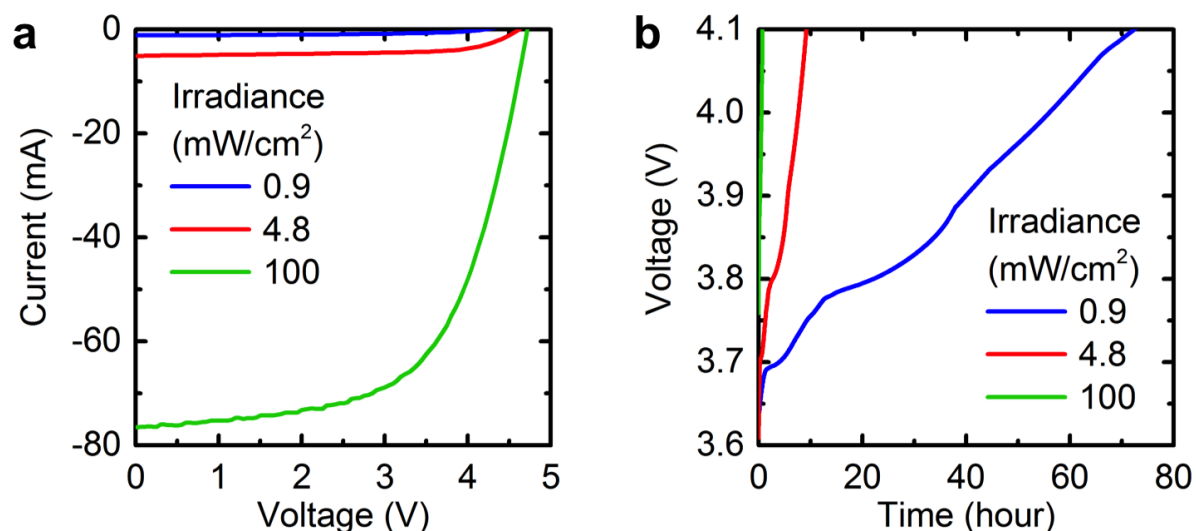


Figure 5.5: (a) Current-voltage characteristics of the flexible amorphous silicon PV module under three different illumination conditions. (b) Battery voltage over time as it is charged by the PV module, under the same three illumination conditions.

irradiance was increased from 0.9 to 4.8 mW/cm², the average PV module current over the 3.6-4.1 V range increased from 0.46 mA to 3.9 mA, a factor of about 8. The time for the battery to charge correspondingly decreased by a factor of 8, from 72 hours to 9.2 hours. Under 100 mW/cm², the higher PV module current introduced a noticeable potential drop in the battery, increasing the voltage at the start of charging to 3.75 V. The average PV current over this charging voltage range was 51 mA, 12 times higher than the current in the 4.8 mW/cm² condition, and the battery charge time was correspondingly 12 times lower, 0.77 hours. This range of light intensities corresponds to charging rates varying from C/72 to greater than 1C. Under all of the illumination conditions, the charge supplied to the battery over the 3.6-4.1 V range was calculated to be approximately 40 mAh, which is consistent with the battery capacity measured over that voltage range during galvanostatic charging.

While these results were obtained by connecting the PV module directly to the battery, the system was also characterized with the addition of a blocking diode connected in series between the PV module and battery as shown in Figure 5.3a. The blocking diode is meant to prevent discharge of the battery into the solar module in the absence of light, without significantly impacting the energy collection efficiency under illumination. Figure 5.6a shows current-voltage characteristics with the blocking diode, indicating the effectiveness of the diode at allowing forward current from the PV module while blocking reverse current. A charging curve for the system with the blocking diode under 4.8 mW/cm² illumination is shown in Figure 5.6b. The light was turned off for several hours in the middle of charging, indicated by the shaded region. Even though the components remained connected during that time, no significant loss of charge was observed, due to the presence of the diode. The

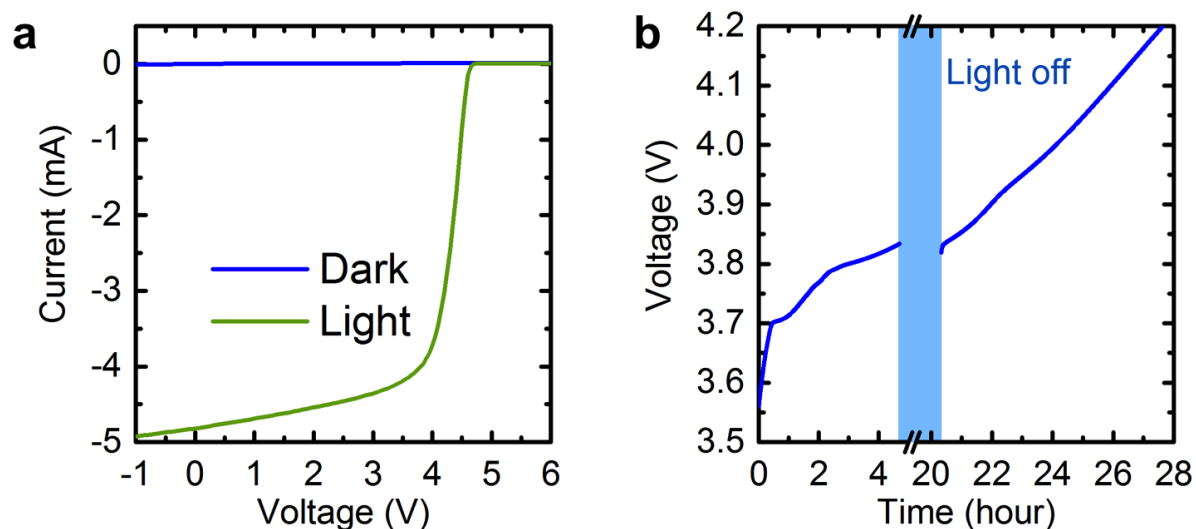


Figure 5.6: Behavior of PV module and battery with blocking diode. (a) Current-voltage characteristics of PV module with blocking diode in the dark and under 4.8 mW/cm^2 illumination from a CFL. (b) Battery charging characteristics under the same illumination condition. In the shaded region, the light was turned off but the battery, PV module, and diode remained connected together. The blocking diode prevented current from flowing out of the battery into the PV module.

total illumination time required for the battery to reach 4.1 V under these conditions was 10.3 hours. This is slightly longer than the time of 9.2 hours without a blocking diode reported in Figure 5.5b, due primarily to the power dissipation in the diode during charging.

The battery was shown previously to have excellent lifetime when cycled at C/5 rate [1]. However, the battery would be subjected to a much higher charging rate under sunlight and higher peak discharging rates when powering electronic devices such as the pulse oximeter. Therefore, the stability of the battery was assessed as it was repeatedly charged to 4.2 V using the PV module under full sun (100 mW/cm^2) and discharged to 3.6 V at a rate of 20 mA. The battery voltage profile during each charge and discharge cycle is plotted in Figure 5.7a, for 10 cycles. Figure 5.7b plots the time required for the battery to reach 4.2 V while charging and 3.6 V while discharging, showing that the performance of the battery was relatively stable over the 10 cycles. The variation in the charging and discharging time may be attributed to variation in temperature of the battery and PV module, and the resulting variation in PV module voltage and battery potential drop.

5.3.3 Battery and solar module powering loads

The battery was employed to power a pulse oximeter, consisting of optoelectronic probe, light-emitting diode (LED) driver, photodiode read circuit, and microcontroller [1]. For

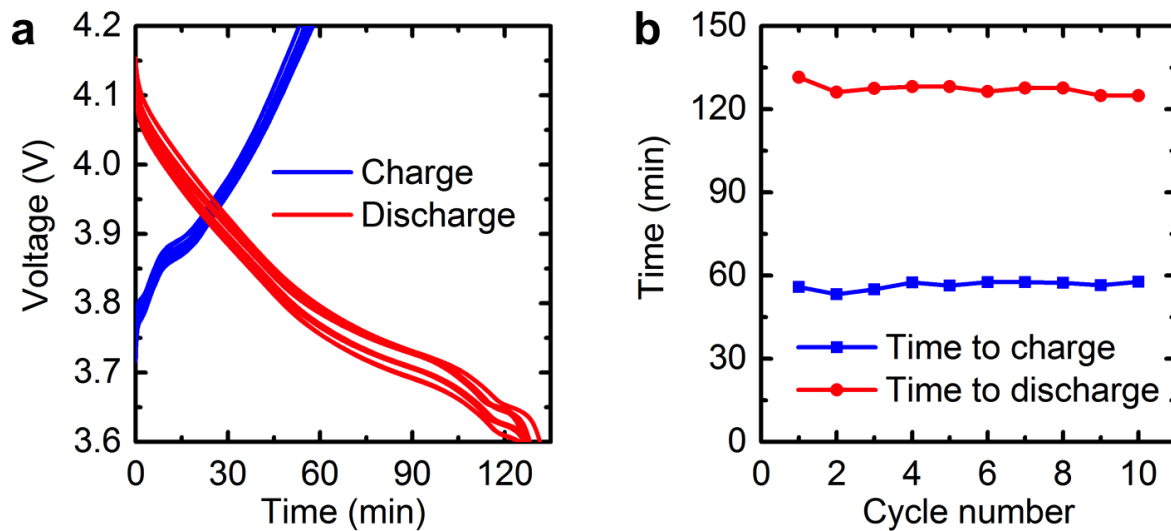


Figure 5.7: (a) Battery voltage profiles over 10 charge/discharge cycles. Charging is performed using the PV module under 100 mW/cm^2 irradiance and discharging is performed at a constant current of 20 mA. (b) Time for the battery to charge to 4.2 V and discharge to 3.6 V over the same 10 cycles as in (a).

the purposes of activity tracking, the pulse oximeter turns on periodically to collect pulse and blood oxygenation measurements. During operation, the optoelectronic probe consumes around 16 mA of current and the data acquisition and processing units consume around 4 mA. In the “off” state, the oximeter system turns off the optoelectronic probe and the data acquisition module; however, the microcontroller and the serial communication module stay on, consuming around 1 mA of current. The lifetime of a battery powering the oximeter depends on the duty cycle, the fraction of the time the oximeter is in the “on” state; an appropriate power source should be able to power the oximeter for many hours before charging is required. An electronic load was configured to alternate between 20 mA and 1 mA with variable duty cycle, simulating the pulse oximeter alternating between its “on” and “off” states, in order to characterize the lifetime of the energy storage and harvesting system under different illumination conditions.

When a battery is connected to a photovoltaic module and load simultaneously, the additional energy collected by the PV module slows the rate of discharge of the battery, prolonging the time the battery can operate before it must be charged. To characterize the system behavior under these conditions, the PV module, battery and load were connected in parallel as shown in Figure 5.8a. The current into the battery in this configuration, I_{bat} , is equal to the difference between PV and load currents, $I_{PV} - I_{load}$; the sign of this value determines whether the battery will charge or discharge. Here, the “on” state lasted for 30 seconds and the “off” state for 90 seconds, giving a duty cycle of 25% and an average load current of 5.75 mA. For both the indoor illumination conditions, 0.9 and 4.8 mW/cm^2 , the

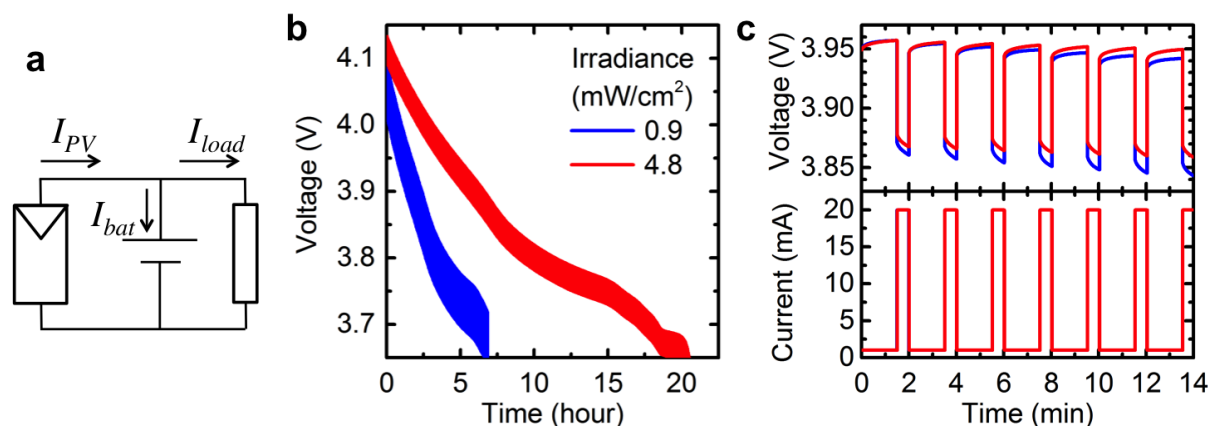


Figure 5.8: (a) Circuit schematic of PV module, battery and load, indicating currents flowing in each component. (b) Discharge curves of the battery with two PV module irradiance conditions. The load alternates between 20 mA for 30 seconds and 1 mA for 90 seconds. (c) Closeup of the battery voltage and load current waveforms shown in (b) over a few load cycles.

current produced by the PV module is less than 5.75 mA, so the battery would be expected to discharge overall. Specifically, with PV module currents of 0.46 and 3.9 mA, respectively, the battery should discharge at average currents of 5.3 and 1.8 mA. The voltage was monitored with both illumination conditions as the battery discharged, as shown in Figure 5.8b and c. Figure 5.8b shows the full discharge curves, while Figure 5.8c shows a closeup of a few load cycles, allowing the voltage and current waveforms to be distinguished. The difference between the voltage under 20 mA load and under 1 mA load is due to the higher potential drop of the battery under the higher discharge rate. Increasing the irradiance from 0.9 to 4.8 mW/cm^2 clearly increases the lifetime of the battery. For example, under 0.9 mW/cm^2 it took 4.8 hours for the voltage in the 20 mA load phase to decrease from 4.0 V to 3.7 V. Under 4.8 mW/cm^2 , this same decrease occurred over 15 hours, 3 times longer. This is consistent with the threefold reduction in the calculated average discharge current. The slower discharge under higher irradiance is visible after just a few cycles in Figure 5.8c.

While increasing the irradiance has been proven effective at slowing the discharge of the battery, in some applications the battery may be required to last even longer between charging, or it may not be feasible for the user of the device to adjust the illumination. In these cases, it is preferable to adjust the load duty cycle instead. If the average load current matches the PV module current exactly, the battery lifetime can in theory be extended indefinitely. For example, if the battery begins in a charged state with voltage of 4.1 V, the PV module current under 4.8 mW/cm^2 at this voltage is 3.4 mA. If the time in the “on” state remains at 30 seconds, the load should be off for 210 seconds to give an average current of 3.4 mA matching the PV current. It was determined experimentally that a 220-

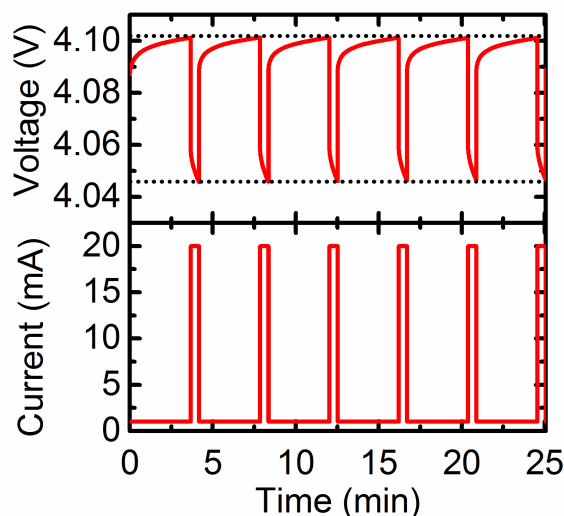


Figure 5.9: Battery voltage and load current waveforms with the load alternating between 20 mA for 30 seconds and 1 mA for 220 seconds. The dotted black lines are a guide to the eye indicating that the battery voltage at the end of each cycle does not change.

second “off” state or duty cycle of 12% resulted in no net charge or discharge of the battery, which is in good agreement with the calculated value. Figure 5.9 shows the battery voltage measured over a few load cycles with these conditions, indicating that the battery voltage (and therefore also its state of charge) is the same after each load cycle.

5.4 Energy systems with battery management

Battery management electronics are a crucial part of systems that contain rechargeable batteries, as they prevent over-voltage and under-voltage conditions that can irreversibly damage the battery. In the previous section, the battery was manually disconnected from the system when it reached its maximum or minimum voltage. However, by incorporating battery management electronics that continuously monitor the condition of the battery, the system can operate safely and reliably over many cycles without any user intervention. One critical function of a battery management system is to terminate charging when the battery reaches its maximum voltage, preventing the over-voltage condition. Battery management circuits for lithium batteries often enforce a constant current-constant voltage charging profile, meaning they charge the battery most of the way at a constant high rate until it reaches its maximum voltage, at which point the charging rate decreases until the battery is fully charged. The second major function is to disconnect the load from the battery when it reaches its minimum voltage, preventing the under-voltage condition. Some battery management circuits also monitor the battery temperature and adjust the charging and discharging conditions

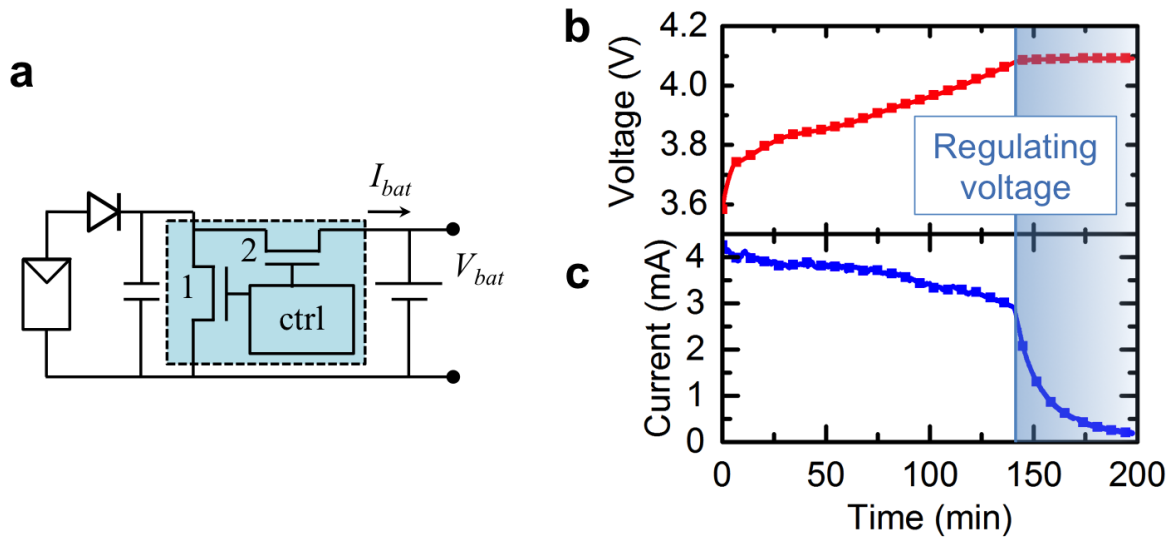


Figure 5.10: Battery charging with solar module and battery management system. (a) Schematic of the experimental setup. The blue shaded region denotes the battery management IC, highlighting its power transistors and control system. (b) Voltage of the battery (V_{bat}) over time during charging. (c) Charging current of the battery (I_{bat}) over the same time period. In the blue shaded region from 140 minutes onward, the battery voltage is maintained at 4.1 V and the excess current from the solar module is shunted away through transistor 1.

appropriately.

5.4.1 System with amorphous silicon solar module

This section describes a system similar to that in the previous section and in [1], but with the addition of a battery management circuit. The solar module was the same Powerfilm amorphous silicon module described in [1], with the current-voltage characteristic shown in Figure 5.5a. To reduce the charging time for demonstration purposes, a smaller (9.4 mAh) battery, of the same lithium-ion chemistry and thin-film architecture as that presented in [1], was used. The battery management system consisted of the same blocking diode described in the previous section (ON Semiconductor MBRM130LT3G), a shunt battery management integrated circuit (IC) designed for lithium-ion batteries (Linear Technology LTC4071) [35], and a 1 μ F decoupling capacitor. To charge the battery, the solar module was exposed to 4.8 mW/cm² irradiance with the CFL; to discharge it, the solar module was disconnected and a 1 k Ω resistive load was connected. The system configurations for charging and discharging are shown in Figure 5.10a and 5.11a, respectively.

The maximum and minimum allowable battery voltages can be programmed through the connection of certain pins on the battery management IC. Here, the maximum voltage was

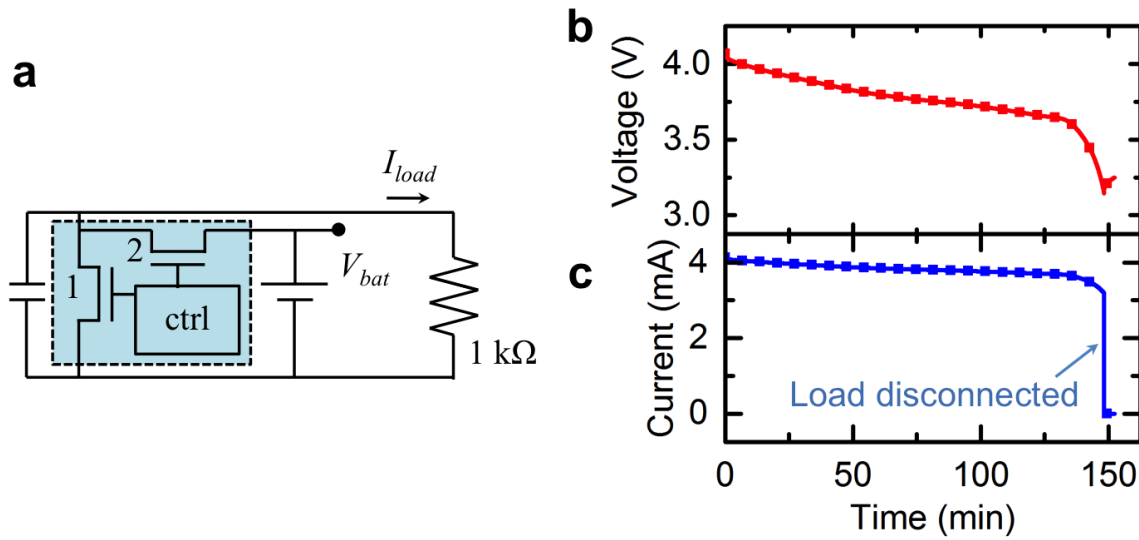


Figure 5.11: Battery discharging with battery management system and $1\text{ k}\Omega$ load. (a) Schematic of the experimental setup. The blue shaded region denotes the battery management IC. (b) Voltage of the battery (V_{bat}) over time during discharging. (c) Current into the resistor (I_{load}) over the same time period.

set to 4.1 V and the minimum voltage to 3.2 V. The control system within the IC (labeled “ctrl” in Figure 5.10a) controls the two power transistors (labeled “1” and “2”) based on the voltage of the battery. During normal operation, when the battery is neither fully charged nor fully discharged, transistor 1 is off and transistor 2 is on, allowing current to flow in or out of the battery.

The measured battery voltage and current are shown in 5.10b and c, respectively, during solar charging. As the battery charges, the voltage increases as seen in Figure 5.10b. Increasing the voltage causes the solar module current to decrease according to its I-V characteristic, resulting in a modest decrease of the battery charging current as seen in Figure 5.10c. After 140 minutes of charging, the battery voltage approached its preset maximum value of 4.1 V, and the battery management system turned on transistor 1 to shunt away the unnecessary current from the PV module. In this stage, represented by the blue shaded region in Figure 5.10b and c, the battery voltage was regulated at 4.1 V and the battery current gradually decayed to zero. The output current of the PV module remained approximately constant at 2.7 mA during this stage, with an increasing portion being directed through transistor 1 instead of the battery.

When a resistive load is connected and the solar module is disconnected, the battery voltage decreases as seen in Figure 5.11b. The corresponding current from the battery into the resistor is shown in Figure 5.11c. After 148 minutes, when the battery voltage reached the preset minimum value of 3.2 V, corresponding to the fully discharged state, the circuit disconnected the load from the battery by turning off transistor 2. The load current dropped

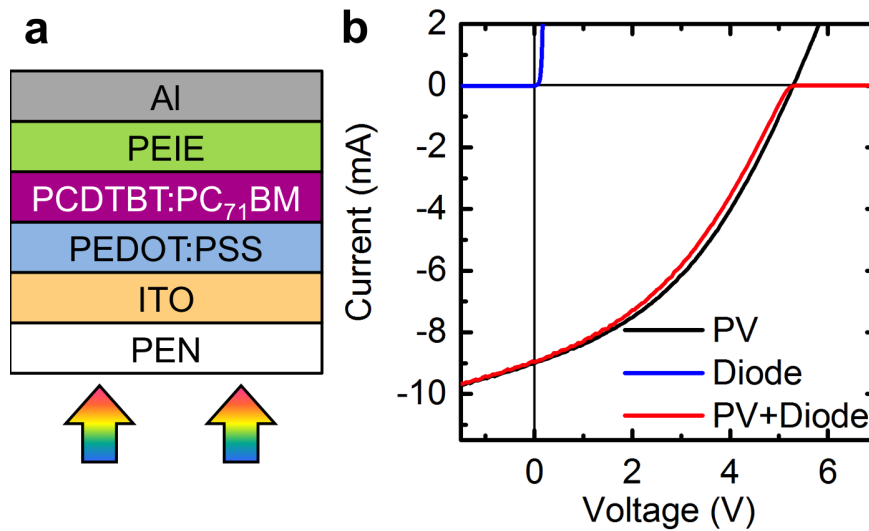


Figure 5.12: (a) Cell structure used in the printed organic PV module: polyethylene naphthalate (PEN) substrate, indium tin oxide (ITO) transparent anode, poly(3,4-ethylenedioxythiophene): poly(styrenesulfonate) (PEDOT:PSS) hole transport layer, poly[N-9'-heptadecanyl-2,7-carbazole-alt-5,5-(4,7-di-2-thienyl-2',1',3'-benzothiadiazole)]: 6,6]-phenyl C₇₁-butyric acid methyl ester (PCDTBT:PC₇₁BM) active layer, polyethyleneimine ethoxylated (PEIE) cathode interlayer, and aluminum cathode. (b) Current-voltage characteristics of printed organic PV module under sunlight, blocking diode, and PV module with blocking diode in series.

to zero as indicated in Figure 5.11c, causing the voltage drop due to the battery's internal resistance to go to zero as well, and as a result the battery voltage in Figure 5.11b recovered slightly.

5.4.2 System with organic solar module

In addition to the off-the-shelf amorphous silicon solar module, the battery can be charged using a custom in-house organic photovoltaic (OPV) module. The printed organic module developed in Section 2.4, for example, has a similar open-circuit voltage to the amorphous silicon module and is thus compatible with lithium-ion battery systems. The current under a given irradiance is lower for the organic module, due to the smaller active area. Still, under sunlight, the output current of several milliamps is adequate to provide a full charge of the battery. The current-voltage characteristics of the printed OPV module under sunlight are shown in Figure 5.12 along with the characteristics of the blocking diode and the structure of the organic solar module. As in the previous sections with the silicon module, the blocking diode effectively prevented current flow into the OPV module at voltages greater than V_{OC} , and added minimal voltage drop compared to the voltage of the solar module.

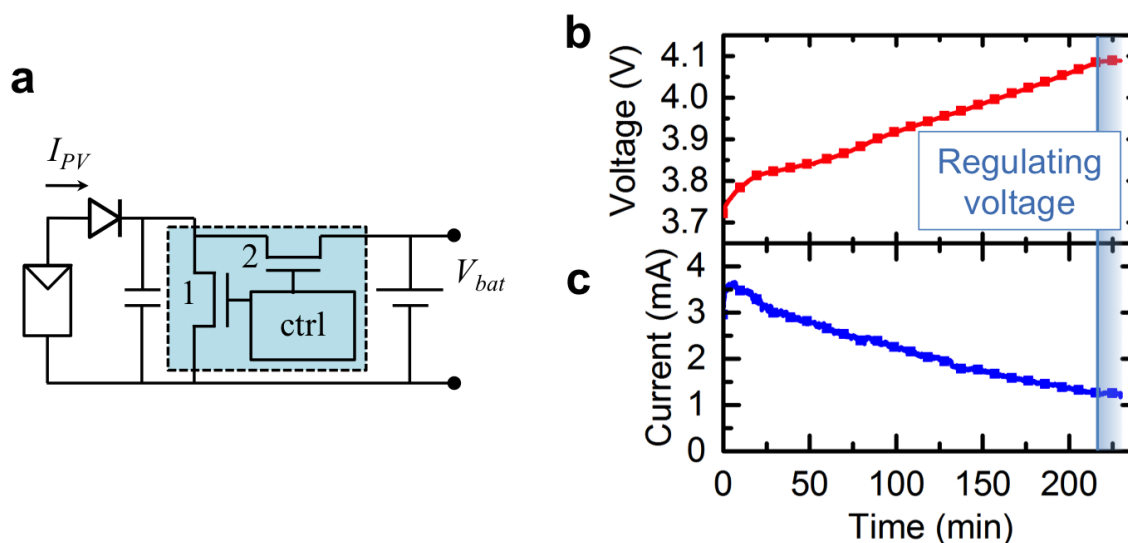


Figure 5.13: Battery charging with organic photovoltaic module and battery management system. (a) Schematic of the experimental setup. The blue shaded region denotes the battery management IC. (b) Battery voltage (V_{bat}) and (c) solar module output current (I_{PV}) over time during charging.

As shown in Figure 5.13, the 9.4 mAh flexible lithium-ion battery was charged using the printed organic solar module under full-sun illumination. The battery management IC was again set to enforce a maximum battery voltage of 4.1 V, and the battery voltage was monitored as seen in Figure 5.13b. Figure 5.13c shows the output current of the solar module during the same time period. A decline in solar module current during charging is evident, due to a combination of the increasing battery voltage and the heating and degradation of the module that occur in the presence of strong sunlight, oxygen and moisture. Nevertheless, the battery voltage did reach its 4.1 V maximum after about 220 minutes, as indicated in the blue shaded region of Figure 5.13b and c, and the battery management system regulated the voltage as described before.

PCDTBT is a relatively stable material and can demonstrate operating lifetimes on the order of years when encapsulated in glass [36]. However, degradation of the PEDOT:PSS hole transport layer and low work function metal cathode are known to limit the lifetime, as are photochemical reactions that can occur in the PCDTBT itself upon prolonged exposure to ultraviolet and visible light [37]. Furthermore, the PEN substrate is not as effective as glass at preventing the ingress of moisture and oxygen, which speed up degradation [38]. Therefore, use of an inverted structure without the PEDOT:PSS or low work function metal, as well as incorporation of an improved barrier material in the PEN substrate, would be expected to improve the lifetime [37, 38].

5.4.3 Implications for maximum power point tracking

Some solar power systems, particularly those with higher power, include maximum power point tracking (MPPT) circuits to increase the energy collection efficiency, as discussed in Section 1.3.1. By comparing the power delivered to the battery with the actual maximum power point of the solar module, the efficiency and the potential benefit of including MPPT can be assessed. Here, this analysis is done for the system described in Section 5.4.1, where the lithium-ion battery is charged by an amorphous silicon solar module under 4.8 mW/cm^2 illumination with a CFL.

The maximum power point of the solar module occurs around 3.7 V, with a current of 4.3 mA and power of 16 mW. In the first 140 minutes of charging, before the shunt regulation was in use, a total energy of 118 J was delivered to the battery. This equates to an average power of 14 mW, 88% of the maximum power point. Therefore, if the solar module were always operating at its maximum power point, 12% less time or 123 minutes would be needed to collect the same 118 J of energy. This result provides an important guideline in the selection of a MPPT scheme: the efficiency of the MPPT circuit, including both the tracking accuracy and the losses in the circuit components, must be greater than 88% to warrant inclusion in the system.

While high-power MPPT systems can be very efficient, the efficiencies of milliwatt-scale MPPT systems reported to date are rarely much greater than 88%, because the losses in the circuitry are a more significant fraction of the total power transferred [39–44]. Furthermore, such systems typically consist of several electronic components including silicon ICs. Therefore, it is likely that increasing the solar module area slightly would be a more cost-effective means of increasing the output power than incorporating a MPPT circuit for a battery charging application such as this. For example, at the time of writing, the price of the Powerfilm solar modules was about 10 cents per square centimeter [45]. In the example considered here, if 16 mW of output power were required rather than the 14 mW that were delivered, without including MPPT, an additional 8 cm^2 of solar module area would be needed, costing approximately 80 cents. By comparison, the cost of a commercially available MPPT IC for milliwatt-scale power levels is \$1.25 [46]. The costs of the additional required passive components and the processes used to attach the components would further increase this value.

It is important to note that the potential benefit of including MPPT depends strongly on what loads and energy storage devices are included in the system. The reason the PV module in this example system is maintained so close to its maximum power point without MPPT is that it was chosen to match the battery voltage, which varies relatively little over the course of charging. Some applications of PV energy harvesting may include supercapacitors, whose voltage varies much more substantially as they charge, as the sole energy storage element. Others may have no energy storage at all; in these cases a change in the illumination conditions or the load impedance could shift the operating point dramatically if MPPT is not included. Applications such as these continue to motivate the development of efficient MPPT solutions for solar energy harvesting [41–43]. To mitigate the increased cost and

bulkiness caused by the addition of power electronics such as MPPT, it is of interest to explore the use of printed and flexible components in power electronics, as will be discussed in the following Chapter 6.

5.5 Conclusion

This chapter has presented a set of flexible thin-film energy harvesting and storage systems incorporating photovoltaic modules and lithium-ion batteries. A system comprising a 48 mAh battery and an amorphous silicon solar module with similar footprint was designed for wearable electronics applications. Battery charging was demonstrated with irradiance ranging from 0.9 to 100 mW/cm², representing both indoor and outdoor illumination conditions. Increasing the photovoltaic power was shown to increase the length of time the battery could power a load before becoming fully discharged. Additionally, optimizing the load duty cycle to balance the average load current and the photovoltaic module current allowed the battery to be maintained at a constant state of charge. Smaller systems based on a 9.4 mAh battery were also demonstrated, using either an amorphous silicon solar module or the in-house printed organic photovoltaic module presented in Chapter 2. To enable truly robust and independent system operation, a battery management IC was integrated with the battery and solar module in both of these smaller systems. The effectiveness of the IC at maintaining the battery within safe voltage limits during charging and discharging was verified.

The basic design principles discussed in this chapter can be applied to many systems, including those with other types of energy harvesting, energy storage, or loads. For example, regardless of the specific application requirements, it is crucial to use a battery with appropriate voltage, capacity, rate capability, and mechanical properties, and to incorporate battery management circuitry. By designing the energy harvester to have high efficiency when operated at the battery voltage, high overall system performance can be achieved without needing to add power electronics for maximum power point tracking. Additionally, the process of matching the average currents of the load and energy harvester can be extended to other types of harvesters and loads. If the load contains devices such as microcontrollers that perform computation, it may be possible to monitor the battery voltage and adjust the duty cycle in real time as illumination conditions change, to ensure the battery remains charged over extended periods of time.

These findings emphasize the importance of considering all components of an electronic system, both power sources and loads, in a single holistic design process. The ideal choices of load duty cycle, battery architecture, energy harvester characteristics, and power electronics all depend on each other, as well as on conditions of use such as amount of light exposure. Co-design and integration of the components can be facilitated by the use of customizable and high-throughput printing processes. Overall, integrated energy harvesting and storage systems in flexible thin-film form factors such as those presented in this chapter can help the vision of ubiquitous, flexible, wireless electronics to be realized.

5.6 References

1. Ostfeld, A. E., Gaikwad, A. M., Khan, Y. & Arias, A. C. High-performance flexible energy storage and harvesting system for wearable electronics. *Scientific Reports* **6**, 26122 (2016).
2. Van Bavel, M., Leonov, V., Yazicioglu, R. F., Torfs, T., Van Hoof, C., Posthuma, N. E. & Vullers, R. J. Wearable battery-free wireless 2-channel EEG systems powered by energy scavengers. *Sensors & Transducers Journal* **94**, 103–115 (2008).
3. MacKenzie, J. D. & Ho, C. Perspectives on energy storage for flexible electronic systems. *Proceedings of the IEEE* **103**, 535–553 (2015).
4. Yan, C., Wang, J. & Lee, P. S. Stretchable graphene thermistor with tunable thermal index. *ACS Nano* **9**, 2130–2137 (2015).
5. Song, Z., Wang, X., Lv, C., An, Y., Liang, M., Ma, T., He, D., Zheng, Y.-J., Huang, S.-Q., Yu, H. & Jiang, H. Kirigami-based stretchable lithium-ion batteries. *Scientific Reports* **5**, 10988 (2015).
6. Dou, L., You, J., Hong, Z., Xu, Z., Li, G., Street, R. A. & Yang, Y. 25th anniversary article: A decade of organic/polymeric photovoltaic research. *Advanced Materials* **25**, 6642–6671 (2013).
7. Gwon, H., Hong, J., Kim, H., Seo, D.-H., Jeon, S. & Kang, K. Recent progress on flexible lithium rechargeable batteries. *Energy & Environmental Science* **7**, 538–551 (2014).
8. Hu, Y. & Sun, X. Flexible rechargeable lithium ion batteries: Advances and challenges in materials and process technologies. *Journal of Materials Chemistry A* **2**, 10712–10738 (2014).
9. Li, L., Wu, Z., Yuan, S. & Zhang, X.-B. Advances and challenges for flexible energy storage and conversion devices and systems. *Energy & Environmental Science* **7**, 2101–2122 (2014).
10. Kim, J.-S., Lee, Y.-H., Lee, I., Kim, T.-S., Ryou, M.-H. & Choi, J. W. Large area multi-stacked lithium-ion batteries for flexible and rollable applications. *Journal of Materials Chemistry A* **2**, 10862–10868 (2014).
11. Wang, X., Lu, X., Liu, B., Chen, D., Tong, Y. & Shen, G. Flexible energy-storage devices: Design consideration and recent progress. *Advanced Materials* **26**, 4763–4782 (2014).
12. Zhou, G., Li, F. & Cheng, H.-M. Progress in flexible lithium batteries and future prospects. *Energy & Environmental Science* **7**, 1307–1338 (2014).
13. Gaikwad, A. M., Arias, A. C. & Steingart, D. A. Recent progress on printed flexible batteries: Mechanical challenges, printing technologies, and future prospects. *Energy Technology* **3**, 305–328 (2015).

14. Bahk, J.-H., Fang, H., Yazawa, K. & Shakouri, A. Flexible thermoelectric materials and device optimization for wearable energy harvesting. *Journal of Materials Chemistry C* **3**, 10362–10374 (2015).
15. Ha, M., Park, J., Lee, Y. & Ko, H. Triboelectric generators and sensors for self-powered wearable electronics. *ACS Nano* **9**, 3421–3427 (2015).
16. Misra, V., Bozkurt, A., Calhoun, B., Jackson, T., Jur, J., Lach, J., Lee, B., Muth, J., Oralkan, O., Ozturk, M., Trolrier-McKinstry, S., Vashaee, D., Wentzloff, D. & Zhu, Y. Flexible technologies for self-powered wearable health and environmental sensing. *Proceedings of the IEEE* **103**, 665–681 (2015).
17. Fan, F. R., Tang, W. & Wang, Z. L. Flexible nanogenerators for energy harvesting and self-powered electronics. *Advanced Materials*, 4283–4305 (2016).
18. Khan, A., Abas, Z., Kim, H. S. & Oh, I.-K. Piezoelectric thin films: an integrated review of transducers and energy harvesting. *Smart Materials and Structures* **25**, 053002 (2016).
19. Garcia-Valverde, R., Villarejo, J. A., Hösel, M., Madsen, M. V., Søndergaard, R. R., Jørgensen, M. & Krebs, F. C. Scalable single point power extraction for compact mobile and stand-alone solar harvesting power sources based on fully printed organic photovoltaic modules and efficient high voltage DC/DC conversion. *Solar Energy Materials and Solar Cells* **144**, 48–54 (2016).
20. Minnaert, B. & Veelaert, P. *The appropriateness of organic solar cells for indoor lighting conditions* in *SPIE Photonics Europe* (eds Heremans, P. L., Coehoorn, R. & Adachi, C.) (International Society for Optics and Photonics, Brussels, Belgium, 2010), 77221P–1 – 77221P–11. doi:10.1117/12.854774. <<http://proceedings.spiedigitallibrary.org/proceeding.aspx?articleid=749480>>.
21. Nelson, J. *The Physics of Solar Cells* (Imperial College Press, London, 2003).
22. Krebs, F. C., Fyenbo, J., Tanenbaum, D. M., Gevorgyan, S. A., Andriessen, R., van Remoortere, B., Galagan, Y. & Jørgensen, M. The OE-A OPV demonstrator anno domini 2011. *Energy & Environmental Science* **4**, 4116–4123 (2011).
23. Carmo, J. P., Gomes, J. M., Gonçalves, L. M. & Correia, J. H. A flexible thin-film for powering stand alone electronic devices. *Measurement* **46**, 4145–4151 (2013).
24. Dennler, G., Bereznev, S., Fichou, D., Holl, K., Ilic, D., Koeppe, R., Krebs, M., Labouret, A., Lungenschmied, C., Marchenko, A., Meissner, D., Mellikov, E., Méot, J., Meyer, A., Meyer, T., Neugebauer, H., Öpik, A., Sariciftci, N., Taillemite, S. & Wöhrle, T. A self-rechargeable and flexible polymer solar battery. *Solar Energy* **81**, 947–957 (2007).
25. Kim, J.-S., Ko, D., Yoo, D.-J., Jung, D. S., Yavuz, C. T., Kim, N.-I., Choi, I.-S., Song, J. Y. & Choi, J. W. A half millimeter thick coplanar flexible battery with wireless recharging capability. *Nano Letters* **15**, 2350–2357 (2015).

26. Lee, Y.-H., Kim, J.-S., Noh, J., Lee, I., Kim, H. J., Choi, S., Seo, J., Jeon, S., Kim, T.-S., Lee, J.-Y. & Choi, J. W. Wearable textile battery rechargeable by solar energy. *Nano Letters* **13**, 5753–5761 (2013).
27. Hu, L., Wu, H., La Mantia, F., Yang, Y. & Cui, Y. Thin, flexible secondary Li-ion paper batteries. *ACS Nano* **4**, 5843–5848 (2010).
28. Koo, M., Park, K.-I., Lee, S. H., Suh, M., Jeon, D. Y., Choi, J. W., Kang, K. & Lee, K. J. Bendable inorganic thin-film battery for fully flexible electronic systems. *Nano Letters* **12**, 4810–4816 (2012).
29. Singh, N., Galande, C., Miranda, A., Mathkar, A., Gao, W., Reddy, A. L. M., Vlad, A. & Ajayan, P. M. Paintable battery. *Scientific Reports* **2**, 481 (2012).
30. Sun, K., Wei, T. S., Ahn, B. Y., Seo, J. Y., Dillon, S. J. & Lewis, J. A. 3D printing of interdigitated Li-ion microbattery architectures. *Advanced Materials* **25**, 4539–4543 (2013).
31. Xu, S., Zhang, Y., Cho, J., Lee, J., Huang, X., Jia, L., Fan, J. A., Su, Y., Su, J., Zhang, H., Cheng, H., Lu, B., Yu, C., Chuang, C., Kim, T.-I., Song, T., Shigeta, K., Kang, S., Dagdeviren, C., Petrov, I., Braun, P. V., Huang, Y., Paik, U. & Rogers, J. A. Stretchable batteries with self-similar serpentine interconnects and integrated wireless recharging systems. *Nature Communications* **4**, 1543 (2013).
32. Kim, S.-H., Choi, K.-H., Cho, S.-J., Choi, S., Park, S. & Lee, S.-Y. Printable solid-state lithium-ion batteries: A new route toward shape-conformable power sources with aesthetic versatility for flexible electronics. *Nano Letters* **15**, 5168–5177 (2015).
33. Dieffenderfer, J. P., Beppler, E., Novak, T., Whitmire, E., Jayakumar, R., Randall, C., Qu, W., Rajagopalan, R. & Bozkurt, A. *Solar powered wrist worn acquisition system for continuous photoplethysmogram monitoring in Engineering in Medicine and Biology Society (EMBC), 2014 36th Annual International Conference of the IEEE (IEEE, Chicago, IL, 2014), 3142–3145. doi:10.1109/EMBC.2014.6944289.*
34. Lochner, C. M., Khan, Y., Pierre, A. & Arias, A. C. All-organic optoelectronic sensor for pulse oximetry. *Nature Communications* **5**, 5745 (2014).
35. Linear Technology. *LTC4071: Li-Ion/Polymer Shunt Battery Charger System with Low Battery Disconnect* 2011. <<http://www.linear.com/docs/29020>> (visited on 07/07/2016).
36. Peters, C. H., Sachs-Quintana, I. T., Kastrop, J. P., Beaupré, S., Leclerc, M. & McGehee, M. D. High efficiency polymer solar cells with long operating lifetimes. *Advanced Energy Materials* **1**, 491–494 (2011).
37. Beaupré, S. & Leclerc, M. PCDTBT: En route for low cost plastic solar cells. *Journal of Materials Chemistry A* **1**, 11097 (2013).
38. Jørgensen, M., Norrman, K. & Krebs, F. C. Stability/degradation of polymer solar cells. *Solar Energy Materials and Solar Cells* **92**, 686–714 (2008).

39. Dondi, D., Bertacchini, A., Brunelli, D., Larcher, L. & Benini, L. Modeling and optimization of a solar energy harvester system for self-powered wireless sensor networks. *IEEE Transactions on Industrial Electronics* **55**, 2759–2766 (2008).
40. Lopez-Lapena, O., Penella, M. T. & Gasulla, M. A new MPPT method for low-power solar energy harvesting. *IEEE Transactions on Industrial Electronics* **57**, 3129–3138 (2010).
41. Simjee, F. I. & Chou, P. H. Efficient charging of supercapacitors for extended lifetime of wireless sensor nodes. *IEEE Transactions on Power Electronics* **23**, 1526–1536 (2008).
42. Grasso, A. D. & Pennisi, S. Micro-scale inductorless maximum power point tracking DC-DC converter. *IET Power Electronics* **6**, 1634–1639 (2013).
43. Wang, Y., Liu, Y., Wang, C., Li, Z., Sheng, X., Lee, H. G., Chang, N. & Yang, H. Storage-less and converter-less photovoltaic energy harvesting with maximum power point tracking for internet of things. *IEEE Transactions on Computer-Aided Design of Integrated Circuits and Systems* **35**, 173–186 (2016).
44. ST Microelectronics. *SPV1040: High efficiency solar battery charger with embedded MPPT* 2013. <<http://www.st.com/resource/en/datasheet/spv1040.pdf>> (visited on 06/30/2016).
45. Jameco. *Edu & Hobby: Muscle Wires, Compass Modules & Solar Products* 2016. <<ftp://ftp.jameco.com/Archive/Catalog%20161/EduHobby.pdf>> (visited on 07/01/2016).
46. ST Microelectronics. *SPV1040: High efficiency solar battery charger with embedded MPPT* 2016. <http://www.st.com/content/st_com/en/products/power-management/photovoltaic-ics/mppt-dc-dc-converters/spv1040.html> (visited on 07/01/2016).

Chapter 6

Printed Components for Power Electronics

This chapter reports on the design, manufacturing, and evaluation of printed passive components for applications in power electronics. Screen-printed inductors, capacitors, resistors, and an RLC circuit on flexible plastic substrates are presented. By optimizing the geometry, ink and fabrication process for the inductors, inductances of several μH with quality factors up to 35 are achieved. Printed inductors and resistors are incorporated into a step-up voltage regulator circuit, with efficiency surpassing 85% of that of a circuit using all conventional surface-mount components, demonstrating their potential to replace surface-mount components in a DC-DC converter. An example application, powering organic light-emitting diodes at constant voltage using a flexible lithium-ion battery as the power source, is presented. Portions of the work in this chapter are published in [1].

6.1 Introduction

Great strides have been made toward high-performing flexible energy sources and loads for applications in wearable and large-area electronics and the Internet of Things [2–4]. However, combining these individual components together into a complete electronic system typically also requires power electronics to overcome any mismatch between the source behavior and the loads' requirements. For example, batteries produce a variable voltage dependent on their state of charge. If a load requires a constant voltage, or a higher voltage than the battery can produce, then power electronics are necessary. Power electronics use active components, transistors, to perform switching and control functions, as well as passive components—inductors, capacitors, and resistors. In a switching voltage regulator circuit, for example, inductors are employed to store energy during each switching cycle, capacitors are used to reduce voltage ripple, and the voltage measurement required for feedback control is accomplished using a resistor divider.

Power electronics appropriate for the demands of low-power portable and wearable de-

VICES, which require a few volts and a few milliamps, typically operate at frequencies in the range of hundreds of kHz to a few MHz, and require inductance and capacitance of several μH and several μF , respectively [5]. The conventional approach for manufacturing these circuits is to solder discrete components onto a rigid printed circuit board (PCB). While the active components of a power electronic circuit are often combined into a single silicon integrated circuit (IC), the passive components are usually external, either to allow customization of the circuit or because the required inductance and capacitance values are too large to be achieved in silicon.

Fabrication of electronic devices and circuits by additive printing processes offers a number of advantages in terms of simplicity and cost when compared to the conventional PCB-based manufacturing techniques. First, since many components of a circuit require the same materials, such as metal for contacts and interconnects, printing allows multiple components to be fabricated simultaneously, with relatively few processing steps and few sources of materials [6]. Replacing subtractive processes such as photolithography and etching with additive processes further reduces process complexity as well as materials waste [7–10]. In addition, the low temperatures used in printing are compatible with flexible and inexpensive plastic substrates, allowing large areas to be covered with electronics using high-speed roll-to-roll manufacturing processes [7, 11]. For applications that cannot be fully realized using printed components, hybrid approaches have been developed in which surface-mount technology (SMT) components are attached at low temperature to flexible substrates alongside the printed components [12–14]. In such hybrid approaches, replacing as many SMT components as possible with their printed counterparts is still desirable to reap the benefits of the additive processes and improve the overall flexibility of the circuit. SMT inductors are particularly bulky and therefore particularly desirable to replace with a planar design [15]. To achieve flexible power electronics, a combination of SMT active components and screen-printed passive components is proposed. Of the various technologies for fabricating printed electronics, screen printing is especially well suited for passive components because of its large film thickness (which is necessary to minimize series resistance of metallic features) and its high printing speed, even when covering centimeter-scale areas with material [16].

It is essential to minimize losses in passive components for power electronics, since the efficiency of the circuit directly affects the size of the energy source that is required to power a system. This is particularly challenging for printed inductors, which consist of long coils and are therefore susceptible to high series resistance. As a result, although there has been some effort toward minimizing resistance of printed coils [17–20], there remains a lack of efficient printed passive components for power electronics. To date, many reported printed passive components on flexible substrates are designed to operate in resonant circuits for radio frequency identification (RFID) or energy harvesting purposes [18–25]. Others focus on materials or fabrication process development and demonstrate general-purpose components that are not optimized for a particular application [17, 26–28]. Power electronic circuits such as voltage regulators, by contrast, tend to utilize larger components than the typical demonstrations of printed passives and do not require resonance, thus demanding different component designs.

This chapter presents the design and optimization of screen-printed inductors in the μH range to achieve minimal series resistance and high performance at frequencies relevant to power electronics. Screen-printed inductors, capacitors, and resistors with various component values are fabricated on flexible plastic substrates. The suitability of these components for flexible electronics is first demonstrated in a simple RLC circuit. Printed inductors and resistors are then integrated with an IC to form a step-up voltage regulator. Finally, the voltage regulator is used to power organic light-emitting diodes (OLEDs) from a flexible lithium-ion battery.

6.2 Experimental details

All layers of the passive components were screen printed onto flexible polyethylene terephthalate (PET) substrates, $76\ \mu\text{m}$ in thickness, using an Asys ASP01M screen printer and stainless steel screens supplied by Dynamesh Inc. Mesh size was 400 threads per inch for the metal layers and 250 threads per inch for the dielectric and resistor layers. Screen printing was performed using a squeegee force of 55 N, print speed of 60 mm/s, snap-off distance of 1.5 mm, and Serilor squeegees with hardness of 65 durometer (for metal and resistor layers) or 75 durometer (for dielectric layer).

Conductive layers—inductors and the contacts to the capacitors and resistors—were printed from either Dupont 5082 [29] or Dupont 5064H [30] silver micro-flake ink, or Inktec PR-010 silver nanoparticle ink [31]. Resistors were printed from Dupont 7082 carbon conductor. For the capacitor dielectric, Conductive Compounds BT-101 barium titanate dielectric was used. Each coat of dielectric was produced using a double pass (wet-wet) print cycle to improve uniformity of the film. For each component, the effect of multiple print cycles on component performance and variability was examined. Samples made with multiple coats of the same material were allowed to dry for 2 minutes at 70°C between coats. After the final coat of each material, the samples were baked at 140°C for 10 minutes to ensure complete drying. The screen printer's automatic alignment feature was used to align subsequent layers. Contacts to the center of the inductor were made by cutting a via into the center pad and stencil printing a trace on the backside of the substrate with Dupont 5064H ink. Interconnects between printed devices were also stencil printed from Dupont 5064H. To demonstrate a hybrid voltage regulator circuit combining printed components and surface-mount components together, printed components were attached to a PCB or flex-PCB using Circuit Works CW2400 conductive epoxy and surface-mount components were attached using conventional soldering.

Film thickness was measured with a Dektak stylus profilometer. DC resistances, voltages, and currents were measured with a digital multimeter. AC impedance of inductors, capacitors, and circuits was measured with an Agilent E4980 LCR meter for frequencies below 1 MHz and an Agilent E5061A network analyzer for frequencies above 500 kHz. Voltage regulator waveforms were measured with a Tektronix TDS 5034 oscilloscope.

Scanning electron microscope (SEM) imaging of inductors and capacitors was performed

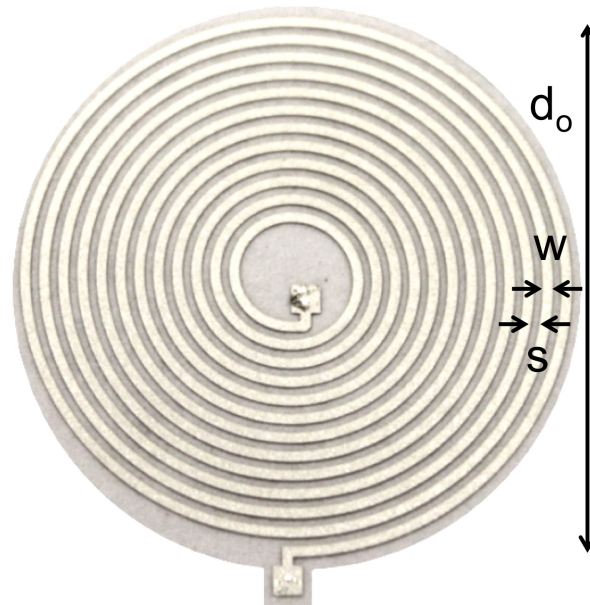


Figure 6.1: Photograph of a screen-printed inductor, indicating geometric parameters. Diameter is 3 cm and $n = 12$.

by Dr. Igal Deckman, and lithium-ion battery fabrication was performed by Dr. Abhinav Gaikwad, as described in [1]. Fabrication of the OLEDs was carried out by Claire Lochner as described in [32].

6.3 Inductors

To design printed inductors for power electronics, the inductance and DC resistance were first predicted for a range of inductor geometries, based on the current sheet model presented in Mohan et al. [33]; inductors of several geometries were fabricated to confirm the accuracy of the model. A circular shape was selected for the inductors in this work because higher inductance can be achieved with lower resistance compared to polygon geometries [34]. The effects of the type of ink and the number of print cycles on resistance and achievable print resolution were determined. These results were then used along with the current sheet model to design 4.7 μH and 7.8 μH inductors optimized for minimum DC resistance.

6.3.1 Geometry and modeling

The inductance and DC resistance of a spiral inductor can be described by a few parameters: the outer diameter d_o , turn width w and spacing s , number of turns n , and the sheet resistance R_{sheet} of the conductor. Figure 6.1 shows a photograph of a screen-printed circular inductor

with $n = 12$, indicating the geometric parameters that determine its inductance. Inductance was calculated for a range of inductor geometries according to the current sheet model of Mohan et al. [33], in which

$$L = \frac{\mu n^2 d_{avg}}{2} \left[\ln \left(\frac{2.46}{\rho} \right) + 0.20\rho^2 \right] \quad (6.1)$$

where μ is the permeability of the core (in this case, air); d_{avg} is the average diameter:

$$d_{avg} = 0.5(d_{out} + d_{in}) \quad (6.2)$$

ρ is the fill ratio:

$$\rho = \frac{d_{out} - d_{in}}{d_{out} + d_{in}} \quad (6.3)$$

and d_{in} is the inner diameter:

$$d_{in} = d_{out} - 2n(w + s) \quad (6.4)$$

The DC resistance is given by

$$R_{dc} = R_{sheet}l/w \quad (6.5)$$

where the length of the spiral is:

$$l = \pi n[d_{in} + (w + s)(n - 1)] \quad (6.6)$$

and the sheet resistance is:

$$R_{sheet} = 1/(\sigma t) \quad (6.7)$$

for conductivity σ and thickness t .

At high frequencies, the skin effect and parasitic capacitance change an inductor's resistance and inductance from their DC values. It is desirable to operate the inductor at frequencies low enough that these effects are negligible and the device behaves as a constant inductance with a constant resistance equal to R_{dc} in series. Thus, this work analyzes the relationships between the geometric parameters, inductance and DC resistance, and the results are used to obtain a given inductance with minimum DC resistance.

Inductance and resistance were calculated for a range of geometric parameters achievable with screen printing and expected to give inductances in the μH range. Outer diameters of 3 and 5 cm, line widths of 500 and 1000 μm , and various numbers of turns were compared. The calculations were performed assuming a sheet resistance of 47 $\text{m}\Omega/\square$, corresponding to a single 7 μm thick layer of Dupont 5028 silver microflake conductor printed using a 400-mesh screen, and setting $w = s$. Calculated inductance and resistance values are shown in Figure 6.2a and b, respectively. The model predicts that inductance and resistance both increase as the outer diameter and number of turns are increased, or as the line width is decreased.

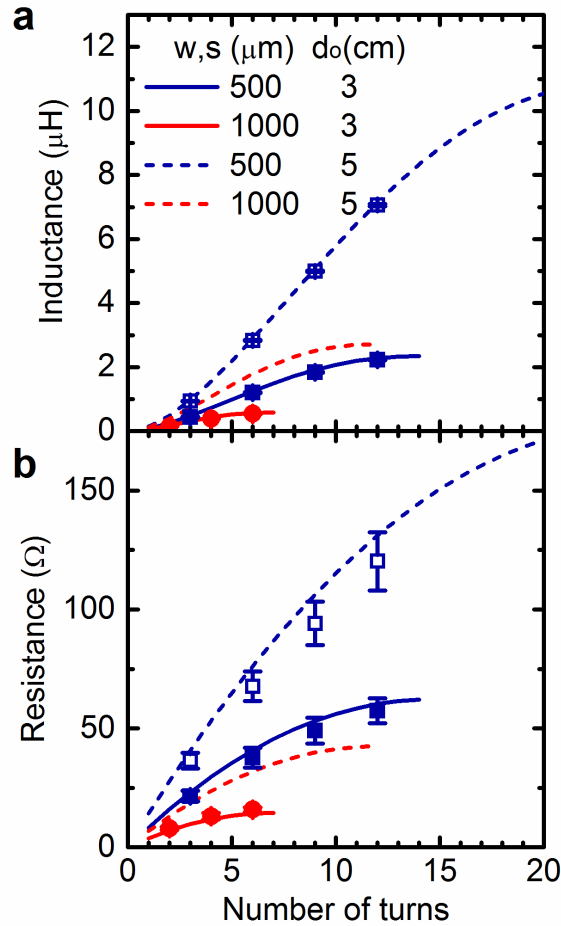


Figure 6.2: Inductance (a) and DC resistance (b) for a variety of inductor geometries. Lines and markers correspond to calculated and measured values, respectively.

Inductors spanning a range of geometries and inductances were fabricated on PET substrates in order to assess the accuracy of the model predictions. Measured inductance and resistance values are shown in Figure 6.2. While the resistances show some deviation from the expected values, mainly due to variations in thickness and uniformity of the deposited ink, the inductance shows excellent agreement with the model.

These results can be used to design inductors having a desired inductance with minimum DC resistance. For example, suppose an inductance of $2 \mu\text{H}$ is desired. Figure 6.2a shows that this inductance can be achieved using 3 cm outer diameter, 500 μm line width, and 10 turns. The same inductance can also be produced using a 5 cm outer diameter, with either 500 μm line width and 5 turns or 1000 μm line width and 7 turns (also shown in the figure). Comparing the resistance of these three possible geometries in Figure 6.2b reveals that the 5 cm inductor with 1000 μm line width has the lowest resistance of 34 Ω , about 40%

Table 6.1: Geometric parameters and inductance of inductors fabricated in this work. Inductance is listed as the measured value followed by the calculated value (from the model) in parentheses.

Inductor Name	Outer Diameter (cm)	Line Width (μm)	Space Width (μm)	Number of Turns	Inductance (μH)
L1	3	500	500	12	2.23 ± 0.02 (2.3)
L2	5	500	500	12	7.06 ± 0.04 (7.2)
L3	5	1000	500	13	4.720 ± 0.002 (4.7)
L4	6	1000	500	16	7.839 ± 0.005 (8.0)

Table 6.2: Comparison of commercially available silver inks for printed inductor fabrication. Conductivity, thickness per coat, and inductor performance are experimentally measured. Viscosity values are cited from the manufacturers' data sheets.

Ink	Conductivity (% of bulk Ag)	Thickness per Coat (μm)	Viscosity (Pa·s)	Performance of Inductor L2
Inktec PR-010	33	2	7-7.5 [31]	Good print with ≤ 2 coats, Min. resistance 34Ω
Dupont 5028	5	7	15-30 [29]	Good print with ≤ 9 coats, Min. resistance 15Ω
Dupont 5064H	15	4	10-20 [30]	Good print with ≤ 6 coats, Min. resistance 11Ω

lower than the other two. The generalized design process to achieve a given inductance with minimum resistance is summarized as follows: first, the largest allowable outer diameter is selected based on the spatial constraints imposed by the application. Then, the line width should be made as large as possible while still allowing the desired inductance to be reached, resulting in a high fill ratio (Equation 6.3).

6.3.2 Ink and printing optimization

Reducing the sheet resistance of the metal films, by increasing the thickness or by using a material with higher conductivity, can further reduce the DC resistance without impacting the inductance. The achievable thickness and conductivity depend on the morphology of the silver particles as well as the rheology of the ink. Therefore, two inductors with geometric parameters given in Table 6.1, referred to as L1 and L2, were fabricated with varying numbers of coats and three different inks, to evaluate the change in resistance. Characteristics of the three inks, one nanoparticle ink and two microparticle inks, are compared in Table 6.2.

Of the three inks compared, the silver nanoparticle ink (Inktec PR-010) offered the highest conductivity, since the small particles could be sintered at temperatures compatible with the

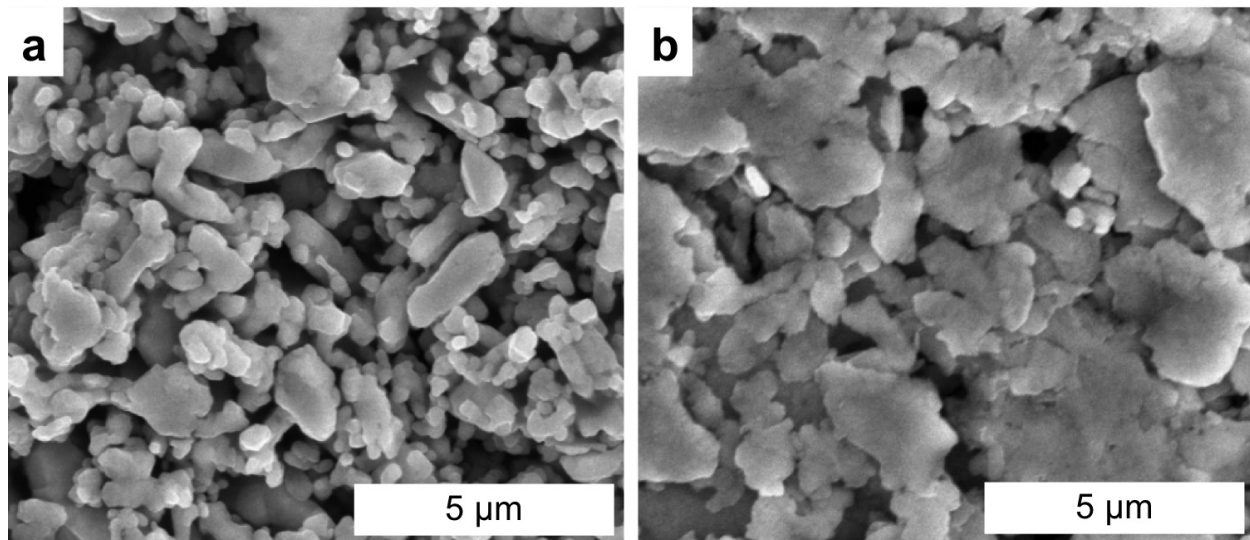


Figure 6.3: SEM micrographs of films screen-printed from Dupont 5028 (a) and 5064H (b) silver microparticle inks [1]. Images taken by Dr. Igal Deckman.

PET substrate to form a film most closely resembling bulk silver [31]. The conductivity of the Dupont 5064H microparticle ink was approximately half that of the nanoparticle ink, and the conductivity of the Dupont 5028 microparticle ink was another factor of three lower than the 5064H. As seen in the SEM micrographs of films printed from the two microparticle inks, Figure 6.3, the reduced conductivity of the 5028 ink compared to the 5064H arises from its smaller particle size and the presence of many voids between the particles in the printed film. The 5064H, on the other hand, has larger and more closely packed flakes, giving behavior closer to that of bulk silver.

For a given film thickness, the material with the highest conductivity would have the lowest sheet resistance (Equation 6.7). However, to determine realistic ranges of sheet resistance achievable by printing, it is important to consider the actual thickness of a coat of each type of ink. The film thickness is determined in part by the wet thickness of the ink transferred to the substrate, which depends on the mesh size of the screen and the amount the ink spreads after printing (known as “slump”), which is related to viscosity and surface tension [35]. The metal fraction and the porosity of the dried film also play an important role. As seen in Table 6.2, the Inktec nanoparticle ink has the lowest thickness, and the Dupont 5028 microparticle ink has the highest thickness. Overall, due to the combination of conductivity and thickness, single coats of the Inktec ink and the Dupont 5064H ink have approximately the same sheet resistance, while the sheet resistance of a coat of Dupont 5028 is substantially higher.

The measured resistances of inductors with various numbers of coats of Dupont 5028 and 5064H are shown in Figure 6.4a and b, for inductors L1 and L2 respectively. As the number of coats of ink was increased, the resistance decreased roughly proportionally, as expected.

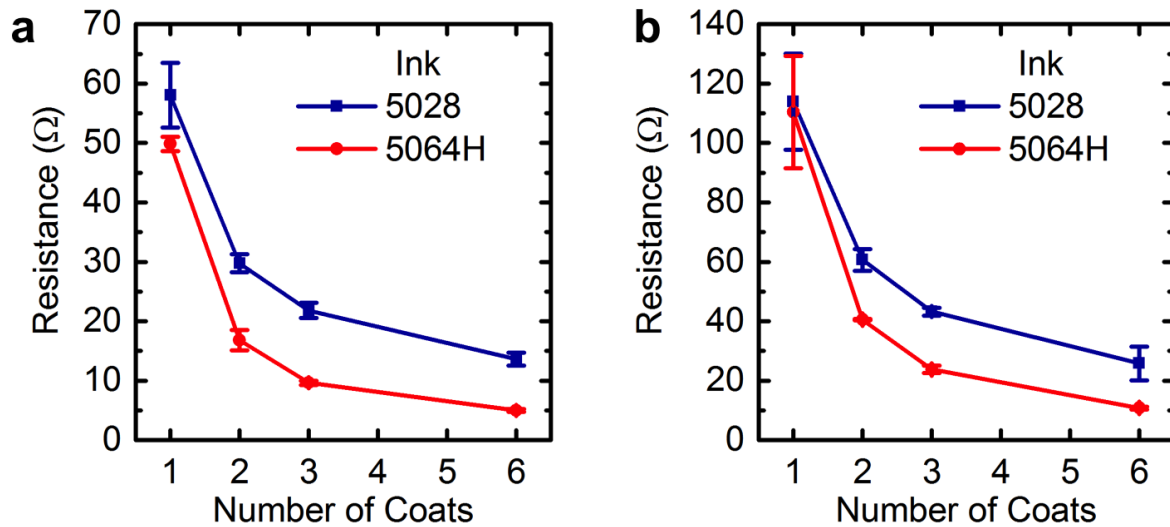


Figure 6.4: DC resistance of inductors L1 (a) and L2 (b) screen-printed from Dupont 5028 and 5064H silver inks.

While the greatest reduction in resistance (50-65%) occurred between 1 and 2 coats, further increasing the thickness beyond 2 coats is clearly desirable. For example, a 6-fold reduction in resistance was achieved through the application of 6 coats. A screen with a relatively small mesh size (400 threads per inch) was used to print these inductors because each coat of ink is relatively thin, allowing the effect of conductor thickness on resistance to be investigated thoroughly. Similar thickness (and resistance) could be achieved faster by printing a smaller number of coats with a larger mesh size, as long as the patterned features remain larger than the minimum resolution of the mesh. This approach could be used to achieve the same DC resistance as the 6-coat inductors discussed here, but with higher production speed.

Although printing multiple coats of ink is desirable to reduce the resistance of a given feature, the practical number of coats that can be printed is limited by the slump of the ink and the resolution of the pattern. A low viscosity leads to a high rate of slump [35]. Achieving a large total film thickness while maintaining the fidelity of patterns with small spaces (such as the 500 μm space width of the inductors) thus requires a high viscosity. The viscosities of the three inks are given in Table 6.2 along with the best performance achieved for the test inductor L2. With the Inktec nanoparticle ink, which had the lowest viscosity, only 2 coats could be printed sequentially before shorts began to occur between neighboring turns of the inductor. For the Dupont 5064H and 5028 inks, which had the middle and highest viscosities respectively, 6 and 9 coats could be printed before shorts became prevalent. As a result of these differences combined with the conductivity and thickness per coat, the lowest inductor resistance overall was achieved using the Dupont 5064H ink. These printed films also had excellent lifetime, demonstrating no significant change in electrical characteristics after more than a year of storage, unencapsulated, in ambient conditions.

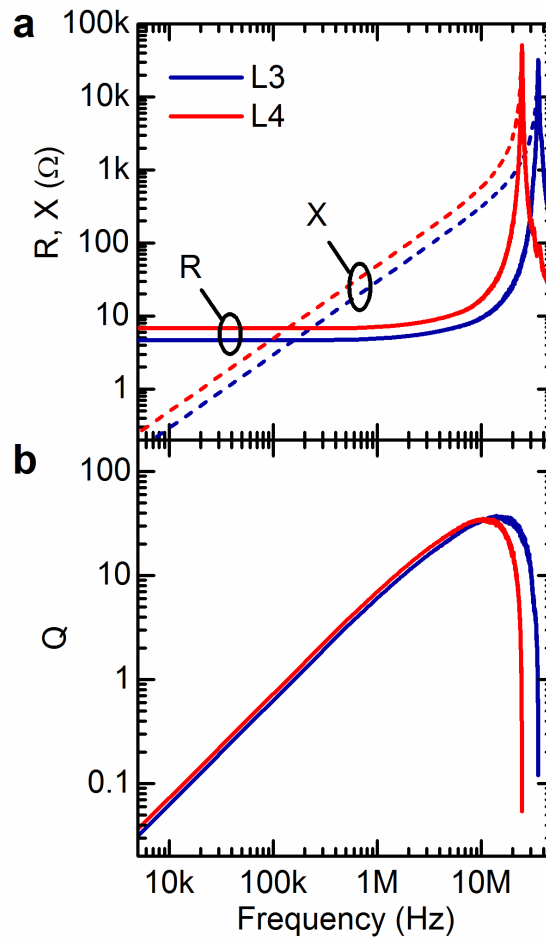


Figure 6.5: Measured resistance R and reactance X (a) and quality factor Q (b) versus frequency for inductors L3 and L4.

6.3.3 Optimized inductors for power electronics

While the inductance (Equation 6.1) depends on the period of the turns, $w + s$, the resistance (Equation 6.5) depends only on the line width w . Therefore, by increasing the ratio of w to s , the resistance can be reduced independent of the inductance. Two additional inductors, L3 and L4, were designed with $w = 2s$ and large outer diameter, as shown in Table 6.1. These inductors were fabricated using 6 coats of Dupont 5064H, shown to give the highest performance in the previous section. L3 had inductance of $4.720 \pm 0.002 \mu\text{H}$ with resistance of $4.9 \pm 0.1 \Omega$, while L4 had $7.839 \pm 0.005 \mu\text{H}$ and $6.9 \pm 0.1 \Omega$, in good agreement with the model predictions. This represents an improvement in the L/R ratio of more than an order of magnitude relative to the values in Figure 6.2, due to the enhancements in thickness, conductivity, and w/s .

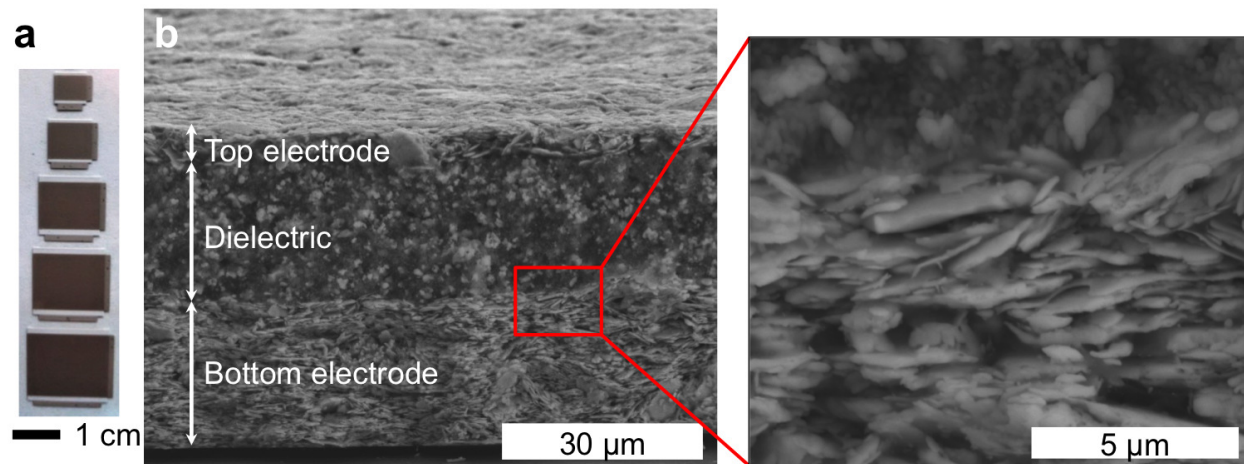


Figure 6.6: (a) Photographs of capacitors with five different areas. (b) Cross-sectional SEM micrographs of a capacitor with two coats of dielectric, showing the barium titanate dielectric and silver electrodes [1]. SEM images taken by Dr. Igal Deckman.

Although a low DC resistance is promising, assessing the suitability of the inductors for power electronics operating in the kHz-MHz range requires characterization at AC frequencies. Figure 6.5a shows the dependence of resistance and reactance of L3 and L4 on frequency. For frequencies below 10 MHz, the resistance stays roughly constant at its DC value, and the reactance increases linearly with frequency, implying a constant inductance as expected. The self-resonant frequency (SRF), defined as the frequency at which the impedance transitions from inductive to capacitive, occurs at 35.6 ± 0.3 MHz for L3 and 24.3 ± 0.6 MHz for L4. The dependence of the quality factor Q , equal to $\omega L/R$, on frequency is shown in Figure 6.5b. L3 and L4 reach their maximum quality factors of 35 ± 1 and 33 ± 1 at frequencies of 11 and 16 MHz respectively. The inductance of several μH and relatively high Q in the high kHz to MHz frequencies make these inductors adequate replacements for conventional surface-mount inductors in low-power DC-DC converters.

6.4 Capacitors

To minimize the required footprint for a given capacitance, it is desirable to use a capacitor technology with a large specific capacitance, equal to the dielectric permittivity ϵ divided by the thickness of the dielectric. In this work, a barium titanate composite was chosen for the dielectric, because it presents higher ϵ than other solution-processed organic dielectrics. The dielectric layer was screen-printed between two layers of the silver conductor to form a metal-dielectric-metal structure. Capacitors with various dimensions on the centimeter scale, as shown in Figure 6.6a, were fabricated using either two or three coats of dielectric ink, to maintain good yield. Figure 6.6b shows cross-sectional SEM micrographs of a representative

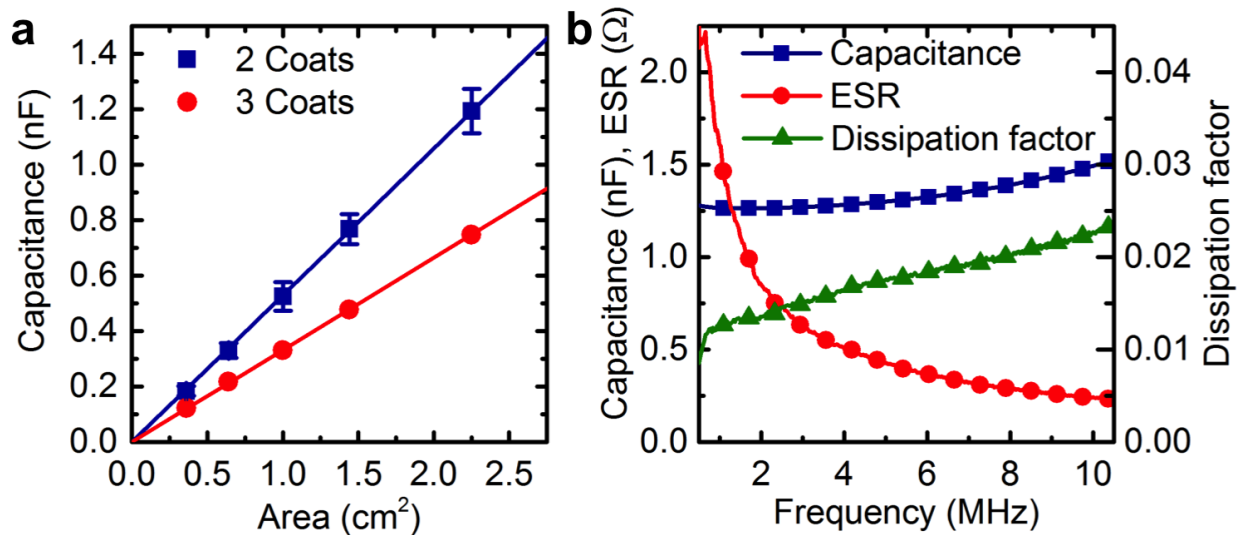


Figure 6.7: (a) Capacitance of capacitors with 2 and 3 coats of barium titanate dielectric and varying area, measured at 1 MHz. (b) Capacitance, ESR, and dissipation factor of a 2.25 cm² capacitor with 2 coats of dielectric, vs. frequency.

capacitor fabricated with two coats of dielectric, for a total dielectric thickness of 21 μm . The top and bottom electrodes are one and six coats of 5064H, respectively. The micron-scale barium titanate particles are visible in the SEM image as brighter areas surrounded by the darker organic binder. The dielectric ink wets the bottom electrode well, forming a clear interface with the printed metal film, as shown in the higher-magnification inset figure.

The capacitance scales proportionally with area as expected, as shown in Figure 6.7a, with a specific capacitance of 0.53 nF/cm² for two coats of dielectric and 0.33 nF/cm² for three coats. These values correspond to a permittivity of 13. Capacitance and dissipation factor (DF) were also measured at varying frequency, as shown in Figure 6.7b for a 2.25 cm² capacitor with two coats of dielectric. The capacitance was found to be relatively flat over the frequency range of interest, increasing by 20% from 1 to 10 MHz, while the DF increases from 0.013 to 0.023 over that same range. As the dissipation factor is a ratio of energy lost to energy stored per AC cycle, a DF of 0.02 signifies that 2% of the power handled by the capacitor is dissipated. This loss is also often expressed as a frequency-dependent equivalent series resistance (ESR), equal to $DF/\omega C$, in series with the capacitor. As shown in Figure 6.7b, the ESR is below 1.5 Ω for frequencies greater than 1 MHz and below 0.5 Ω for frequencies greater than 4 MHz.

While the μF -scale capacitances needed for DC-DC converters would require prohibitively large areas using this capacitor technology, the 100 pF - nF capacitance range and low loss of these capacitors makes them suitable for other applications, such as filters and resonant circuits. A number of approaches could be used to increase the capacitance. A higher dielectric constant would increase the specific capacitance [36]; this can be achieved by

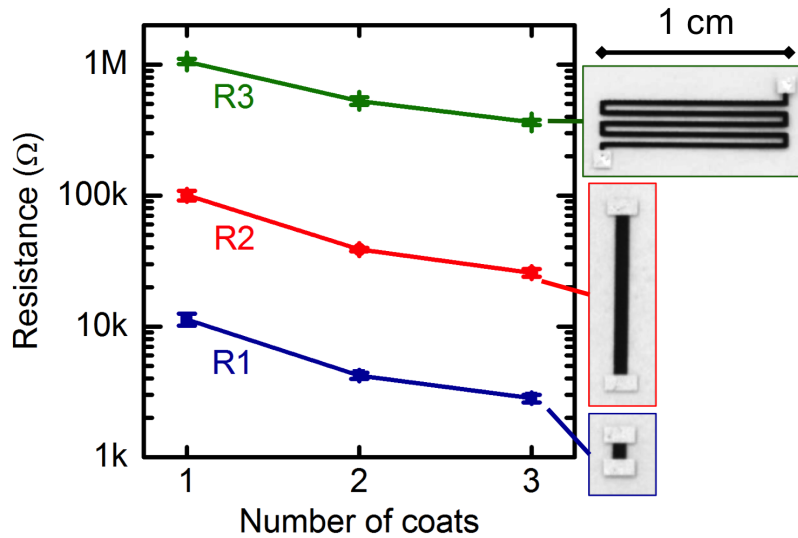


Figure 6.8: Resistance of three different resistor geometries with varying numbers of coats of carbon resistive ink. Photographs of the three resistors are shown on the right.

increasing the concentration of barium titanate particles in the ink, for example. A smaller dielectric thickness could be used, although this would require a bottom electrode with lower roughness than the screen printed silver flakes. Thinner, lower roughness layers for capacitors can be deposited by spray coating [37], inkjet printing [25], or gravure printing [21], which could be integrated with the screen printing process. Finally, multiple alternating layers of metal and dielectric could be printed in a stack and connected in parallel, increasing the capacitance per unit area [28].

6.5 Resistors

Voltage dividers, consisting of a pair of resistors, are typically used to perform the voltage measurement necessary for feedback control of a voltage regulator. For this type of application, printed resistors should present resistances in the range of $k\Omega$ - $M\Omega$ and low variation from device to device. Here, a single coat of screen-printed carbon ink was found to have a sheet resistance of $900 \Omega/\square$. This information was used to design two straight-line resistors (R1 and R2) and one serpentine resistor (R3) with nominal resistances of $10 k\Omega$, $100 k\Omega$, and $1.5 M\Omega$, respectively. Resistances in between the nominal values were achieved by printing two or three coats of ink, as shown in Figure 6.8 alongside photographs of the three resistors. 8-12 samples of each type were fabricated; in all cases, the standard deviation of the resistances was 10% or less. Samples with two or three coats tended to have slightly less variation in resistance than those with one coat. The small variation in measured resistance

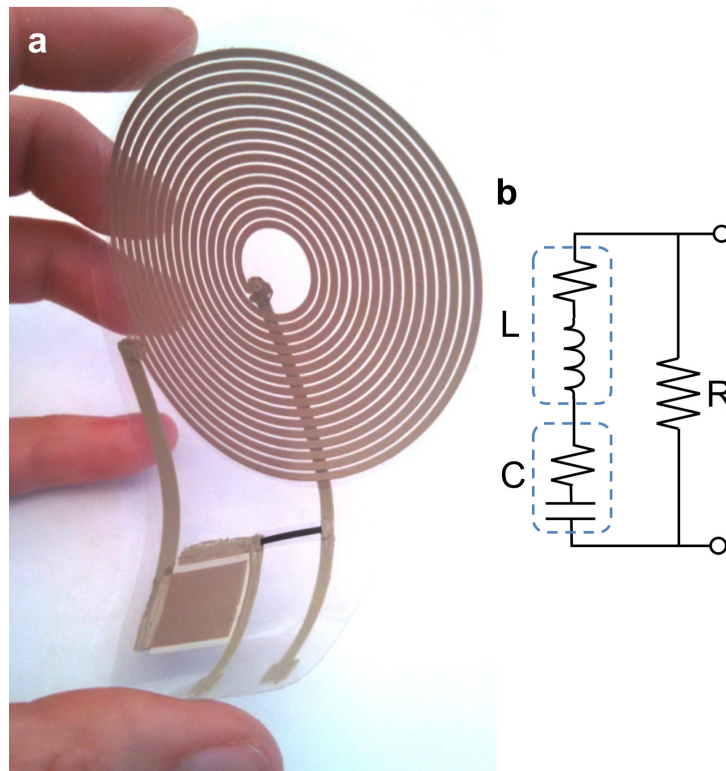


Figure 6.9: (a) Photograph of screen-printed RLC circuit using a series combination of $8 \mu\text{H}$ inductor and 0.8 nF capacitor, in parallel with a $25 \text{ k}\Omega$ resistor. (b) Diagram of the circuit including inductor and capacitor series resistances.

and close agreement with the nominal values suggests that other resistances in this range can be obtained straightforwardly by modifying the resistor geometry.

6.6 Circuits

6.6.1 RLC circuit

An RLC circuit, a classic textbook example of the combination of resistor, inductor, and capacitor, was fabricated to demonstrate and verify the behavior of the passive components integrated into a truly printed circuit. In this circuit, an $8 \mu\text{H}$ inductor and a 0.8 nF capacitor were connected in series, and a $25 \text{ k}\Omega$ resistor was placed in parallel with them. A photograph of the flexible circuit is shown in Figure 6.9a. This particular series-parallel combination was selected because its behavior is dominated by each of the three components at different frequencies, allowing the performance of each one to be highlighted and assessed. The expected frequency response of the circuit was calculated, taking into account the 7Ω series resistance of the inductor and the 1.3Ω ESR of the capacitor. The circuit diagram

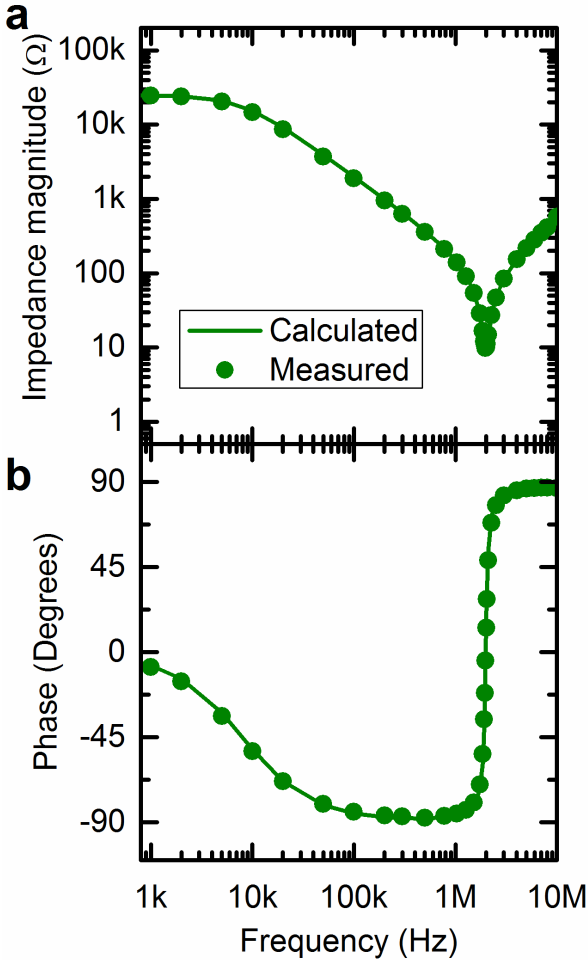


Figure 6.10: Impedance magnitude (a) and phase (b) of the printed RLC circuit.

is shown in Figure 6.9b, and the calculated impedance magnitude and phase are shown in Figure 6.10a and b along with measured values. At low frequency, the high impedance of the capacitor means that the behavior of the circuit is dominated by the 25 k Ω resistor. As the frequency increases, the impedance of the LC path decreases; the overall circuit behavior is capacitive until the resonant frequency of 2.0 MHz. Above the resonant frequency, the inductor impedance dominates. Figure 6.10 clearly shows the excellent agreement between the calculated and measured values over the entire frequency range. This signifies that the model used here, where the inductors and capacitors are ideal components with series resistances, is accurate for predicting circuit behavior at these frequencies.

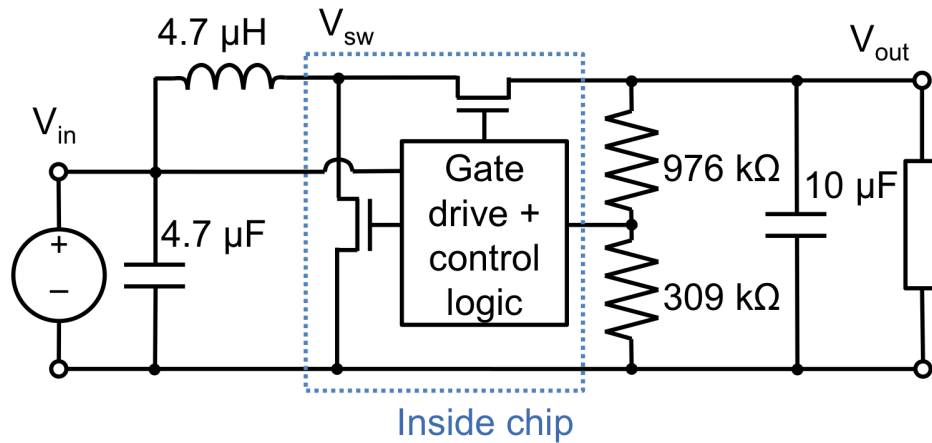


Figure 6.11: Diagram of the voltage regulator circuit constructed in this work.

6.6.2 Voltage regulator

Finally, the printed inductors and resistors were implemented in a step-up voltage regulator. The IC used in this demonstration was the Microchip MCP1640B [5], a pulse width modulation (PWM) based synchronous boost regulator operating at 500 kHz. The circuit diagram is shown in Figure 6.11. A $4.7 \mu\text{H}$ inductor and two capacitors ($4.7 \mu\text{F}$ and $10 \mu\text{F}$) are used as the energy storage elements, and a pair of resistors is used to measure the output voltage for the feedback control. The resistor values were chosen to regulate the output voltage to 5 V. The circuit was fabricated on a PCB and its performance was measured over a range of load resistances and input voltages between 3 and 4 V, simulating the voltages of a lithium-ion battery at various states of charge. The efficiency with printed inductors and resistors was compared to that with SMT inductor and resistors. SMT capacitors were used in all cases, because the capacitances required for this application were too large to accomplish using the printed capacitors.

Waveforms measured using a printed inductor are shown in Figure 6.12, for a 4.0 V input voltage and 1000Ω load resistance. Figure 6.12b shows the voltage at the V_{sw} terminal of the IC; the voltage across the inductor is $V_{in} - V_{sw}$. Figure 6.12c shows current into the inductor. Efficiency of the circuits with SMT and printed components is shown as a function of input voltage and load resistance in Figure 6.13a, and Figure 6.13b shows the ratio of efficiency with printed components to that with SMT components. The measured efficiencies with the SMT components are similar to the expected values given in the manufacturer's data sheet [5]. At high input currents (low load resistance and low input voltage), the efficiency is substantially lower with the printed inductor than with the SMT inductor due to the higher series resistance. However, with higher input voltage and higher output current the resistive losses become less significant and the performance with the printed inductor begins to approach that of the SMT inductor. For load resistances $>500 \Omega$ with $V_{in} = 4.0 \text{ V}$, or

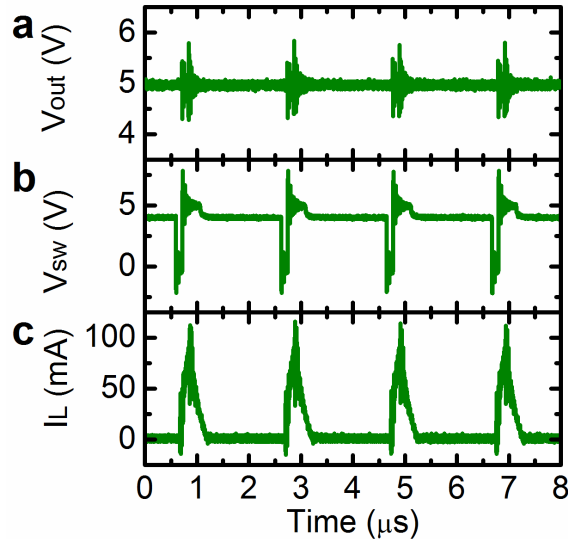


Figure 6.12: Waveforms of (a) V_{out} , (b) V_{sw} and (c) current into the inductor, with 4.0 V input voltage and 1 k Ω load resistance, measured using printed inductor. Surface-mount resistors and capacitors were used for this measurement.

>750 Ω with $V_{in} = 3.5$ V, the efficiency with the printed inductor is >85% of that with the SMT inductor.

Comparing the current waveform in Figure 6.12c with the measured power loss confirms that resistive losses in the inductor are primarily responsible for the difference in efficiency between the printed and SMT circuits. The measured input and output power for 4.0 V input voltage and 1000 Ω load resistance were 30.4 mW and 25.8 mW for the circuit with SMT components, and 33.1 mW and 25.2 mW for the circuit with printed components, respectively. The loss in the printed circuit is therefore 7.9 mW, 3.4 mW higher than that of the circuit with SMT components. The RMS inductor current calculated from the waveform in Figure 6.12c is 25.6 mA, giving an expected power loss of 3.2 mW due to its series resistance of 4.9 Ω . This is 96% of the measured 3.4 mW difference in DC power. Additionally, circuits were fabricated with a printed inductor and printed resistors as well as with a printed inductor and SMT resistors, and no significant difference in efficiency was observed between them.

To demonstrate a potential application of the flexible power electronic components, a voltage regulator including a printed inductor was connected between a flexible lithium-ion battery as the source and an array of OLEDs as the load. The OLEDs were fabricated by Claire Lochner according to Lochner et al. [32], and each OLED pixel drew 0.6 mA at 5V. Like the battery in Chapter 5, this battery employed lithium cobalt oxide and graphite respectively as the cathode and anode, and was fabricated by blade coating, the most common battery printing method [38], by Dr. Abhinav Gaikwad. The capacity of the battery was 16 mAh and its voltage was 4.0 V at the time of testing. Figure 6.14 shows a photograph of the circuit powering two OLED pixels in parallel. In the second prototype of the system,

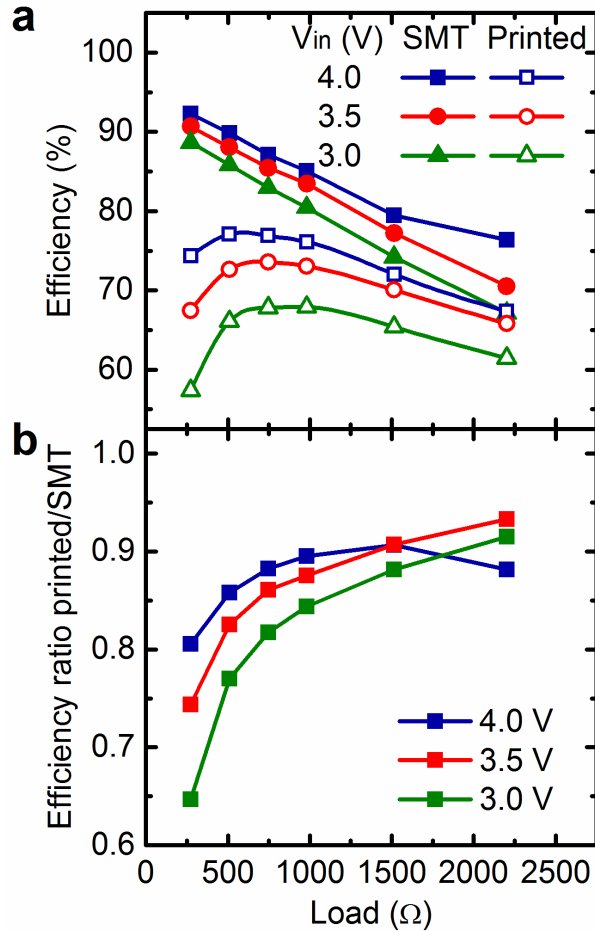


Figure 6.13: (a) Efficiency of a voltage regulator circuit using all surface-mount components vs. one with printed inductor and resistors, for various load resistances and input voltages. (b) Ratio of efficiencies of the surface-mount and printed circuits shown in (a).

shown powering three OLED pixels in Figure 6.15, the regulator was fabricated on a flex-PCB and printed resistors were used in place of the SMT resistors. Permanent connections using conductive epoxy, along with lower-profile connectors, were employed in place of the bulky clips used in the first prototype.

These demonstrations show the potential of the printed power components to be integrated with other flexible and organic devices to form more complex electronic systems. Use of printed components in power electronics also offers opportunities to realize power systems that are even more flexible, lower profile, and more thoroughly integrated than those developed in this chapter. For example, the low temperatures and high-viscosity inks used to produce screen-printed films should allow the passive components, as well as interconnects between devices and contact pads for surface-mount components, to be printed on arbitrary

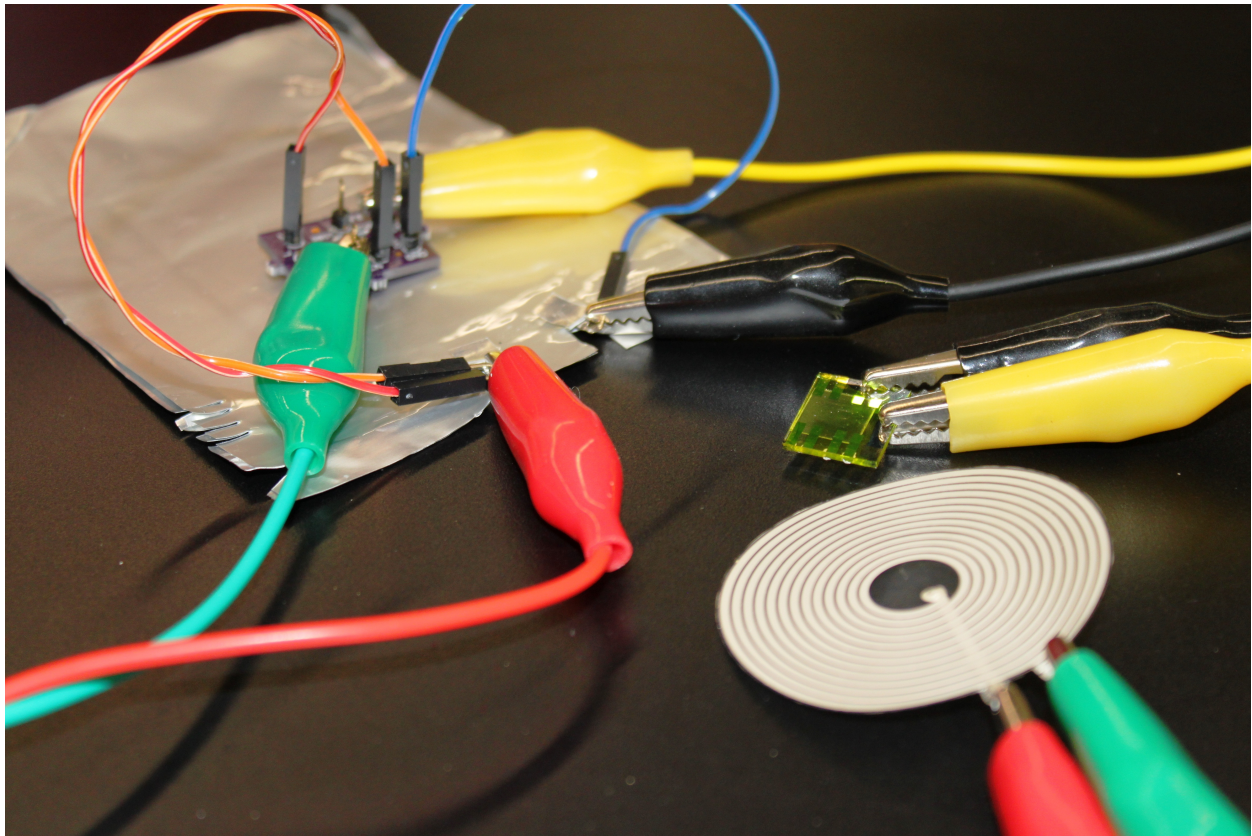


Figure 6.14: Photograph of a voltage regulator circuit using printed inductor, with a flexible lithium-ion battery as the source and organic LEDs as the load.

substrates. This combined with the use of existing low-temperature conductive adhesives [39] for the surface-mount components would allow the entire circuit to be built, without subtractive processes such as PCB etching, on an inexpensive substrate such as PET.

6.7 Conclusion

Screen-printed inductors, capacitors, and resistors have been demonstrated with a range of values on flexible PET substrates, with the goal of replacing surface-mount components in power electronics. This work has shown that the resistance of the inductors, which is of great concern for power electronics, can be reduced by more than an order of magnitude by designing the spiral with large diameter, fill ratio, and line width-space width ratio, and by using a thick layer of low resistivity ink. The components were integrated into a fully printed and flexible RLC circuit and show predictable electrical behavior in the kHz-MHz frequency range that is of most interest for power electronics.

A typical use case for printed power electronics would be in a wearable or product-

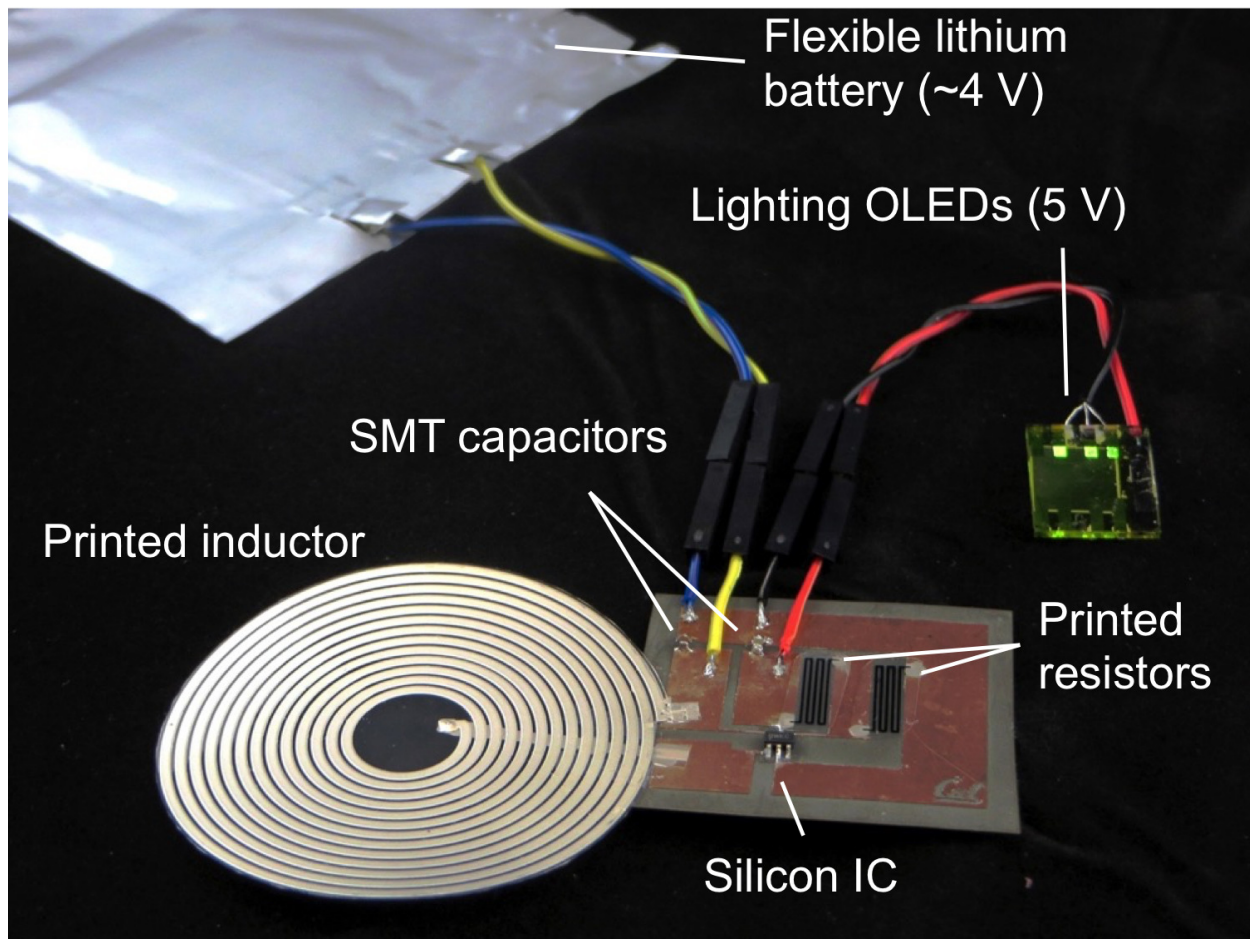


Figure 6.15: Photograph of a voltage regulator circuit on a flex-PCB using printed inductor and printed resistors, with a flexible lithium-ion battery as the source and organic LEDs as the load.

integrated flexible electronic system powered by a flexible rechargeable battery, such as lithium-ion, which produces a variable voltage depending on its state of charge. If the loads, which would include printed and organic electronic devices, require a constant voltage or one that is higher than the battery output, a voltage regulator is needed. For this reason, the printed inductor and resistors were integrated into a step-up voltage regulator alongside a conventional silicon IC, which was used to power OLEDs at a constant voltage of 5 V from a variable-voltage battery source. Efficiency of the circuit surpassed 85% of that of a control circuit using surface-mount inductor and resistors over a range of load currents and input voltages. Despite the material and geometry optimizations, resistive losses in the inductor remained the limiting factor of the circuit performance at high current levels (input current greater than about 10 mA). At lower currents, however, the losses in the inductor were reduced and the overall performance became limited by the IC efficiency. Since many

printed and organic devices require relatively low currents, such as the small OLEDs used in this demonstration, the printed power inductor can be deemed appropriate for this type of application. Higher overall converter efficiency may be achieved by utilizing an IC designed to have the highest efficiency at lower current levels.

In this chapter, the voltage regulators were built using conventional PCB, flex-PCB, and soldering techniques for the surface-mount components, and the printed components were fabricated on separate substrates. However, there is great opportunity for further integration, due to the low temperatures and additive nature of the screen printing process, the ability to combine SMT and printed components on the same substrate with conductive adhesives, and the flexibility and low profile of the printed components. The screen-printed passive components developed in this work therefore help to pave the way for flexible electronic systems integrating energy sources and loads with high-performing power electronics, using inexpensive substrates, primarily additive processes, and a minimum number of surface-mount components.

6.8 References

1. Ostfeld, A. E., Deckman, I., Gaikwad, A. M., Lochner, C. M. & Arias, A. C. Screen printed passive components for flexible power electronics. *Scientific Reports* **5**, 15959 (2015).
2. Nathan, A., Ahnood, A., Cole, M. T., Suzuki, Y., Hiralal, P., Bonaccorso, F., Hasan, T., Garcia-Gancedo, L., Dyadyusha, A., Haque, S., Andrew, P., Hofmann, S., Moultrie, J., Flewitt, A. J., Ferrari, A. C., Kelly, M. J., Robertson, J., Amaratunga, G. A. J. & Milne, W. I. Flexible electronics: The next ubiquitous platform. *Proceedings of the IEEE* **100**, 1486–1517 (2012).
3. Roselli, L., Borges Carvalho, N., Alimenti, F., Mezzanotte, P., Orecchini, G., Virili, M., Mariotti, C., Goncalves, R. & Pinho, P. Smart surfaces: Large area electronics systems for internet of things enabled by energy harvesting. *Proceedings of the IEEE* **102**, 1723–1746 (2014).
4. Misra, V., Bozkurt, A., Calhoun, B., Jackson, T., Jur, J., Lach, J., Lee, B., Muth, J., Oralkan, O., Ozturk, M., Trolrier-McKinstry, S., Vashae, D., Wentzloff, D. & Zhu, Y. Flexible technologies for self-powered wearable health and environmental sensing. *Proceedings of the IEEE* **103**, 665–681 (2015).
5. Microchip. *MCP1640/B/C/D Data Sheet* 2014. <<http://ww1.microchip.com/downloads/en/DeviceDoc/20002234c.pdf>> (visited on 05/14/2015).
6. Perelaer, J., Smith, P. J., Mager, D., Soltman, D., Volkman, S. K., Subramanian, V., Korvink, J. G. & Schubert, U. S. Printed electronics: The challenges involved in printing devices, interconnects, and contacts based on inorganic materials. *Journal of Materials Chemistry* **20**, 8446–8453 (2010).

7. Arias, A. C., Daniel, J., Krusor, B., Ready, S., Sholin, V. & Street, R. All-additive ink-jet-printed display backplanes: Materials development and integration. *Journal of the Society for Information Display* **15**, 485–490 (2007).
8. Miettinen, J., Pekkanen, V., Kaija, K., Mansikkamäki, P., Mäntysalo, J., Mäntysalo, M., Niittynen, J., Pekkanen, J., Saviak, T. & Rönkkä, R. Inkjet printed System-in-Package design and manufacturing. *Microelectronics Journal* **39**, 1740–1750 (2008).
9. Subramanian, V., Chang, J. B., de la Fuente Vornbrock, A., Huang, D. C., Jagannathan, L., Liao, F., Mattis, B., Molesa, S., Redinger, D. R., Soltman, D., Volkman, S. K. & Zhang, Q. *Printed electronics for low-cost electronic systems: Technology status and application development in ESSDERC 2008 - 38th European Solid-State Device Research Conference* (IEEE, Edinburgh, UK, 2008), 17–24. doi:10.1109/ESSDERC.2008.4681691.
10. Liu, J., Yang, C., Wu, H., Lin, Z., Zhang, Z., Wang, R., Li, B., Kang, F., Shi, L. & Wong, C. P. Future paper based printed circuit boards for green electronics: Fabrication and life cycle assessment. *Energy & Environmental Science* **7**, 3674–3682 (2014).
11. Forrest, S. R. The path to ubiquitous and low-cost organic electronic appliances on plastic. *Nature* **428**, 911–918 (2004).
12. Ben-Salah Akin, M., Rissing, L. & Heumann, W. *Enabling eutectic soldering of 3D opto-electronics onto low Tg flexible polymers in 2014 IEEE 64th Electronic Components and Technology Conference (ECTC)* (IEEE, 2014), 1595–1600. doi:10.1109/ECTC.2014.6897507. <<http://ieeexplore.ieee.org/lpdocs/epic03/wrapper.htm?arnumber=6897507>>.
13. Putaala, J., Hannu, J., Kunnari, E., Mäntysalo, M., Nousiainen, O. & Jantunen, H. Reliability of SMD interconnections on flexible low-temperature substrates with inkjet-printed conductors. *Microelectronics Reliability* **54**, 272–280 (2014).
14. Eshkeiti, A., Reddy, A. S. G., Emamian, S., Narakathu, B. B., Joyce, M., Joyce, M., Fleming, P. D., Bazuin, B. J. & Atashbar, M. Z. Screen printing of multilayered hybrid printed circuit boards on different substrates. *IEEE Transactions on Components, Packaging and Manufacturing Technology* **5**, 415–421 (2015).
15. Acanski, M., Popovic-Gerber, J. & Ferreira, B. *Design of a flexible very low profile high step-up PV module integrated converter in 2012 IEEE Energy Conversion Congress and Exposition (ECCE)* (IEEE, Raleigh, NC, 2012), 2942–2948. doi:10.1109/ECCE.2012.6342365.
16. Khan, S., Dahiya, R. & Lorenzelli, L. Technologies for printing sensors and electronics over large flexible substrates: A review. *IEEE Sensors Journal* **15**, 3164–3185 (2015).
17. Bidoki, S. M., Nouri, J. & Heidari, A. A. Inkjet deposited circuit components. *Journal of Micromechanics and Microengineering* **20**, 055023 (2010).

18. Redinger, D., Molesa, S., Yin, S., Farschi, R. & Subramanian, V. An ink-jet-deposited passive component process for RFID. *IEEE Transactions on Electron Devices* **51**, 1978–1983 (2004).
19. Lim, N., Kim, J., Lee, S., Kim, N. & Cho, G. Screen printed resonant tags for electronic article surveillance tags. *IEEE Transactions on Advanced Packaging* **32**, 72–76 (2009).
20. Nilsson, H.-E., Unander, T., Siden, J., Andersson, H., Manuilskiy, A., Hummelgard, M. & Gulliksson, M. System integration of electronic functions in smart packaging applications. *IEEE Transactions on Components, Packaging and Manufacturing Technology* **2**, 1723–1734 (2012).
21. Jung, Y., Park, H., Park, J.-A., Noh, J., Choi, Y., Jung, M., Jung, K., Pyo, M., Chen, K., Javey, A. & Cho, G. Fully printed flexible and disposable wireless cyclic voltammetry tag. *Scientific Reports* **5**, 8105 (2015).
22. Voutilainen, J.-V., Happonen, T., Hakkinen, J. & Fabritius, T. All silk-screen printed polymer-based remotely readable temperature sensor. *IEEE Sensors Journal* **15**, 723–733 (2015).
23. Leung, S. Y. Y. & Lam, D. C. C. Performance of printed polymer-based RFID antenna on curvilinear surface. *IEEE Transactions on Electronics Packaging Manufacturing* **30**, 200–205 (2007).
24. Park, H., Kang, H., Lee, Y., Park, Y., Noh, J. & Cho, G. Fully roll-to-roll gravure printed rectenna on plastic foils for wireless power transmission at 13.56 MHz. *Nanotechnology* **23**, 344006 (2012).
25. McKerricher, G., Perez, J. G. & Shamim, A. Fully inkjet printed RF inductors and capacitors using polymer dielectric and silver conductive ink with through vias. *IEEE Transactions on Electron Devices* **62**, 1002–1009 (2015).
26. Kim, Y., Kim, H. & Yoo, H.-J. Electrical characterization of screen-printed circuits on the fabric. *IEEE Transactions on Advanced Packaging* **33**, 196–205 (2010).
27. Kang, B. J., Lee, C. K. & Oh, J. H. All-inkjet-printed electrical components and circuit fabrication on a plastic substrate. *Microelectronic Engineering* **97**, 251–254 (2012).
28. Chang, J., Zhang, X., Ge, T. & Zhou, J. Fully printed electronics on flexible substrates: High gain amplifiers and DAC. *Organic Electronics* **15**, 701–710 (2014).
29. DuPont. *DuPont 5028 Silver Conductor technical data sheet* <<http://www.dupont.com/content/dam/dupont/products-and-services/electronic-and-electrical-materials/documents/prodlib/5028.pdf>> (visited on 06/21/2016).
30. DuPont. *DuPont 5064H Silver Conductor technical data sheet* <<http://www.dupont.com/content/dam/dupont/products-and-services/electronic-and-electrical-materials/documents/prodlib/5064H.pdf>> (visited on 06/21/2016).
31. InkTec. *TEC ink brochure* <<http://www.inktec.com.tw/products/electronic-ink/3.pdf>> (visited on 06/21/2016).

32. Lochner, C. M., Khan, Y., Pierre, A. & Arias, A. C. All-organic optoelectronic sensor for pulse oximetry. *Nature Communications* **5**, 5745 (2014).
33. Mohan, S., del Mar Hershenson, M., Boyd, S. & Lee, T. Simple accurate expressions for planar spiral inductances. *IEEE Journal of Solid-State Circuits* **34**, 1419–1424 (1999).
34. Stojanovic, G. & Zivanov, L. *Comparison of optimal design of different spiral inductors in 2004 24th International Conference on Microelectronics* **2** (IEEE, 2004), 613–616. doi:10.1109/ICMEL.2004.1314902. <<http://ieeexplore.ieee.org/lpdocs/epic03/wrapper.htm?arnumber=1314902>>.
35. Abbott, S., Church, T., Parker, D. & Harris, A. *How to be a great screen printer* (ed Abbott, S.) 8–34 (Macdermid Autotype Limited, Wantage, UK, 2008).
36. Reboun, J., Blecha, T., Syrový, T., Hamacek, A. & Shlykevich, A. *Printed passive components for RFID labels in Proceedings of the 5th Electronics System-integration Technology Conference (ESTC)* (IEEE, 2014), 1–5. doi:10.1109/ESTC.2014.6962823. <<http://ieeexplore.ieee.org/lpdocs/epic03/wrapper.htm?arnumber=6962823>>.
37. Van Tassell, B., Yang, S., Le, C., Huang, L., Liu, S., Chando, P., Liu, X., Byro, A., Gerber, D. L., Leland, E. S., Sanders, S. R., Kinget, P. R., Kymissis, I., Steingart, D. & O'Brien, S. Metacapacitors: Printed thin film, flexible capacitors for power conversion applications. *IEEE Transactions on Power Electronics* **31**, 2695–2708 (2016).
38. Gaikwad, A. M., Arias, A. C. & Steingart, D. A. Recent progress on printed flexible batteries: Mechanical challenges, printing technologies, and future prospects. *Energy Technology* **3**, 305–328 (2015).
39. Li, Y. & Wong, C. Recent advances of conductive adhesives as a lead-free alternative in electronic packaging: Materials, processing, reliability and applications. *Materials Science and Engineering R: Reports* **51**, 1–35 (2006).

Chapter 7

Conclusions and Future Work

7.1 Conclusions

The work presented in this thesis represents significant progress toward the vision of ubiquitous, flexible, integrated electronics powered by sustainable energy sources. The use of printing-based fabrication methods facilitates customization and integration of the components, as well as design of systems with flexible and innovative form factors, in a way that the conventional process of assembling discrete off-the-shelf components cannot. To take full advantage of these benefits, the system design process must span many levels, from the selection of materials and manufacturing techniques to the co-design and evaluation of devices. This work aimed to determine and apply the design principles for such systems, in addition to developing high-performing hybrid power electronics and solution-processed photovoltaic modules optimized for integration into power systems.

Organic photovoltaic cells and modules were designed and manufactured using a variety of materials and form factors. Solar cells were built on glass and plastic substrates using single-walled carbon nanotube transparent electrodes as an abundant, flexible, solution processable alternative to ITO. Small monolithically integrated solar modules on glass were developed for integration with alkaline batteries into wearable energy harvesting accessories. Solar module power conversion efficiency up to 7.8% and system energy conversion and storage efficiency of 2.7% were demonstrated under indoor lighting conditions. Larger, printed and flexible OPV modules were also developed to charge lithium-ion batteries in thin-film energy systems. These modules as well as commercial amorphous silicon solar modules were integrated with batteries, battery management electronics, and loads to form complete power systems.

Characterization of system behavior under varying conditions of load and illumination has shed light on several important design variables that can be used to optimize system performance for specific applications. For example, selecting the solar module design to give maximum power output when operated at the battery voltage allows a high energy collection efficiency to be achieved without maximum power point tracking circuitry. For systems which will spend time outdoors harvesting sunlight, the solar module and battery

must both be designed to have high performance at high currents, for example by minimizing series resistance. For wearable systems, which are likely to spend time indoors and outdoors, the indoor lighting conditions may also contribute significantly to the total daily energy collection if the brightness is high enough. If that is the case, the system must also have high performance under low current, requiring low leakage and high battery efficiency at slow charging rates. In addition, optimizing the load duty cycle to match the average load current to the solar module output current can greatly extend the battery lifetime before becoming discharged, without requiring any modification to the battery itself. Finally, material choices such as the choice of transparent electrode material depend on the required size and current of the solar cells, as well as the relative importance of efficiency, flexibility and cost, for the application at hand. For example, carbon nanotube transparent electrodes were shown to be most competitive with ITO when flexibility is needed and when the travel distance for charge carriers in the transparent electrode is short.

While photovoltaics and batteries are well-known and well-studied components of power systems, systems where the load voltage requirements differ from the source output characteristics also require power electronics, for which there has been much less precedent using printed components. Therefore, screen-printed passive components were designed in order to create hybrid flexible power electronics that could be integrated with flexible power sources. Through optimization of inductor geometry and fabrication, inductors of several μH with resistance of only a few Ω and quality factors of 35 were achieved. This result is a significant advance in the performance of printed spiral inductors and enables their use in DC-DC converter applications, where efficiency is critical. A hybrid voltage regulator circuit combining a silicon IC with printed inductor and resistors on a flexible substrate was demonstrated. The circuit with the printed components displayed efficiency surpassing 85% of that of a circuit using all conventional components.

In summary, high-performing energy devices, including power inductors and photovoltaic modules, have been demonstrated and integrated with batteries into power systems. These systems are of great importance for applications that require a wireless and integrated power source, such as wearables for healthcare applications and sensors for the internet of things. Furthermore, the use of low-temperature solution processing and flexible materials for the energy devices can enable their integration with load devices into complete, standalone flexible electronic systems.

7.2 Suggestions for future work

Avenues to further improve device performance and manufacturing viability have been identified throughout this thesis. These suggestions are summarized here, along with some applications that merit further investigation and opportunities to integrate the components more thoroughly into streamlined products.

One issue limiting the commercial viability of organic solar modules is the use of toxic chlorinated solvents such as dichlorobenzene to print the active layer. If OPVs are to be

manufactured at large scale using printing processes, the materials must be deposited from safe solvents such as water or alcohol. Bulk heterojunction devices have been demonstrated using aqueous dispersions of polymer nanoparticles [1]; this technique is of great interest for large-area solar module applications. Regardless of the solvent used, the printing process for the active layer must be optimized to increase uniformity and yield, in order to develop larger-area modules with higher performance. Additionally, for cell areas greater than a few square millimeters, the series resistance of the carbon nanotube transparent electrodes and even ITO on flexible substrates can limit the performance under sunlight. Therefore, adding a sparse printed metal grid to reduce the resistance, or utilizing a higher-conductivity flexible transparent electrode such as a silver nanowire/conducting polymer composite [2], is recommended. Finally, the utility of the solar cell structures used here is limited by their relatively short lifetime under illumination in ambient conditions. Optimizing the active layer materials to improve their stability [3], using inverted cell architectures without PEDOT:PSS or low work function metals [4], and engineering more effective flexible encapsulation materials would improve the lifetime and usefulness of the solar cells.

Flexible power electronics would benefit from a capacitor technology with a much greater specific capacitance than that presented here. Increasing the dielectric constant, for example by using a higher concentration of ceramic particles, would increase the capacitance. The capacitance would also be increased substantially by using a smaller dielectric thickness, on the order of 100 nm rather than the tens of microns used in the screen printed capacitors. Producing films this thin with high yield and reproducibility will require a different printing process, as well as inks with substantially smaller particle size and lower viscosity [5–7]. The roughness of the metal bottom electrode must also be small relative to the dielectric thickness, requiring an alternative to the screen-printed silver flakes. To further increase the capacitance on a given substrate area, multiple alternating layers of metal and dielectric could be printed in a stack and connected in parallel [7, 8].

Although the inductor performance was high compared to most previously reported printed spiral inductors in the literature, further improving the performance would make the inductors appropriate for a greater range of power levels. For example, use of a printable magnetic material (e.g. magnetic nanoparticle ink [9]) would reduce the size of the spiral required to reach a given inductance, thereby reducing the associated resistance.

It is also important to improve the efficiency of DC-DC converter ICs for low power applications beyond what is commercially available today. In the demonstration of power electronics with printed components, the IC was found to be the limiting factor in circuit performance under conditions of low load current. Increasing the IC efficiency would reduce the size of the power source needed for a given load. Also, although maximum power point tracking was not deemed necessary in this work, systems without battery storage may still require it, and would therefore benefit from improved efficiency of power converters.

Although there are still aspects of the components that can be improved, there are also a number of applications that may directly benefit from the designs and results discussed in this work. For example, when two inductors are placed close to each other, the magnetic field caused by an alternating current in one inductor will induce a current in the other,

allowing power to be transferred or data to be communicated wirelessly between systems on two separate substrates. It is of great interest to incorporate coils for wireless power transfer into flexible electronic systems to complement or replace energy harvesting, allowing systems to be powered on demand (without exposed metal contacts) rather than relying on unpredictable ambient energy sources. The design process used here to develop high-performance inductors for DC-DC converters could also be used to develop high-performance printed coils for wireless power transfer.

The wearable power sources could be applied to power a number of wearable healthcare sensors, for example to sense heart rate, body temperature, or blood oxygenation [10]. Since printed and flexible sensors have been developed to monitor several biosignals [11–13], these could be integrated with the power sources into a single self-powered wearable package. The layered thin-film energy harvesting and storage system could also be rolled up and carried as a portable power source, and could be scaled to a larger area to power larger loads. Additionally, since the systems were shown to be effective under indoor lighting conditions, they could also be employed to power devices for sensing, communication, or information display for the internet of things.

There is great opportunity to develop innovative integration schemes for the power sources and loads in these systems. As one example, the power electronics and load devices could all be printed on a single substrate, which could also serve as the encapsulation layer for the PV module. The necessary ICs could be attached to the same substrate using conductive adhesives. Characterizing the mechanical properties of the components and optimizing the printing process to print all of the components with minimal steps would further enable the design of robust and cost-effective flexible electronic systems.

7.3 References

1. Yamamoto, N. A., Payne, M. E., Koehler, M., Facchetti, A., Roman, L. S. & Arias, A. C. Charge transport model for photovoltaic devices based on printed polymer: fullerene nanoparticles. *Solar Energy Materials and Solar Cells* **141**, 171–177 (2015).
2. Gaynor, W., Burkhard, G. F., McGehee, M. D. & Peumans, P. Smooth nanowire/polymer composite transparent electrodes. *Advanced Materials* **23**, 2905–2910 (2011).
3. Kong, J., Song, S., Yoo, M., Lee, G. Y., Kwon, O., Park, J. K., Back, H., Kim, G., Lee, S. H., Suh, H. & Lee, K. Long-term stable polymer solar cells with significantly reduced burn-in loss. *Nature Communications* **5**, 5688 (2014).
4. Beaupré, S. & Leclerc, M. PCDTBT: En route for low cost plastic solar cells. *Journal of Materials Chemistry A* **1**, 11097 (2013).
5. McKerricher, G., Perez, J. G. & Shamim, A. Fully inkjet printed RF inductors and capacitors using polymer dielectric and silver conductive ink with through vias. *IEEE Transactions on Electron Devices* **62**, 1002–1009 (2015).

6. Jung, Y., Park, H., Park, J.-A., Noh, J., Choi, Y., Jung, M., Jung, K., Pyo, M., Chen, K., Javey, A. & Cho, G. Fully printed flexible and disposable wireless cyclic voltammetry tag. *Scientific Reports* **5**, 8105 (2015).
7. Van Tassell, B., Yang, S., Le, C., Huang, L., Liu, S., Chando, P., Liu, X., Byro, A., Gerber, D. L., Leland, E. S., Sanders, S. R., Kinget, P. R., Kymissis, I., Steingart, D. & O'Brien, S. Metacapacitors: Printed thin film, flexible capacitors for power conversion applications. *IEEE Transactions on Power Electronics* **31**, 2695–2708 (2016).
8. Chang, J., Zhang, X., Ge, T. & Zhou, J. Fully printed electronics on flexible substrates: High gain amplifiers and DAC. *Organic Electronics* **15**, 701–710 (2014).
9. Koh, K., Park, J., Park, J., Zhu, X. & Lin, L. *Core-shell magnetic nanoparticles for on-chip RF inductors in 2013 IEEE 26th International Conference on Micro Electro Mechanical Systems (MEMS)* (IEEE, 2013), 465–468. doi:10.1109/MEMSYS.2013.6474279. <<http://ieeexplore.ieee.org/lpdocs/epic03/wrapper.htm?arnumber=6474279>>.
10. Khan, Y., Ostfeld, A. E., Lochner, C. M., Pierre, A. & Arias, A. C. Monitoring of vital signs with flexible and wearable medical devices. *Advanced Materials* **28**, 4373–4395 (2016).
11. Lochner, C. M., Khan, Y., Pierre, A. & Arias, A. C. All-organic optoelectronic sensor for pulse oximetry. *Nature Communications* **5**, 5745 (2014).
12. Khan, Y., Pavinatto, F. J., Lin, M. C., Liao, A., Swisher, S. L., Mann, K., Subramanian, V., Maharbiz, M. M. & Arias, A. C. Inkjet-printed flexible gold electrode arrays for bioelectronic interfaces. *Advanced Functional Materials* **26**, 1004–1013 (2015).
13. Swisher, S. L., Lin, M. C., Liao, A., Leeflang, E. J., Khan, Y., Pavinatto, F. J., Mann, K., Naujokas, A., Young, D., Roy, S., Harrison, M. R., Arias, A. C., Subramanian, V. & Maharbiz, M. M. Impedance sensing device enables early detection of pressure ulcers in vivo. *Nature Communications* **6**, 6575 (2015).